



CERN-THESIS-2012-321

# Reconstruction of the Tau Lepton and the Study of $B^0 D^{*-} \tau^+ \nu_\tau$ at LHCb

THÈSE N° 5384 (2012)

PRÉSENTÉE LE 22 JUIN 2012

À LA FACULTÉ DES SCIENCES DE BASE  
LABORATOIRE DE PHYSIQUE DES HAUTES ÉNERGIES  
PROGRAMME DOCTORAL EN PHYSIQUE

ÉCOLE POLYTECHNIQUE FÉDÉRALE DE LAUSANNE

POUR L'OBTENTION DU GRADE DE DOCTEUR ÈS SCIENCES

PAR

Anne KEUNE

acceptée sur proposition du jury:

Prof. O. Schneider, président du jury

Prof. T. Nakada, directeur de thèse

Prof. M. Calvi, rapporteur

Prof. C. Grab, rapporteur

Dr W. Hulsbergen, rapporteur



ÉCOLE POLYTECHNIQUE  
FÉDÉRALE DE LAUSANNE

Suisse  
2012



*To my father, my mother,  
my sister and brother*



# Acknowledgements

I am indebted to my supervisor Prof. Tatsuya Nakada, who has given me the opportunity to study at EPFL. Throughout the four years he has given me the freedom to develop my own work, yet steered me in the right direction when needed. Always critical and correct, he has taught me a lot.

Special thanks to Fred Blanc who has helped me at every step throughout my Ph.D. He introduced the idea of reconstructing  $\tau \rightarrow 3\pi\nu_\tau$ , which has led to many interesting analysis ideas. I also appreciate the extensive proofreading of my thesis.

I express my gratitude to the ST group. The emulator software was set up for the VELO by Tomasz Szumlak. While I worked on making it compatible with the ST FPGA algorithms, he was always available to help. Guido Haefeli and Alex Gong have played a large role in optimising the emulator. They have helped me understand the firmware and supplied the needed changes to improve the intrinsic consistency with the emulator. Matt Needham, Jeroen van Tilburg, Mark Tobin, Helge Voss, Abraham Gallas Torreira and Olaf Steinkamp have helped me by taking numerous data runs, explaining me the ST software, reading the ST and emulator sections of my thesis and finding ways to improve my work.

I thank the VELO group for letting me be part of their shift team. Thanks to Karol Hennessy and Antonio Pellegrino for reading parts of this thesis and thanks to Adlène Hicheur and Géraldine Conti for providing the initial version of the magnetic field map.

My studies on  $\tau$  decays have brought me to different working groups, who I thank for their ideas and feedback. Many thanks to Wouter Hulsbergen for introducing and explaining the idea of a constrained fit to me. I am grateful to Rob Lambert and Alessandra Borgia for helping me with my stripping line and producing the much needed Monte Carlo samples.

Thanks to my office mates Greig Cowan and Yasmine Ahmis whose expertise on a wide range of subjects was always readily available to me and has been of great help.

Finally, thanks to Erika Lüthi, Esther Hofmann, Lalaine Barbon Strebél, Nathalie Grub and Anu Liisa Saarelainen for all much needed non-physics related help.

*Genève, 01 April 2012*

A. K.



# Abstract

The LHCb experiment at CERN has been designed to perform high precision measurements of B meson decays. In this thesis the LHCb magnetic field parameterization and the emulation of the LHCb Silicon Tracker noise reduction algorithms are discussed. Both studies have contributed to the general performance of the LHCb detector.

The ability of the LHCb experiment to accurately measure B meson production and decay vertices allows the experiment to perform precision time-dependent studies. Most  $\tau$  leptons detected by LHCb either originate from B mesons or  $D_s$  mesons, which causes the  $\tau$  decay vertex to be significantly displaced. This makes the LHCb experiment a great detector for  $\tau$  physics studies. Tauonic decays are thought to be highly sensitive to New Physics contributions due to the high  $\tau$  mass. Each known decay containing a  $\tau$  lepton, also includes at least one  $\tau$  neutrino, due to lepton flavour conservation. Decays containing  $\tau$  leptons are often disregarded due to reconstruction difficulties with neutrinos passing straight through the LHCb detector, carrying undetectable energy. However, if one can overcome these difficulties, there are numerous interesting decays with  $\tau$  leptons that are highly sensitive to New Physics contributions, but are unexplored at LHCb.

In the first part of this thesis the exclusive reconstruction of a number of interesting  $\tau$  physics channels is performed. These decays all suffer from missing energy and some even contain unreconstructable vertices. It is shown that despite these difficulties, the full  $\tau$  momentum can be calculated up to a certain ambiguity in all cases considered. The analytical calculation is then extended to a constrained fit that exploits measurement errors to obtain the best result. The constrained fit improves the reconstruction efficiency and may also improve the accuracy of the calculation.

In the second part, the developed  $\tau$  reconstruction method is tested on LHCb data collected in 2011. A specific tauonic decay is chosen on which the exclusive  $\tau$  reconstruction is performed in an attempt to extract its signal. It is shown that the goodness of the constrained fit can be used as an excellent new selection cut to reduce background. However, to confidently extract the observed number of signal events, the study can be improved. The foundations are laid for exclusive  $\tau$  reconstruction at LHCb and the developed methods in this thesis will continue to be used to perform  $\tau$  physics analyses at LHCb.

**Keywords:** CERN, LHCb, magnetic field parameterization, emulation, Silicon Tracker, noise reduction, tau lepton, exclusive reconstruction, constrained fit





# Résumé

L'expérience LHCb au CERN est conçue pour effectuer des mesures de précision dans le système du méson B. Dans cette thèse, sont présentés la paramétrisation du champ magnétique de l'aimant dipolaire de LHCb, ainsi que l'émulation de l'algorithme de réduction de bruit dans le détecteur de trajectoires au silicium. Les résultats de ces deux études sont essentiels à l'excellente performance du détecteur LHCb.

La mesure de phénomènes dépendant du temps de vie du méson B sont rendu possibles à LHCb par la capacité du détecteur à mesurer avec précision les vertex de production et de désintégration. La plupart des leptons  $\tau$  (tauon) détectés par LHCb proviennent de mésons B ou  $D_s$ . Par conséquent, les tauons sont produit dans des vertex déplacés. Cela fait de LHCb un excellent détecteur pour l'étude de la physique du lepton  $\tau$ . Les désintégrations du  $\tau$  sont en principe très sensibles à la Nouvelle Physique, de part sa masse élevée. Mais la conservation du nombre leptonique implique que chaque lepton  $\tau$  est produit conjointement avec un neutrino  $\tau$ . Les neutrinos traversent le détecteur LHCb sans être détectés. A cause de l'énergie emportée des neutrinos et des difficultés de reconstruction qu'elle implique, les désintégrations contenant un tauon sont souvent ignorées. Toutefois, si des solutions sont trouvées à ces complications, de nombreux processus physiques contenant des leptons  $\tau$  et sensibles à la Nouvelle Physique peuvent être étudiés à LHCb.

Dans un premier temps, cette thèse présente la méthode de reconstruction de plusieurs processus intéressants contenant des leptons  $\tau$ . Dans tous ces processus, le problème de l'énergie manquante due aux neutrinos est adressé. Il est montré que, malgré ces difficultés, la quantité de mouvement du  $\tau$  peut être déterminée dans tous les cas considérés, bien que parfois persiste une ambiguïté dans les solutions. Le calcul analytique est ensuite généralisé à un fit contraint qui exploite les incertitudes de mesures et qui permet une meilleure précision. Finalement, la méthode de reconstruction des leptons  $\tau$  est testée sur les données LHCb collectées en 2011. Une désintégration spécifique a été choisie, pour laquelle il est montré que la qualité du fit contraint peut être utilisée efficacement comme un nouveau critère de sélection. Les données de LHCb sont modélisées, et le signal est mesuré. Toutefois, la description pourra être améliorée dans le futur pour obtenir une mesure plus précise.

Les fondations sont posées pour la reconstruction de leptons  $\tau$ . Les méthodes développées dans cette thèse vont continuer à être utilisées pour l'étude de la physique du lepton  $\tau$  à LHCb.

**Mots clés:** CERN, LHCb, paramétrisation du champ magnétique, émulation, Silicon Tracker, réduction de bruit, tau lepton, la reconstruction exclusive, fit contraint



# Contents

<b>Acknowledgements</b>	<b>v</b>
<b>Abstract</b>	<b>vii</b>
<b>Résumé</b>	<b>ix</b>
<b>Introduction</b>	<b>1</b>
<b>1 Theory</b>	<b>3</b>
1.1 The Standard Model of particle physics . . . . .	3
1.1.1 Particles and forces . . . . .	3
1.1.2 Interaction amplitudes . . . . .	4
1.2 Weak interaction . . . . .	5
1.2.1 The CKM Matrix . . . . .	6
1.2.2 Parity violation . . . . .	7
1.3 Phenomenology of the semileptonic $B^0 \rightarrow D^{*-} \tau^+ \nu_\tau$ decay . . . . .	8
1.3.1 The $b \rightarrow c \ell \nu_\ell$ decay rate . . . . .	8
1.3.2 The $B^0 \rightarrow D^{*-} \tau^+ \nu_\tau$ decay including QCD corrections . . . . .	10
1.3.3 Current measurements . . . . .	13
1.4 New Physics possibilities . . . . .	13
1.5 Conclusion . . . . .	14
<b>2 The LHCb experiment</b>	<b>15</b>
2.1 Magnetic field . . . . .	17
2.1.1 Magnetic field parameterization . . . . .	18
2.1.2 Parameterization results and comparison . . . . .	20
2.2 Tracking system . . . . .	22
2.2.1 Tracker Turicensis . . . . .	23
2.2.2 Inner Tracker . . . . .	23
2.2.3 Silicon Tracker readout . . . . .	24
2.2.4 Outer Tracker . . . . .	25
2.3 Emulation of the ST TELL1 algorithms . . . . .	25
2.3.1 Noise reduction algorithms . . . . .	26
2.3.2 Clustering . . . . .	30

## Contents

---

2.3.3	Results from early data taking . . . . .	31
2.4	Particle identification . . . . .	32
2.4.1	Calorimeters . . . . .	33
2.4.2	Muon system . . . . .	33
2.4.3	RICH detectors . . . . .	34
2.5	Vertex Locator . . . . .	35
2.6	The Trigger . . . . .	37
2.7	LHCb Software . . . . .	38
<b>3</b>	<b>Studies of <math>\tau</math> reconstruction using simulated events</b>	<b>41</b>
3.1	The lepton flavour violating decay $\tau^- \rightarrow \mu^+ \mu^- \mu^-$ . . . . .	42
3.1.1	Estimation of measurement limit at LHCb . . . . .	43
3.1.2	Normalisation difficulties . . . . .	43
3.2	Reconstruction of $\tau^- \rightarrow \pi^+ \pi^- \pi^- \nu_\tau$ from a known vertex . . . . .	45
3.2.1	Analytic reconstruction . . . . .	45
3.2.2	Analytic limitations . . . . .	48
3.2.3	Constrained fit . . . . .	48
3.2.4	Decay time distributions . . . . .	50
3.3	$Z^0 \rightarrow \tau^+ \tau^-$ reconstruction without mass cut . . . . .	51
3.3.1	Constrained fit . . . . .	52
3.3.2	Reconstruction efficiency and accuracy . . . . .	52
3.3.3	di- $\tau$ invariant mass distribution . . . . .	53
3.3.4	Conclusion . . . . .	54
3.4	Ideas on $B_s^0 \rightarrow \tau^+ \tau^-$ reconstruction . . . . .	54
3.4.1	Analytical calculation . . . . .	55
3.4.2	Constrained fit . . . . .	65
3.4.3	Conclusion . . . . .	69
3.5	Further event reconstruction possibilities including a $\tau$ lepton . . . . .	70
3.5.1	The lepton flavour violating decay $B_{(s)}^0 \rightarrow \mu^+ \tau^-$ . . . . .	71
3.5.2	An extra track: $B^+ \rightarrow K^+ \tau^+ \tau^-$ . . . . .	73
3.5.3	An extra vertex: $B^0 \rightarrow K^* \tau^+ \tau^-$ . . . . .	77
3.5.4	Conclusion . . . . .	79
<b>4</b>	<b>The study of <math>B^0 \rightarrow D^{*-} \tau^+ \nu_\tau</math></b>	<b>81</b>
4.1	Final state reconstruction . . . . .	81
4.2	Event pre-selection . . . . .	84
4.2.1	Stripping Cuts . . . . .	85
4.2.2	Results . . . . .	87
4.3	Offline selection . . . . .	87
4.3.1	The value of $\chi^2$ as a selection cut . . . . .	87
4.3.2	Tuning of the selection criteria . . . . .	88
4.3.3	Results . . . . .	90
4.4	Background contributions . . . . .	92

**Contents**

---

4.5 Signal extraction . . . . .	93
4.6 Discussion . . . . .	98
<b>Summary</b>	<b>103</b>
<b>A The <math>b \rightarrow c\ell\nu_\ell</math> decay rate</b>	<b>105</b>
<b>Curriculum Vitae</b>	<b>115</b>



# Introduction

Although the Standard Model is used to describe all particles and their interactions, it is known not to be complete. Measurements in particle decays that are not in agreement with the Standard Model are indicators of New Physics. The differences between measurement and prediction will shed light on the type of New Physics contribution necessary to cause such differences. The semitauonic  $B^0 \rightarrow D^{*-} \tau^+ \nu_\tau$  decay is thought to be highly sensitive to contributions beyond the Standard Model. In this thesis, the foundation of an exclusive reconstruction method is laid, which offers a new approach to the study of the  $B^0 \rightarrow D^{*-} \tau^+ \nu_\tau$ .

In Chapter 1 the Standard Model of particle physics is introduced. Aspects of the Standard Model that are important to the semitauonic  $B^0 \rightarrow D^{*-} \tau^+ \nu_\tau$  decay are emphasised. The decay rate of  $b \rightarrow c \tau^+ \nu_\tau$  is calculated based on a free quark model. More accurate calculations on the decay rate and branching fraction of the full  $B^0 \rightarrow D^{*-} \tau^+ \nu_\tau$  decay including QCD corrections are described. Finally, the current measurements are given and New Physics possibilities are discussed.

Chapter 2 introduces the LHCb experiment. All its subdetectors, responsible for particle identification and track reconstruction, are discussed. Extra emphasis is put on the LHCb magnetic field. A full description of its parameterization, leading to the current field map used by LHCb, is given. The emulation of the Silicon Tracker online noise reduction algorithms and its perfect results are also described in detail. A short description of the LHCb trigger and its software framework is given.

Chapter 3 tackles the exclusive reconstruction of several interesting decays that include at least one  $\tau$  lepton. Analytical reconstruction possibilities are described and the improvements that a constrained fit could bring discussed. All reconstruction analyses in this chapter are based on Monte Carlo data, but the results of the different reconstruction methods are discussed both for generated particles and reconstructed ones.

In Chapter 4 the exclusive  $\tau$  reconstruction is applied on the  $B^0 \rightarrow D^{*-} \tau^+ \nu_\tau$  decay. Its efficiency is tested on  $0.37 \text{ fb}^{-1}$  data taken in 2011. All steps involved with the signal extraction of this decay are covered in this chapter. The signal and physics background distributions are taken from simulation and used to model the real data candidates. A systematics study is performed to determine the likelihood of real  $\tau$  particles being present in the selected data.





# 1 Theory

## 1.1 The Standard Model of particle physics

### 1.1.1 Particles and forces

The Standard Model (SM) of particles and forces is the only theory currently available to describe the fundamental structure of matter and the forces of nature. It is based on the idea that matter is ultimately made from twelve elementary particles and their anti-particles governed by three of the four fundamental forces. These elementary particles are called fermions and hold an intrinsic angular momentum of spin- $\frac{1}{2}$ . The twelve fermions appear as two types: quarks and leptons, with each two elementary particles in three generations. For each particle there is a corresponding anti-particle, which has identical mass and spin, but has opposite values for all other non-zero quantum number labels.

The four fundamental forces of nature are the strong force, electromagnetism (EM), the weak force and gravity. The Standard Model theory encapsulates how the twelve elementary particles interact mediated by the first three of these forces. The effects of gravity, although important on macroscopic scales, are negligible due to their low intensity on the elementary particle scale compared to the other forces. Gravity is therefore not incorporated in the Standard Model.

Each type of interaction has a characteristic set of force carrier particles associated with the quantum excitation of the force field related to that interaction. These mediator particles hold an intrinsic angular momentum of spin-1 and are therefore called bosons. The strong force is mediated by gluons, which couple to colour charge. This type of charge is only carried by quarks and gluons and comes in three types: red, blue and green. The electromagnetic force carrier is the photon and couples to all electrically charged particles. There are three weak force carriers; the neutral Z boson and a positively and a negatively charged W boson. The weak interaction acts on all quarks and leptons. The Standard Model fermions and bosons are summarised in Table 1.1.

## Chapter 1. Theory

---

	Force	EM charge	Charge carrier
Bosons	Strong	0	$g_a, \alpha \in \{1, \dots, 8\}$ (gluons)
	EM	0	$\gamma$ (photon)
	Weak	0	$Z^0$ (Z boson)
		$\pm 1$	$W^\pm$ (W bosons)

	Type	EM charge	I	II	III
Fermions	Quark	$+\frac{2}{3}$	u (up)	c (charm)	t (top)
		$-\frac{1}{3}$	d (down)	s (strange)	b (bottom)
	Lepton	-1	e (electron)	$\mu$ (muon)	$\tau$ (tau)
		0	$\nu_e$ (e neutrino)	$\nu_\mu$ ( $\mu$ neutrino)	$\nu_\tau$ ( $\tau$ neutrino)

Table 1.1: The mediator bosons of the fundamental interactions and the three generations of fermions, divided into quarks and leptons.

In the Standard Model, the electromagnetic and weak interactions are combined into the electroweak interaction. The electromagnetic and weak forces are distinguishable at low energies through spontaneous symmetry breaking, which will be discussed in Section 1.2. A fifth interaction type is needed for this unification. The force carrier of this interaction, the Higgs boson, is still unobserved. The discovery or exclusion of the Higgs boson is one of the goals of the LHC.

Although the Standard Model has proven to be an accurate theory by correctly predicting most physics results, it is still believed to be a low energy effective theory of a more general high energy theory. It also does not include the gravitational force. In addition, it fails to describe experimentally observed phenomena like dark matter and the large matter-antimatter asymmetry in the universe. New experimental results constantly challenge the theory.

### 1.1.2 Interaction amplitudes

Feynman diagrams are a visualisation of particle interactions. Each diagram represents a contribution to the interaction amplitude  $\mathcal{M}$ , where  $|\mathcal{M}|^2$  is related to the probability of the process occurring. There is a basic set of rules for calculating the contribution represented by each diagram, which are called the Feynman rules. Figure 1.1 shows a basic Feynman diagram.

Fermion fields (or wave functions), denoted by  $\psi$  and  $\bar{\psi}$ , are 4-component spinors and are represented by a solid line. The bosonic field,  $A_\mu$ , mediates between the two fermion fields. The vertex factor incorporates the coupling constant,  $g$ , of the interaction, which is a dimensionless number dependent on the strength of the interaction.  $\Gamma^\mu$  represents a  $4 \times 4$  matrix, which describes the Lorentz structure of interaction, as described below.

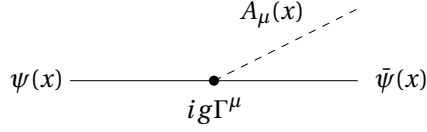


Figure 1.1: A Feynman diagram depicting two fermions mediated by a boson.

Wave functions themselves do not represent observables directly, but observable currents can be constructed from bilinear covariants of the wave functions. Bilinear covariants are products of the form  $\bar{\psi}\Gamma\psi$ , where  $\Gamma$  is a  $4 \times 4$  matrix. Any  $4 \times 4$  matrix can be written as a linear combination of 16 linearly independent matrices. A set of 16 linearly independent matrices is provided by the matrices  $I, \gamma^\mu, \gamma^5, \gamma^\mu\gamma^5$  and  $\sigma^{\mu\nu} = \frac{i}{2}[\gamma^\mu, \gamma^\nu]$ . The bilinear covariants of this set of matrices have the transformation properties of tensors or pseudotensors. The names given to these objects and their transformation properties under a change of coordinates are

$$\text{Scalar: } S(x) = \bar{\psi}\psi \qquad S'(x') = S(x) \qquad (1.1)$$

$$\text{Pseudoscalar: } P(x) = \bar{\psi}\gamma^5\psi \qquad P'(x') = \det(\Lambda)P(x) \qquad (1.2)$$

$$\text{Vector: } V^\mu(x) = \bar{\psi}\gamma^\mu\psi \qquad V^{\mu'}(x') = \Lambda^\mu_{\mu'}V^\mu(x) \qquad (1.3)$$

$$\text{Axial-vector: } A^\mu(x) = \bar{\psi}\gamma^\mu\gamma^5\psi \qquad A^{\mu'}(x') = \det(\Lambda)\Lambda^\mu_{\mu'}A^\mu(x) \qquad (1.4)$$

$$\text{Tensor: } T^{\mu\nu}(x) = \bar{\psi}\sigma^{\mu\nu}\psi \qquad T^{\mu'\nu'}(x') = \Lambda^\mu_{\mu'}\Lambda^\nu_{\nu'}T^{\mu\nu}(x) \qquad (1.5)$$

with

$$\Lambda^\mu_{\mu'} = \frac{\partial x^\mu}{\partial x^{\mu'}} \qquad (1.6)$$

the coordinate transformation matrix.

The interaction Lagrangian for the interaction between a fermionic vector current and a bosonic gauge field is then given by

$$\mathcal{L} = -g\bar{\psi}\gamma^\mu\psi A_\mu \qquad (1.7)$$

In order to calculate the full interaction amplitude, the sum over the contributions of all perturbations of the interaction is taken.

## 1.2 Weak interaction

The weak and electromagnetic forces are unified in the electroweak interaction. The gauge fields or bosons of the electroweak interaction are here denoted by  $W_0, W_1, W_2$  and  $B_0$ . Each of these bosons is massless.

## Chapter 1. Theory

---

The Standard Model  $W^\pm$  and  $Z^0$  bosons of the weak force and the  $\gamma$  of the electromagnetic force are produced by the spontaneous symmetry breaking of the electroweak symmetry caused by the Higgs mechanism [1]. These massive bosons are linear combinations of the electroweak bosons as

$$W^\pm = \frac{1}{\sqrt{2}} (W_1 \mp iW_2) \quad (1.8)$$

$$\begin{pmatrix} \gamma \\ Z^0 \end{pmatrix} = \begin{pmatrix} \cos\theta_W & \sin\theta_W \\ -\sin\theta_W & \cos\theta_W \end{pmatrix} \begin{pmatrix} B_0 \\ W_0 \end{pmatrix} \quad (1.9)$$

where  $\theta_W$  is the Weinberg angle [2].

The mass eigenstates of the quarks are not the same as the weak eigenstates. Mass eigenstates are measured with a definite lifetime and decay width, whereas the weak force acts on the weak eigenstates. In order to describe the transformation between the quark eigenstates, Kobayashi and Maskawa introduced the Cabibbo-Kobayashi-Maskawa (CKM) quark mixing matrix [3]. The  $W^\pm$  bosons change the quark flavour from up-type to down-type and visa versa. They are referred to as the charged current of weak interaction. The neutral weak current, mediated by the  $Z^0$  boson cannot change flavour, just like the photon in the electromagnetic interaction.

The strong and electromagnetic forces conserve the three fundamental discrete symmetries of nature: parity (P), charge conjugation (C) and time reversal (T). The weak interaction has the unique property that it violates parity, as well as charge conjugation and the combined charge-parity (CP) symmetries. However, the combined CPT is still thought to be conserved.

### 1.2.1 The CKM Matrix

The complex, unitary  $3 \times 3$  quark-mixing matrix  $V_{\text{CKM}}$  defines the transformation of down-type quarks from the mass eigenstates  $(d, s, b)$  to the weak eigenstates  $(d', s', b')$ .

$$\begin{pmatrix} d' \\ s' \\ b' \end{pmatrix} = \underbrace{\begin{pmatrix} V_{ud} & V_{us} & V_{ub} \\ V_{cd} & V_{cs} & V_{cb} \\ V_{td} & V_{ts} & V_{tb} \end{pmatrix}}_{V_{\text{CKM}}} \begin{pmatrix} d \\ s \\ b \end{pmatrix} \quad (1.10)$$

Where the elements  $V_{ij}$ , with  $i \in \{u, c, t\}$  and  $j \in \{d, s, b\}$ , represent the different coupling strengths between quarks. The nine elements each initially contribute two degrees of freedom: a real and a complex parameter. However, the unitarity of the matrix implies nine constraints on its complex parameter. Six constraints are due to orthogonality and three to normalisation:

$$\sum_i V_{ij} V_{ik}^* = 0 \quad \text{and} \quad \sum_i |V_{ij}|^2 = 1 \quad (1.11)$$

holds for all  $i \in \{u, c, t\}$  and  $j, k \in \{d, s, b\}$  with  $j \neq k$ . This reduces the eighteen parameters which define the matrix to nine, which can be interpreted as three mixing angles and six complex phases. Redefining the quark fields can be used to reduce the six complex phases to a single complex phase. As a result, the CKM matrix is defined by four parameters: three mixing angles and one phase. This phase is the source of all  $CP$ -violating effects in the Standard Model.

A popular form of the CKM matrix is the Wolfenstein [4] parameterization as it exhibits a hierarchical structure in the magnitudes of the matrix elements

$$V_{\text{CKM}} = \begin{pmatrix} 1 - \frac{\lambda^2}{2} & \lambda & \lambda^3 A(\rho - i\eta) \\ -\lambda & 1 - \frac{\lambda^2}{2} & \lambda^2 A \\ \lambda^3 A(1 - \rho - i\eta) & -\lambda^2 A & 1 \end{pmatrix} + \mathcal{O}(\lambda^4) \quad (1.12)$$

It is obtained from an expansion around  $\lambda = \sin \theta_C$ , with  $\theta_C$  the Cabibbo angle. Currently, the best determination of the expansion parameter is  $\lambda = 0.2253 \pm 0.0007$  [5].  $A$ ,  $\rho$  and  $\eta$  are real parameters of order unity. A non-zero value of  $\eta$  turns some matrix elements into complex numbers, introducing a phase angle and thereby violating  $CP$  invariance.

### 1.2.2 Parity violation

The helicity of a particle is +1 when the sign of the projection of its spin vector onto its momentum vector is positive. Equivalently, its helicity is -1 when this projection is negative. For massive particles, helicity is dependent on the frame of reference. For massless particles it is a Lorentz invariant property of the particle and equal to the more abstract intrinsic property of chirality, which is determined by whether the particle transforms in a right- or left-handed representation of the Poincaré group.

General spinors in the Dirac representation can have both left- and right-handed components. The matrix  $\gamma^5$  is called the chiral projection operator and can separate these components.  $(\gamma^5)^2 = 1$  and therefore its eigenvalues are  $\lambda = \pm 1$ . The right-handed component  $\psi_R$  (eigenvalue +1) and left-handed component  $\psi_L$  (eigenvalue -1) of a general spinor  $\psi$ , can be expressed as

$$\psi_R = P_R \psi \quad \text{and} \quad \psi_L = P_L \psi \quad (1.13)$$

Where the right- ( $P_R$ ) and left-handed ( $P_L$ ) operators are given by

$$P_R = \frac{1 + \gamma^5}{2} \quad \text{and} \quad P_L = \frac{1 - \gamma^5}{2} \quad (1.14)$$

The weak current exhibits a  $V - A$  (Vector minus Axial-Vector) structure. Its interaction

operator is therefore given by

$$\Gamma^\mu = \gamma^\mu \frac{1}{2}(1 - \gamma^5) \quad (1.15)$$

This operator will thus filter out the left component of the spinor, leading to parity violation in the weak system. As a consequence, only left-handed particles or right-handed anti-particles couple to the W boson.

### 1.3 Phenomenology of the semileptonic $B^0 \rightarrow D^{*-} \tau^+ \nu_\tau$ decay

It is not possible to precisely calculate the  $B^0 \rightarrow D^{*-} \tau^+ \nu_\tau$  decay rate due to QCD corrections within the B and  $D^*$  meson.

It is possible though to calculate the  $b \rightarrow c \tau \nu_\tau$  decay rate, when all QCD corrections are neglected and the d-quark acts as a spectator particle. In Section 1.3.1 the branching fraction ratio of  $b \rightarrow c \tau \nu_\tau$  over  $b \rightarrow c \mu \nu_\mu$ , which is equal to the ratio of their decay rates, is calculated.

Several model-dependent or measurement-based calculations that do account for QCD corrections have been performed and are discussed in Section 1.3.2. Current measurements are compared with these calculations in Section 1.3.3.

#### 1.3.1 The $b \rightarrow c \ell \nu_\ell$ decay rate

The general expression for the differential decay rate of a particle of energy  $E$  is given by Fermi's 'Golden Rule':

$$d\Gamma = \frac{1}{2E} \langle |\mathcal{M}|^2 \rangle d\Phi \quad (1.16)$$

where  $d\Phi$  denotes the phase space which depends on the masses and the momenta of the particles in the initial and final states. The details of the interactions of the particles via the various forces are encoded in the matrix element  $\mathcal{M}$ , which is averaged over initial state spins and summed over final state spins.

The decay  $b \rightarrow c \ell \nu_\ell$  occurs through the weak interaction. Figure 1.2 depicts the Feynman diagram of this decay. The vertex factors of this decay are given by  $g_w \Gamma^\mu / \sqrt{2}$ , where the weak interaction coupling strength is denoted by  $g_w$  and the weak  $V - A$  interaction matrix is given by  $\Gamma^\mu = \gamma^\mu \frac{1}{2}(1 - \gamma^5)$ . The CKM element  $|V_{cb}|$  describes the quark mixing. A factor of  $\sqrt{2}$  is applied by convention. The Feynman propagator factor of the mediating W boson is given by

$$\frac{1}{m_W^2 - q^2} \simeq \frac{1}{m_W^2} \quad (1.17)$$

where  $q^2$  denotes the transferred momentum squared by the virtual W, which is negligible

### 1.3. Phenomenology of the semileptonic $B^0 \rightarrow D^{*-} \tau^+ \nu_\tau$ decay

compared to  $m_W^2$ , the W mass squared.

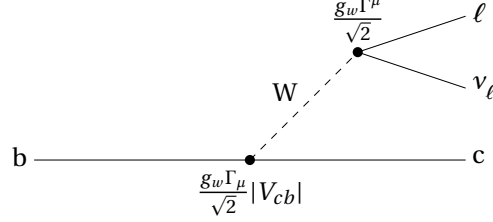


Figure 1.2: A Feynman diagram depicting the  $b \rightarrow c \ell \nu_\ell$  decay according to the quark spectator model.

Combining these decay amplitude contributions, the matrix element is expressed as

$$\mathcal{M} = \frac{g_w}{\sqrt{2}} |V_{cb}| \left( \bar{\psi}_c \gamma_\mu \frac{1}{2} (1 - \gamma^5) \psi_b \right) \cdot \frac{1}{m_W^2} \cdot \frac{g_w}{\sqrt{2}} \left( \bar{\psi}_\ell \gamma^\mu \frac{1}{2} (1 - \gamma^5) \psi_\nu \right) \quad (1.18)$$

The average matrix element squared can solely be expressed in terms of the neutrino energy  $E_\nu$  as (Equation A.11)

$$\langle |\mathcal{M}|^2 \rangle = 64 G_F^2 |V_{cb}|^2 \frac{1}{2} \left( m_b^2 - 2m_b E_\nu - m_c^2 - m_\ell^2 \right) m_b E_\nu \quad (1.19)$$

The full derivation is given in Appendix A. The phase space, integrated over b- and c-momenta can be reduced to

$$d\Phi = \frac{1}{4(2\pi)^3} dE_\nu dE_\ell \quad (1.20)$$

The expression of the total decay rate becomes

$$\Gamma = \frac{4G_F^2}{(2\pi)^3} |V_{cb}|^2 \int \left( m_b^2 - 2m_b E_\nu - m_c^2 - m_\ell^2 \right) E_\nu dE_\nu dE_\ell \quad (1.21)$$

Where  $E = m_b$  in the b-quark center of mass frame. Working out the integral over the neutrino and  $\tau$  lepton energies, the total decay rate can be expressed as

$$\Gamma = \frac{G_F^2 m_b^5}{192\pi^3} |V_{cb}|^2 f_{ps} \quad (1.22)$$

where  $f_{ps}$  is the phase space factor, dependent on the masses  $m_b$ ,  $m_c$  and  $m_\ell$ . Its full expression is also given in Appendix A.

The individual b- and c-quark masses are not well known. More accurately measured is the



difference in mass [5]

$$m_b - m_c = 3.43 \pm 0.05 \text{ GeV} \quad (1.23)$$

This difference is used to calculate the phase space factors for the  $\tau$  lepton and the muon as a function of the b-quark mass, depicted in Figure 1.3. In addition it shows the ratio of phase space factors, which in the spectator quark model is equal to their branching fraction ratio. This ratio is found to be approximately 0.2 to 0.25, depending on the quark masses chosen.

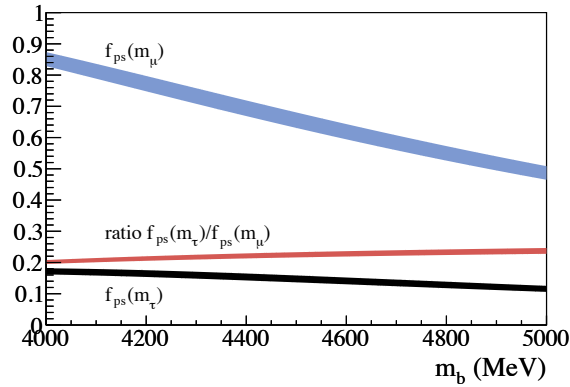


Figure 1.3: The phase space factors for the  $B^0 \rightarrow D^{*-} \tau^+ \nu_\tau$  decay, the  $B^0 \rightarrow D^{*-} \mu^+ \nu_\mu$  decay and their ratio as a function of the b-quark mass. The thickness of the bands represent the c-quark mass range from  $m_c = m_b - 3.48 \text{ GeV}$  to  $m_c = m_b - 3.38 \text{ GeV}$ .

### 1.3.2 The $B^0 \rightarrow D^{*-} \tau^+ \nu_\tau$ decay including QCD corrections

In reality the b- and c-quarks are confined by the strong interaction inside mesons; particles which consists of one quark and one anti-quark. The  $B^0$  meson consists of a down and a bottom quark, whereas the  $D^{*-}$  particle consists of a down and a charm quark:

$$B^0 = \{d, \bar{b}\} \quad \text{and} \quad D^{*-} = \{d, \bar{c}\} \quad (1.24)$$

The strong interaction is mediated by gluons, acting on quarks, anti-quarks and other gluons. These interactions, within and between mesons, have to be taken into account when calculating the decay rate. In semileptonic decays, a simplification comes from the fact that the leptonic current coupling to the W boson does not strongly interact with the hadronic current. Hence, the complication of additional gluon interactions is limited to the B and  $D^*$  mesons. This is illustrated in the Feynman diagram in Figure 1.4.

In the matrix element of Equation 1.18, the hadron current,  $H_\mu$ , complicated by strong inter-

### 1.3. Phenomenology of the semileptonic $B^0 \rightarrow D^{*-} \tau^+ \nu_\tau$ decay

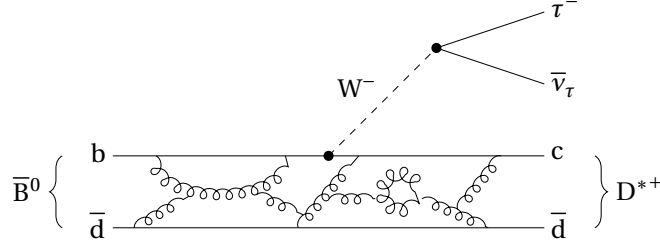


Figure 1.4: A Feynman diagram depicting the  $B^0 \rightarrow D^{*-} \ell^+ \nu_\ell$  decay, including QCD gluon interactions.

actions, is given by

$$H_\mu = \langle D^{*-} | \bar{\psi}_c \gamma_\mu (1 - \gamma^5) \psi_b | B^0 \rangle \quad (1.25)$$

The relatively model-independent heavy-quark effective theory (HQET) can be used to determine the matrix element for the decay. HQET is a theoretical approach used to describe meson systems that contain one heavy quark ( $b$  or  $c$ ) and one light quark ( $u$ ,  $d$  or  $s$ ). The  $b$ - and  $c$ -quark masses are much larger than  $\Lambda_{\text{QCD}}$ , the characteristic energy scale of QCD quark binding. As the momentum exchanges in mesons due to the strong force are of the order  $\Lambda_{\text{QCD}}$ , the change in velocity of a heavy quark during an interaction is approximately  $\Lambda_{\text{QCD}}/m_q$ , with  $q \in \{c, b\}$ . In the limit where  $m_q \rightarrow \infty$ , the heavy quark's velocity is therefore conserved. And in this limit, the heavy quark spin does not interact with the gluon field. Heavy quarks of different flavours and spins can thus be treated identically. This is called the heavy quark spin-flavour symmetry. Analogous to the electron and proton in the hydrogen atom, the assumption is that the light quark in the heavy-light meson is independent of the heavy quark kinematics, up to hyperfine corrections. Such corrections manifest themselves, for example, as the mass splittings between pseudoscalar and vector mesons such as  $\delta m = m_{D^*} - m_{D^0}$ .

The hadronic uncertainties are all due to the coupling of the final state charm quark with the spectator light quark. The probability of a particular final state configuration is parameterized by form factors. When the heavy quark decays it acquires motion relative to its initial state. For a given transferred momentum,  $q^2$ , from the  $b$ -quark to the lepton-neutrino system, the form factor describes the likeliness of the light quark and the moving heavy quark reassembling into a particular final state.

A key result of HQET is that, in the heavy quark symmetry limit, all decays from one light-heavy meson to another light-heavy meson can be described in a single common form factor. Dominated by heavy quark kinematics, the form factor does not depend on the light quark nor does it depend on flavour. This common form factor is called the Isgur-Wise function [6].

From Lorentz invariance one finds the decomposition of the hadronic current in terms of

## Chapter 1. Theory

---

form factors. The HQET preferred parameterization is given by [7]

$$H_\mu = \sqrt{m_B m_{D^*}} [ i h_V(\omega) \epsilon_{\mu\nu\alpha\beta} \epsilon^{*\nu} v_B^\alpha v_{D^*}^\beta - h_{A_1}(\omega)(\omega+1)\epsilon_\mu^* + h_{A_2}(\omega)\epsilon^* \cdot v_B v_{B\mu} + h_{A_3}(\omega)\epsilon^* \cdot v_B v_{D^*\mu} ] \quad (1.26)$$

With  $\epsilon$  the polarisation vector of the vector meson. The form factors  $h_i$ , with  $i \in \{V, A_1, A_2, A_3\}$ , are expressed in terms of  $\omega = v_B \cdot v_{D^*}$ , because velocity is a conserved quantity in the  $m_q \rightarrow \infty$  limit.

In the infinite quark-mass limit, the spin-flavour symmetry of the quarks relates these form factors to a single universal function  $\xi(\omega)$ .

$$\lim_{m_q \rightarrow \infty} h_i = \alpha_i \xi(\omega) \quad (1.27)$$

with coefficients

$$\alpha_V = \alpha_{A_1} = \alpha_{A_3} = 1 \quad \text{and} \quad \alpha_{A_2} = 0 \quad (1.28)$$

This function is the Isgur-Wise function and is independent of the heavy quark masses. The shape of  $\xi(\omega)$  is not predicted by HQET. However, its value at  $\omega = 1$  is well defined. In this case, at which  $v_B = v_{D^*}$  and there is no relative motion between the initial and the final heavy quark, the light quark is insensitive to the decay and therefore

$$\xi(1) = 1 \quad (1.29)$$

Outside the heavy-quark symmetry limit, the current can no longer be described by the Isgur-Wise function. In order to take the hyperfine corrections in powers of  $\Lambda_{\text{QCD}}/m_b$  and  $\Lambda_{\text{QCD}}/m_c$  into account, the Isgur-Wise function is replaced by a form factor denoted by  $\mathcal{F}(\omega)$ , which at  $\omega = 1$  is shifted away from unity due to the corrections. An important advantage of the  $B^0 \rightarrow D^{*-} \ell^+ \nu_\ell$  decay mode is that the first order corrections to  $\mathcal{F}(1)$  vanish as a consequence of Luke's theorem [8]. As a result,  $\mathcal{F}(1)$  is theoretically known to about the 5% level [9]:

$$\mathcal{F}(1) = 0.927 \pm 0.024 \quad (1.30)$$

The determination of the shape of  $\mathcal{F}(\omega)$  is however model dependent. And therefore there is no unique answer to what the SM  $\mathcal{B}(B^0 \rightarrow D^{*-} \tau^+ \nu_\tau) / \mathcal{B}(B^0 \rightarrow D^{*-} \ell^+ \nu_\ell)$  ratio is.

In 1989 J.G. Körner and G.A. Schuler considered the spectator quark model to determine the ratios [10]

$$\mathcal{B}(B^0 \rightarrow D^{*-} \tau^+ \nu_\tau) / \mathcal{B}(B^0 \rightarrow D^{*-} e^+ \nu_e) = 0.2519 \quad (1.31)$$

$$\mathcal{B}(B^0 \rightarrow D^{*-} \tau^+ \nu_\tau) / \mathcal{B}(B^0 \rightarrow D^{*-} \mu^+ \nu_\mu) = 0.2529 \quad (1.32)$$

In 2000 D.S. Hwang and D.-W. Kim determined a model independent ratio, by using the CLEO experimentally determined form factors from 1997 [11]. They came to a ratio of

$$\mathcal{B}(B^0 \rightarrow D^{*-} \tau^+ \nu_\tau) / \mathcal{B}(B^0 \rightarrow D^{*-} e^+ \nu_e) = 0.256_{-0.013}^{+0.014} \quad (1.33)$$

The latest theoretical prediction of the ratio comes from C.-H. Chen and C.-Q. Geng in 2006 [12]. Using the light-front quark model (LFQM), they determine the different branching fraction which leads to a ratio of

$$\mathcal{B}(B^0 \rightarrow D^{*-} \tau^+ \nu_\tau) / \mathcal{B}(B^0 \rightarrow D^{*-} \ell^+ \nu_\ell) = 0.2518 \pm 0.0181 \quad (1.34)$$

### 1.3.3 Current measurements

The BaBar collaboration has measured the branching fraction of  $B^0 \rightarrow D^{*-} \tau^+ \nu_\tau$  to be [13]

$$\mathcal{B}(B^0 \rightarrow D^{*-} \tau^+ \nu_\tau) = (1.62 \pm 0.31 \pm 0.10 \pm 0.05)\% \quad (1.35)$$

Previously the Belle experiment had reported [14]

$$\mathcal{B}(B^0 \rightarrow D^{*-} \tau^+ \nu_\tau) = (2.02_{-0.37}^{+0.40} \pm 0.37)\% \quad (1.36)$$

A new preliminary result on the observation of the  $B^0 \rightarrow D^*(2010)^{\mp} \tau^{\pm} \nu_\tau$  decay was presented by the BaBar collaboration at the Europhysics Conference on High-Energy Physics 2011 (EPS 2011) [15]. Normalised to the equivalent semi-muonic decay, which is well-measured to be  $\mathcal{B}(B^0 \rightarrow D^{*-} \mu^+ \nu_\mu) = (5.11 \pm 0.23)\%$  [5], the updated study results in a fraction of

$$\mathcal{R}(D^*) = \mathcal{B}(B^0 \rightarrow D^{*-} \tau^+ \nu_\tau) / \mathcal{B}(B^0 \rightarrow D^{*-} \mu^+ \nu_\mu) = 0.356 \pm 0.038 \pm 0.032 \quad (1.37)$$

This result is separated by  $\sim 2\sigma$  from the theoretical predication given in Equation 1.34.

## 1.4 New Physics possibilities

Despite the fact that the Standard Model is the most successful theory describing particle interactions, it is incomplete. It is believed that it must be replaced by a more fundamental theory at high energy scales. Any new physics occurring at this higher energy scale will generate low energy effective couplings that contribute to SM processes. Thus, by measuring deviations from Standard Model predictions, signatures of new physics can be studied.

There are numerous New Physics (NP) models. Semileptonic B decays are used to analyse possible couplings beyond the SM  $V - A$  coupling. However, one of the most compelling reasons to search for the exclusive  $B^0 \rightarrow D^{*-} \tau^+ \nu_\tau$  decays is that it can be used to constrain classes of models with scalar interactions, such as those which arise in models with extended Higgs sectors. This decay channel is potentially sensitive to a charged Higgs boson, as the tree

level  $b \rightarrow c \ell \nu_\ell$  process can be mediated by an  $H^\pm$  instead of a  $W^\pm$ . Since the Higgs coupling is proportional to the particle masses, this effect may be observed in semileptonic  $B \rightarrow X \tau \nu_\tau$  decays and remain unobserved in other semileptonic modes.

The contribution of a charged Higgs to the  $B^0 \rightarrow D^{*-} \tau^+ \nu_\tau$  decay has been studied [16]. Figure 1.5 shows the ratio of branching fractions  $\mathcal{B}(B^0 \rightarrow D^{*-} \tau^+ \nu_\tau) / \mathcal{B}(B^0 \rightarrow D^{*-} \mu^+ \nu_\mu)_{\text{SM}}$  depending on the charged Higgs mass and assumes no new physics contribution in the muon decay. The undetermined ratio of the vacuum expectation values of the neutral Higgs fields, is given by  $\tan \beta$ . The bands depict a measurement uncertainty in the Isgur-Wise function.

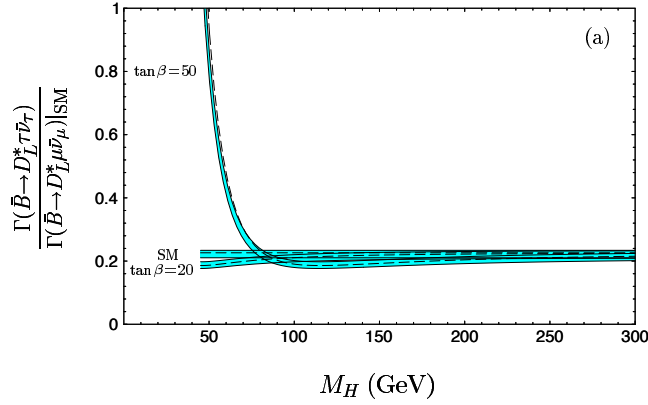


Figure 1.5: The branching ratio of  $\mathcal{B}(B^0 \rightarrow D^{*-} \tau^+ \nu_\tau) / \mathcal{B}(B^0 \rightarrow D^{*-} \mu^+ \nu_\mu)_{\text{SM}}$  depending on the charged Higgs mass for  $\tan \beta = 20$  and  $\tan \beta = 50$  [16].

## 1.5 Conclusion

The branching ratio  $\mathcal{B}(B^0 \rightarrow D^{*-} \tau^+ \nu_\tau) / \mathcal{B}(B^0 \rightarrow D^{*-} \mu^+ \nu_\mu)$  is a measurement sensitive to physics beyond the Standard Model. These NP contributions are expected to be large in the tauonic B decay due to the larger coupling of the charged Higgs boson to the  $\tau$  lepton, relative to the muon. The Standard Model prediction of this ratio, based on measured form factors, is  $0.25 \pm 0.02$  [12]. A measurement different from this value would be a strong indicator of new physics.  $\mathcal{B}(B^0 \rightarrow D^{*-} \mu^+ \nu_\mu)$  has been well measured. The study of  $\mathcal{B}(B^0 \rightarrow D^{*-} \tau^+ \nu_\tau)$ , which is started in this thesis, will determine the existence of NP contributions in this decay process.

## 2 The LHCb experiment

The LHCb experiment is a precision experiment dedicated to studying b-hadron decays at CERN's Large Hadron Collider (LHC) [17]. Figure 2.1 shows a side-view schematic of the LHCb detector with a right-handed coordinate system: the interaction point is defined as the origin, the  $z$ -axis is defined as the beam axis and the  $y$ -axis is pointing upwards. LHCb is a single arm spectrometer covering an angle of 10 mrad to 250 or 300 mrad, vertically or horizontally respectively. LHCb is designed as a spectrometer due to the angular distribution of b-hadron decays, which occur predominantly in either forward or backward direction.

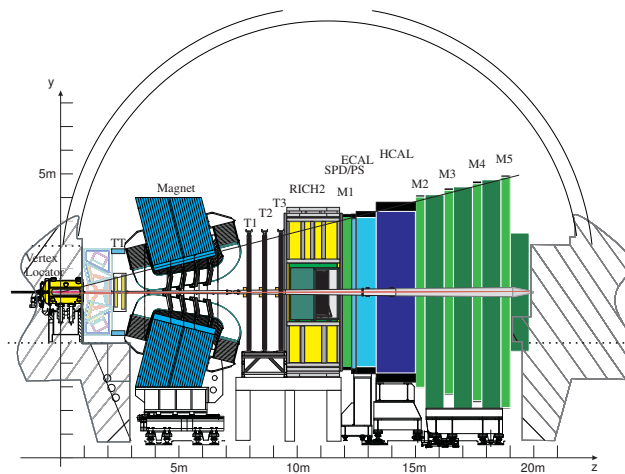


Figure 2.1: Schematic diagram of the LHCb detector [17].

The b-hadron decays studied by the LHCb experiment are produced in proton-proton collisions of the LHC. The LHCb detector is designed to operate at a nominal luminosity of  $2 \cdot 10^{32} \text{ cm}^{-2} \text{ s}^{-1}$  in order to collect  $2 \text{ fb}^{-1}$  of data in a nominal year based on a  $b\bar{b}$ -quark production cross section of  $500 \mu\text{b}$  at 14 TeV centre-of-mass energy collisions.

In 2010 and 2011 the LHC has delivered collisions with a centre-of-mass energy of  $\sqrt{s} = 7 \text{ TeV}$ .

## Chapter 2. The LHCb experiment

---

During 2010 approximately  $35 \text{ pb}^{-1}$  of data was collected by the LHCb experiment. Using these data the  $b\bar{b}$ -quark production cross section was measured to be  $(75.3 \pm 5.4 \pm 13.0) \mu\text{b}$  [18]. In the first half of 2011 an abundance of  $370 \text{ pb}^{-1}$  of data was added to this collection. In this thesis, both the data collected in 2010 and before the summer of 2011 are used to study the  $B^0 \rightarrow D^{*-} \tau^+ \nu_\tau$  decay.

The subset of  $B^0 \rightarrow D^{*-} \tau^+ \nu_\tau$  decays is studied where the  $\tau^+$  particle decays as  $\tau^+ \rightarrow \pi^+ \pi^+ \pi^- \bar{\nu}_\tau$  and the  $D^{*-}$  particle is required to decay as  $D^{*-} \rightarrow \bar{D}^0 \pi^-$ , with  $\bar{D}^0 \rightarrow K^+ \pi^-$ . The considered  $B^0 \rightarrow D^{*-} \tau^+ \nu_\tau$  decay thus results in 5 charged pions and a charged kaon, which need to be reconstructed and identified in order to remodel the original decay. The LHCb experiment is designed to accurately determine the charge, momentum and type of all particles that traverse the detector.

A key component in the determination of charge and momentum is the LHCb dipole magnet. Traversing through the magnetic field,  $\vec{B}$ , causes the particle trajectory to deflect. A particle of charge  $q$  experiences a force of  $\vec{F} = q\vec{v} \times \vec{B}$ , where  $\vec{v}$  is the velocity of the particle. The direction of the bending reveals the charge of the particle, whereas its curvature is used to measure the momentum of the particle. Simplifying the conditions by assuming the particle traverses orthogonally through a constant field, the force experienced becomes  $F = qvB$ . This field causes the particle to follow a circular path of radius  $r$  and its motion is described by the relation  $p = B|q|r$ , where  $p$  is the momentum of the particle. The momentum  $p$  is thus proportional to the radius of the curvature. This thesis covers the parameterization of the LHCb magnetic field. This field description is used for all LHCb analyses. The magnetic field and its parameterization are described in more detail in Section 2.1.

In order to measure the curvature of the particle trajectory caused by the magnetic field, a tracking system is needed. The LHCb Silicon Trackers (ST) and Outer Tracker (OT) record the exact position of all traversing charged particles before and after the magnet. This part of the tracking system is described in Section 2.2. In order to achieve high accuracy in the trajectory measurements, the tracking detectors are divided into hundreds of thousand detecting elements or strips. A particle traversing through LHCb will only be registered by a few of these detection strips. Therefore only the information of those strips that detected a signal is stored. The process of this so-called zero-suppression of the raw data for the LHCb ST is described in Section 2.3. This thesis covers the offline emulation of the noise reductive Field-Programmable Gate Array (FPGA) algorithms used for the zero-suppression. The tests performed using the emulator have resulted in bit-perfect agreement between the online and offline clusterisation algorithms.

While the magnetic field and the tracking system are used to determine the momentum of a particle, its energy is measured by calorimeters. All particles, except for muons, are absorbed in the calorimeters, where the energy released during their absorption is measured. Besides the measurement of energy, the LHCb calorimeters are also used to distinguish between photons, electrons and hadrons. In addition, low-level trigger decisions are based on its fast

transverse energy estimations. To identify and measure muon tracks, a muon tracking system is installed downstream of the calorimeters.

In principle, the particles traversing LHCb can be identified and reconstructed using the named subdetectors. However, the LHCb experiment also houses two Ring Imaging Cherenkov (RICH) detectors. These detectors can identify particles of different masses by measuring their velocity, provided their momentum is known. The RICH system is especially designed to distinguish charged pions from kaons and protons. This ability enables the accurate identification of the numerous particles originating from hadronic collisions. The particle identification detectors are described in Section 2.4.

Because LHCb is dedicated to studying b-hadron decays, it is important to accurately measure the production and decay positions of a particle. After being created in a proton-proton collision, the B meson typically flies a centimeter before decaying. The LHCb Vertex Locator (VELO) is designed to distinguish these secondary vertices from the primary vertices with great precision. The VELO tracking detector is described in more detail in Section 2.5.

The design frequency of two proton bunches crossing at the LHCb interaction point is 40 MHz. Approximately 10 MHz of these bunch crossings will result in collisions with particles inside the LHCb acceptance region. Only a fraction of these collisions contain B meson decays that are of interest to the LHCb physics program. The event rate that can be recorded is limited by the offline computing capacity of 2 kHz. A triggering system is in place to efficiently select those events which contain B decays of interest. The LHCb Trigger is described in Section 2.6.

## 2.1 Magnetic field

The bending power of the magnet is represented by the integrated field, which is approximately  $\int B \cdot dl = 4 \text{ Tm}$  when integrated over the detector length in  $z$ -direction. With the  $xz$ -plane the main bending plane of the experiment,  $B_y$  is the main field component. To eliminate asymmetry effects caused by detector systematics, this component can be chosen to be either positive or negative, corresponding to upward or downward polarity, respectively. Figure 2.2 shows the values for each of the field components of the upward polarity field versus the  $z$ -axis.

The upward and downward polarity field have the same values but with opposite sign. A simple and accurate parameterization method which can be equally applied on both upward and downward polarity measurements is used to map the magnetic field values. The method has been shown to be robust by obtaining consistent results when applying the exact same method on different data sets. This magnetic field parameterization, described in 2.1.1, has indeed shown that a single field map can be used for both polarities. This result has been implemented and is used for all current LHCb physics analyses.



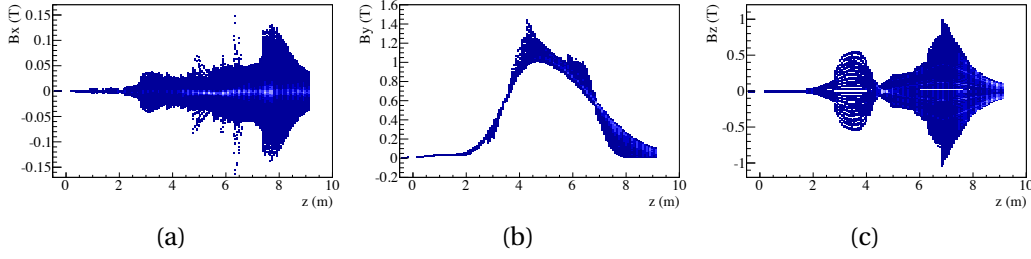


Figure 2.2: Values of the (a)  $B_x$ , (b)  $B_y$  and (c)  $B_z$  measured field shapes versus  $z$ -axis.

### 2.1.1 Magnetic field parameterization

The magnetic field parameterization is based on measurements taken in December 2005 [19]. These measurements do not cover the full acceptance region of the detector and extrapolation is needed to determine the field values in these areas. Using the simulation model TOSCA [19, 20] field values are calculated which do cover the full acceptance of LHCb. The magnetic field parameterization of LHCb is a realistic description based on both data measurements and calculated field values to regulate the extrapolation. The parameterization covers the full acceptance region.

**Parameterization of residuals.** High order polynomials are needed to accurately describe the measured field as a function of space coordinates but induce large errors when extrapolated. Therefore it is chosen to parameterize residuals: the differences between measured values and calculated values. The residuals are generally described by smooth, continuous functions which parameterization requires lower order polynomials and extrapolates in a controlled manner.

**Construction of the residuals.** Calculated magnetic field values are available on a grid of  $100 \times 100 \times 100 \text{ mm}^3$ . The field must be determined on the measurement coordinates in order to calculate the residuals between the calculated and measured values. For each measurement a surrounding cube of 27 calculated values is selected. These values are then interpolated onto the measurement coordinate. The 3D polynomial fit function TMultiDimFit [21] is used with polynomials of order 2 to perform this interpolation. The interpolated values are independent of polarity (up to their sign) and can be used to calculate the field residuals on the measurement coordinates.

**Fit method and regions.** The parameterization of the residuals is performed per field component  $-B_x$ ,  $B_y$  and  $B_z$  and is divided up in 11 areas of different  $z$ -coordinate. An overlap in fitting regions ensures small discrepancies on the boundaries. All four quadrants of the coordinate system are fitted simultaneously. The residuals are fitted using TMultiDimFit. Restricting

the polynomials to an order of 3 or 4 per dimension is sufficient to obtain good agreement between the residual values and the parameterization without introducing uncontrolled extrapolation.

Due to the small number of measurements for  $z < 2.8$  m, those measurements outside the LHCb acceptance region are included to improve fit results. For regions with larger  $z$ -coordinate, measurements up to 10 cm outside the acceptance region are included to improve fit results at the boundary of the acceptance region.

**Extrapolation in  $z$ -coordinate.** Data measurements are taken up to  $z = 9.1$  m, but an accurate field description is required up to  $z = 14$  m. Extrapolation is not relied upon to describe the magnetic field between  $z = 9.1$  m and  $z = 14$  m. Instead, the residuals are taken at  $z = 9$  m where the fit is accurate and zero field is assumed at  $z = 14$  m and beyond. Between these points the residuals are reduced as a linear function of  $z^4$ , as that is the best match visually found (Figure 2.3). The advantage over using calculated simulation values is that this method ensures a smooth transition and avoids discontinuities in the parameterized field at  $z = 9.1$  m.

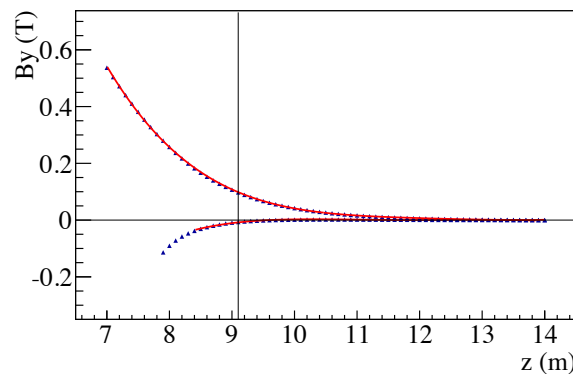


Figure 2.3: The upward polarity parameterization results for  $z > 7$  m and  $(x, y) = (100, 10)$  cm (upper measurements) and  $(x, y) = (100, 200)$  cm (lower measurements).

**LHCb software grid.** The LHCb software works with magnetic field values on a discrete grid of  $100 \times 100 \times 100$  mm<sup>3</sup> in space. The magnetic field values on the coordinates of this grid are determined during the parameterization and stored directly into a field map and used by the LHCb reconstruction software.

**Schematic overview.** Figure 2.4 schematically depicts the steps of the parameterization.

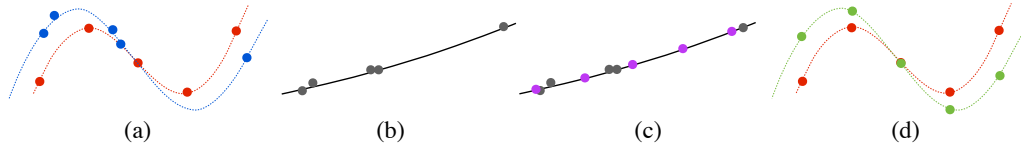


Figure 2.4: (a) Calculated values (red) and measured values (blue). (b) The residuals between calculated and measured values and their parameterization (grey) and in (c) in addition the residuals on the simulation coordinates (magenta). (d) The calculated values (red) and the final parameterized field values (green).

### 2.1.2 Parameterization results and comparison

In order to determine the accuracy of the field parameterization, it is necessary to know the measurement error. The discrepancies between different measurements taken at the same space coordinates have determined the measurement error to be in the order of  $10^{-3}$  Tesla for both the upward and downward polarities. In addition, the absolute differences between upward and downward polarity measurements show the same distributions as measurement error distributions of a single polarity.

The parameterized map is validated by the differences between measurement and parameterized values. The distributions of these differences for the different field components and their magnitude are of the order of the measurement error. In addition, the discrepancies at the boundaries between different fit regions are also of the order of the fit accuracy or less.

Fitting residuals smooths out small fluctuations in the calculated values. However, those fluctuations are later reintroduced by adding the calculated values to the fitted residuals. The fluctuations in the calculated values will therefore remain.

The distribution of differences between parameterized values of the upward and downward polarities are fitted using double Gaussians. The result shows discrepancies of the order  $10^{-3}$  T or  $10^{-4}$  T for the inner Gaussian fits. The results of the fits are given in Table 2.1 and superimposed for all components in Figure 2.5. The agreement between the upward and downward polarity parameterizations is consistent with the agreement in measurement between the two polarities.

Table 2.1: The fit results of the differences between parameterized values of the upward and downward polarities for (a)  $\delta B_x$ , (b)  $\delta B_y$ , (c)  $\delta B_z$  and (d)  $\delta|B|$  for  $z < 9.1$  m.

	single Gaussian deviation	double Gaussian		
		inner deviation	outer deviation	inner/outer (%)
$\delta B_x$	$8.0 \cdot 10^{-4}$	$3.0 \cdot 10^{-4}$	$1.3 \cdot 10^{-3}$	47/53
$\delta B_y$	$4.2 \cdot 10^{-4}$	$3.7 \cdot 10^{-4}$	$3.0 \cdot 10^{-3}$	73/27
$\delta B_z$	$5.6 \cdot 10^{-4}$	$4.1 \cdot 10^{-4}$	$3.1 \cdot 10^{-3}$	67/33
$\delta B $	$4.0 \cdot 10^{-4}$	$3.7 \cdot 10^{-4}$	$3.4 \cdot 10^{-3}$	73/27

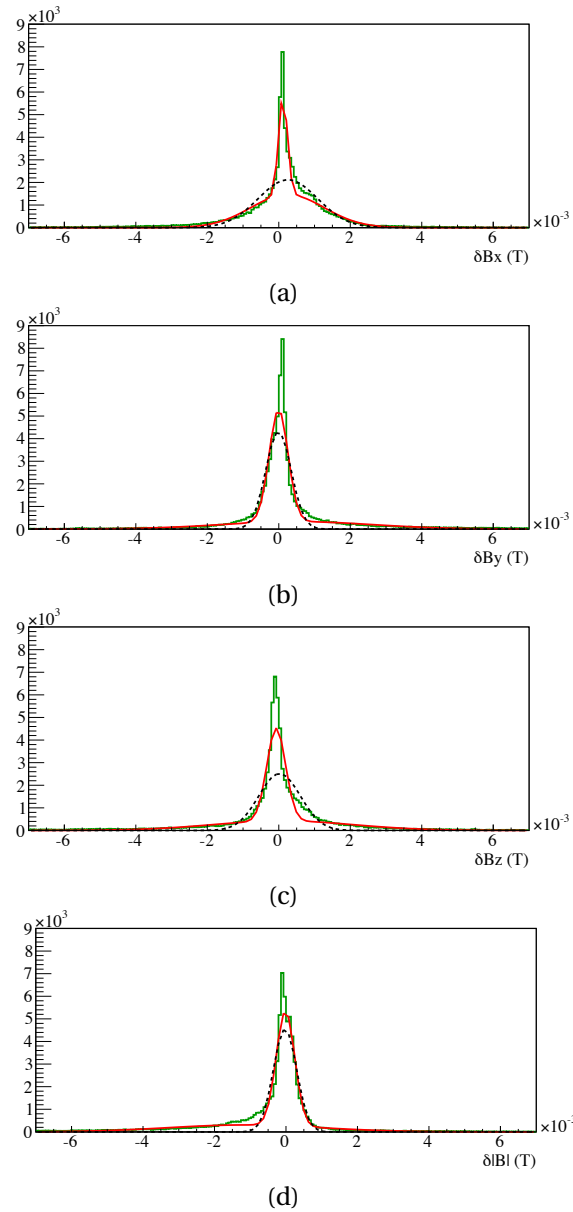


Figure 2.5: The differences between parameterized values of the upward and downward polarities for (a)  $\delta B_x$ , (b)  $\delta B_y$ , (c)  $\delta B_z$  and (d)  $\delta |B|$  for  $z < 9.1$  m, plus corresponding Gaussian fit results in black dotted line and double Gaussian fit results in red solid line.

The amount of deflection on the particle trajectory depends on the integrated field. From the interaction point, the magnetic field is integrated over paths with initial slopes  $t_x$  in  $x$ -direction and  $t_y$  in  $y$ -direction ranging between  $[-0.3, 0.3]$  rad and  $[-0.25, 0.25]$  rad, respectively, matching the acceptance region. The integrated  $Bdl_x$  component is depicted as a function of these slopes in Figure 2.6 for the upward and downward parameterizations as well as for

the simulation values up to  $z = 9.1$  m, as this is the region of the parameterization based on measurements. The integrated field  $Bdl_x$  component of the simulation values is significantly higher than those using either the (flipped-sign) upward or downward parameterization, which show similar results.

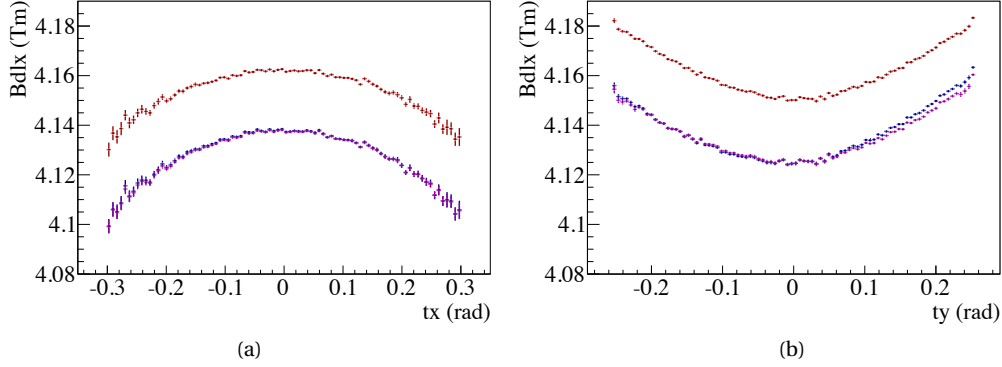


Figure 2.6: The integrated field component  $Bdl_x$  (Tm) vs (a)  $t_x$  and (b)  $t_y$  (rad) for the calculated field (red, top curve) and upward (blue) and downward (magenta) parameterized field based on data measurements (bottom curves).

The  $Bdl_x$  component is mainly dependent on the  $B_y$  component of the field and to a lesser degree on the  $B_z$  component. The quadrant comparison of the field components show a mirror symmetry along the  $y$ -axis, but an asymmetry along the  $x$ -axis for the  $B_y$  and the  $B_z$  component. This is consistent with the integration results depicted in Figure 2.6. It is difficult to explain where the difference between upward and downward polarity comes from for  $t_y > 0$ .

An important conclusion of this work is that a single parameterization adequately describes both the upward and downward polarities with a simple sign inversion. The reconstruction of LHCb data taken since the beginning of 2010 has been performed using the parameterization derived from the described fit to the combined upward and downward polarity data so to obtain highest precision. The momentum and hence mass resolution of the LHCb spectrometer is dependent this work, notably in the world best B meson mass measurements [22].

## 2.2 Tracking system

The main LHCb tracking system comprises four tracking stations. The first station is named the Tracker Turicensis (TT) and is located in the fringe field upstream of the magnet. The other three stations (T1-T3) are located downstream of the magnet and are spread over a distance of approximately two meters. These three stations are divided into two subdetectors: an Inner Tracker (IT) and an Outer Tracker (OT). The IT is situated around the beam pipe and deals with the higher occupancy region. The OT covers the remainder of the LHCb acceptance region. The tracking system employs two different detector technologies. The TT and the IT

use silicon microstrip detectors, whereas the OT uses straw-tube drift chambers. Their more detailed specifications are discussed in Sections 2.2.1-2.2.4.

### 2.2.1 Tracker Turicensis

The TT subdetector, situated upstream of the LHCb dipole magnet, is constructed of two sets of two layers, which consist of silicon microstrip detectors. The first two layers (TTa) are separated from the last two layers (TTb) by a distance of 27 cm. All layers cover the nominal acceptance region of the LHCb experiment. The TT subdetector has the approximate spatial dimensions of  $150 \times 130$  cm in order to fulfil the full acceptance requirement. The outer two layers have a vertical strip geometry ( $x$ -layers), whereas the second and the third layer are rotated by a stereo angle of  $+5^\circ$  and  $-5^\circ$ , respectively ( $u/v$ -layers). This geometry provides accurate tracking information in the  $xz$ -bending plane of the particle. The rotated layers enable positioning in the  $y$ -direction, with worse resolution than that for the  $x$ -direction.

The layout of the detection layers is based upon the use of 9.64 cm wide and 9.44 cm long silicon sensors with a readout strip pitch of  $183 \mu\text{m}$ . A readout sector consists of 512 data strips. The layers in the TTa subdetector consist of twelve modules, each constructed from fourteen sensors, which are positioned left and right of the beam pipe. In addition there are two so called half-modules, which consist of seven sensors, placed around the beam pipe. The TTb layers follow a similar structure, but is widened by an extra module on each side. The layout of the TTa and TTb  $x$ -layer is depicted in Figure 2.7. The colour coding illustrates which sensors are connected to the same readout sector.

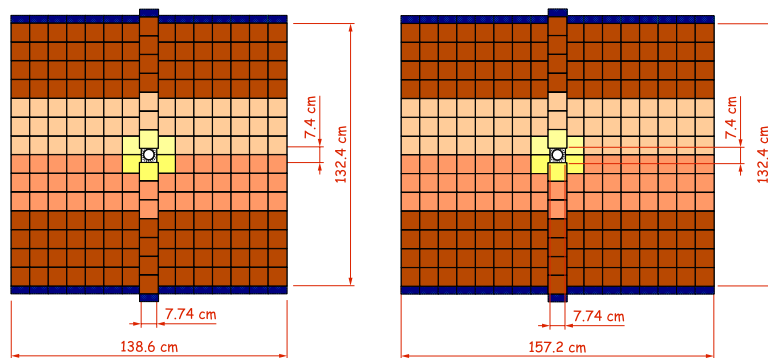


Figure 2.7: Layout of the  $x$ -layer in TTa (left) and in TTb (right).

### 2.2.2 Inner Tracker

The IT is located downstream of the LHCb dipole magnet. Its three tracking stations (T1-T3) are composed of four independent detector boxes. These boxes are positioned in a cross-shaped manner around the beam pipe and cover the  $120 \text{ cm} \times 40 \text{ cm}$  high occupancy region

of the LHCb acceptance. A detector box contains four detection layers which follow the  $xuvx$ -geometry, alike the configuration of the Tracker Turicensis detection layers. Each detection layer is divided into seven silicon strip ladders. One-sensor ladders are used in the top and bottom boxes, whereas two-sensor ladders compose the left and right boxes. The IT silicon sensors are 7.6 cm wide and 11 cm long and carry 384 readout strips with a strip pitch of 198  $\mu\text{m}$ . The sensors are connected to a readout sector of 384 data strips. The IT geometry is depicted in Figure 2.8.

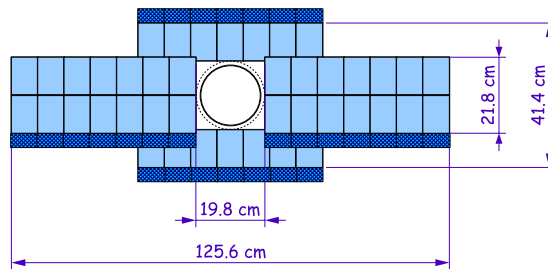


Figure 2.8: Geometry of an IT2  $x$ -layer.

### 2.2.3 Silicon Tracker readout

The electronic data from the Tracker Turicensis (TT) and Inner Tracker (IT) of the LHCb experiment are transmitted from the front-end read-out chips, called Beetles, of the detector to the data acquisition boards called TELL1s. A TELL1 can process the data of 3072 readout strips, which is equivalent to the readout of 24 Beetle chips, which is composed of 128 readout strips each. The raw unprocessed data that are collected by the TELL1s are called non-zero-suppressed (NZS) data. The main task of the TELL1 boards is the clustering of this NZS data.

The first two TT layers are built from 33.792 silicon microstrips and thus each require 11 TELL1s to manage their readout. The second two layers both consist of 37.888 strips, corresponding to 13 TELL1s per layer. A total of 48 TELL1 boards is used to process the full data information from the 143.360 readout strips. The combined IT layers result in a total of 129.024 readout strips. Each IT station is read out by 14 TELL1s, resulting in a total of 42 TELL1s needed for the full IT data acquisition.

Data acquired by a front-end Beetle is divided into 4 analog links (A-Links) of 32 data strips. These 32 data strips are preceded by 3 header words, which are also part of the same link, as shown in Figure 2.9. The value of a header word is either significantly higher or lower than the average signal on a data strip and is therefore considered as either positive or negative. The header words are used to encode event information, e.g. the pipeline column number (PCN), which identifies the position of an event in the pipeline of the Beetle chip. The full NZS bank

## 2.3. Emulation of the ST TELL1 algorithms

data format of the ST is described in [23].

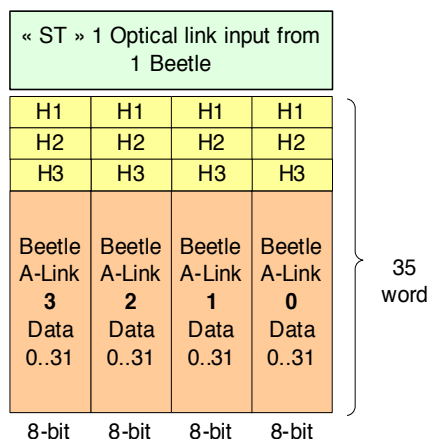


Figure 2.9: ST input data format received from the ADC cards.

### 2.2.4 Outer Tracker

The Outer Tracker (OT) is the second of the two tracking subdetectors behind the LHCb dipole magnet and covers the part of the LHCb acceptance that is not covered by the Inner Tracker (with a small overlap of about 1 mm). The boundaries between the IT and the OT have been chosen such that the expected mean occupancy in the hottest region of the OT is limited to below 10%. Contrary to the other tracking subdetectors, the Outer Tracker is a gas detector and is composed of 5.0 mm outer diameter (4.9 mm inner diameter) straw drift-tubes. They are mounted with a pitch of 5.25 mm. The OT consists of three stations made up from four layers, which in turn are composed of a left- and a right-half, each consisting of nine modules. Each OT module consists of two staggered layers (monolayers) of 64 tubes aligned vertically. There are two types of modules: short modules are located above and below the beam pipe and the IT boxes and long modules extend the entire height of the subdetector (4.85 m). Each OT layer consists of 8 short and 14 long modules. The orientation of the layers follows the same stereo angle configuration as the ST subdetectors. The complete OT detector with all three stations comprises approximately 55.000 single straw channels. These straws are filled with an Ar/CO<sub>2</sub> (70%/30%) mixture. This gas mixture enables a fast drift time (approximately 40 ns) and a drift-coordinate resolution of 200  $\mu\text{m}$  is achieved.

## 2.3 Emulation of the ST TELL1 algorithms

Each TELL1 board contains four Field Programmable Gate Arrays (FPGAs), which perform low-level tasks like noise reduction and clustering. The data output of the TELL1 is called zero-suppressed (ZS) data and only holds information on the clusters found in the data. The raw



data is also referred to as non zero-suppressed (NZS) data. Figure 2.10 shows the algorithms performed on the programmable FPGAs.

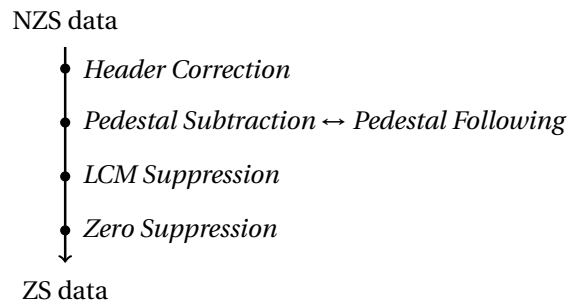


Figure 2.10: The flow diagram of the different algorithms applied on the NZS data in order to obtain ZS data.

Due to limited storage resources only the ZS output data of the TELL1s will be stored for further physics analysis and all NZS data will be lost. Therefore it is crucial to verify the functionality of the FPGA algorithms. In order to verify this functionality, an emulator has been developed and tested using simulated data as well as noise and test data from the detector.

The algorithms implemented in VHDL on the FPGAs have restricted complexity; for example, division is only possible through bit shifts. The emulator is coded in C++, but takes into account the firmware's restricted complexity concerning divisions and rounding differences.

### 2.3.1 Noise reduction algorithms

On the FPGAs three types of noise reduction are performed: Header correction, pedestal subtraction and LCM suppression.

The crosstalk between the header data and the data on the first strips of each link induces noise on these data strips. The origin of the crosstalk is not well understood. A header correction is applied on the affected strips. In addition, for each strip there is a positive offset in the signal, which fluctuates around an ADC count of 128 depending on strip number. An ADC count of 128 lies in the middle of the allowed range of 0-256 ADC. The offset is also referred to as the pedestal. The pedestal is calculated and updated using the pedestal following algorithm. The data is corrected for this pedestal value by its subtraction. After these corrections are applied for each individual strip, the noise induced by common mode is subtracted per link.

### Header correction

Crosstalk between the header data and the data on the first strips of each link can cause a pedestal shift on these strips. This causes the first strips to seem more noisy. A dependence has been observed between the number of strips affected by header crosstalk and the length of the cable used to transport the data. The IT cables range in length from 2.7 to 5.5 m and mainly the first two strips of each link suffer from header induced noise. The TT cables are 8 m in length and increased noise levels are visible up to the first six strips. For the implementation of the header correction on the TELL1, a header correction is needed which reduces the noise sufficiently, but takes into account the number of correction parameters.

The effect of header crosstalk can be reduced by applying a correction to the ADC counts of the affected strips, depending on whether the relevant headers are positive or negative. For each strip to be corrected, three dependencies are considered: the values (positive or negative) of the two last header words ([H2] and [H3] as depicted in Figure 2.9) per link and whether the PCN is odd or even. The PCN for a given Beetle is encoded in these last two header bits, as follows

$$\text{PCN} = 2^7 \cdot [H2, 3] + 2^6 \cdot [H3, 3] + \dots + 2^1 \cdot [H2, 0] + 2^0 \cdot [H3, 0] \quad (2.1)$$

where  $[Hx, y]$  is the  $x^{\text{th}}$  header of the  $y^{\text{th}}$  link and takes the value 0 for a negative header and 1 for a positive one. Whether the PCN is an odd or even number is therefore dependent on whether the last header of the first link ( $[H3, 0]$ ) is positive or negative. The header correction for each strip is thus dependent on the values of three header words, except for the strips in link 0 of the Beetle, where corrections depend on two header words. Eight corrections are used to reduce the header crosstalk induced noise on the first six strips of each link.

The eight corrections,  $c^{\pm\pm\pm}$ , applied are the difference between the average ADC count of the strip,  $\langle a \rangle$ , and the average ADC count of the same strip depending on whether the three relevant headers are positive or negative,  $\langle a^{\pm\pm\pm} \rangle$ , given by

$$c^{\pm\pm\pm} = \langle a^{\pm\pm\pm} \rangle - \langle a \rangle$$

The PCN also has a large influence on the common mode noise of the full Beetle. This noise contribution needs to be suppressed before the calculation of the value of  $\langle a \rangle$ . Figure 2.11 shows the average noise per strip over 96 Beetle analog links before and after applying header corrections for IT TELL1 8 and TT TELL1 35.

### Pedestal following and subtraction

The pedestal is the average ADC offset on a strip without signals applied. To start the pedestal calculation, an initial pedestal value,  $p_0$ , is assumed per strip. This can be an ADC of 128 for all strips or individually specified pedestal values from a conditions database. The initial pedestal

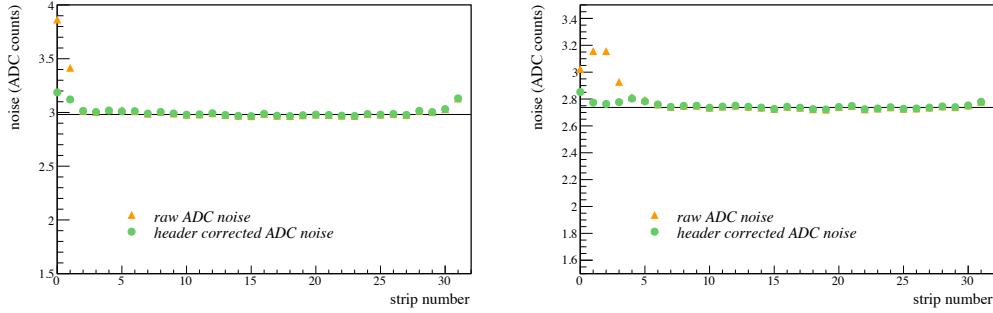


Figure 2.11: The average noise (over 96 Beetle analog links) per strip before (orange triangles) and after (green circles) applying header corrections for TELL1s (left) IT TELL1 8 and (right) TT TELL1 35.

sum is then defined as

$$\text{sum}_0 = 2^{10} \cdot p_0 \tag{2.2}$$

Every event the new pedestal value is calculated as

$$p_{i+1} = \frac{\text{sum}_{i+1}}{2^{10}} = \frac{\text{sum}_i - \text{sum}_i / 2^{10} + a_i}{2^{10}} \tag{2.3}$$

The mean pedestal (in its first iteration  $p_0$ ) is subtracted from the pedestal sum, while a newly measured offset,  $a_i$ , is added. The resulting sum is then divided by  $2^{10}$ , i.e. a bit-shift of 10 is applied, to obtain the updated pedestal value. Note that the offline emulator is purposely limited to using bit-shifts as the multiplication and division methods to accurately mimic the firmware. In each event the updated pedestals are subtracted from the data.

Figure 2.12 shows the pedestal value for a given strip as a function of the number of events used for its calculation. It shows that from an initial value of 128 ADC, the pedestal value converges to a value of 141 ADC, which is the true pedestal value.

To minimise the effect of a signal in the pedestal calculation, the update of the pedestal sum is limited to a maximum of 15 ADC per event. The signal thus has a minimal effect on the pedestal if its occurrence is infrequent. A constant signal may result in an overestimated pedestal value.

After performing the pedestal following, the correct pedestal value for each strip can be stored. If believed that the pedestal values do not vary over short periods of time, then the subtraction of the pedestals can be performed without the pedestal following on.

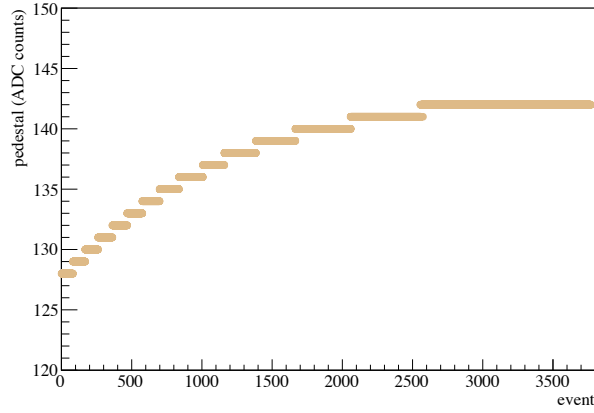


Figure 2.12: The pedestal value for a given strip dependent on the number of events used for its calculation.

### Linear common mode suppression

After the pedestal subtraction and header corrections, the data is corrected for common mode (CM) noise. The algorithm is performed per analog link (32 strips) and consists of the following steps:

1. Subtraction of the mean ADC count
2. Subtraction of a second refined mean where ADC values above a threshold are set to zero in order to exclude possible signal hits
3. Correction of the slope

This process sequence is depicted in Figure 2.13. As we are limited to the use of bit shifts instead of division, the mean must be calculated over 32 ( $2^5$ ) values. Therefore in the second mean calculation, possible hits are set to 0 instead of being left out of the calculation.

The slope,  $s$ , is calculated using the method

$$s = \frac{3 \cdot \sum_i (i - 16) \cdot a_i}{2^{13}}$$

where index  $i$  stands for the strip number ranging from 0 to 31 and  $a_i$  is the ADC count of strip  $i$ . Due to the limitation caused by programming in integers, two approximations are made

$$\langle i - 16 \rangle \sim 0$$

$$2^{13}/3 \sim \sum_i (i - 16)^2$$

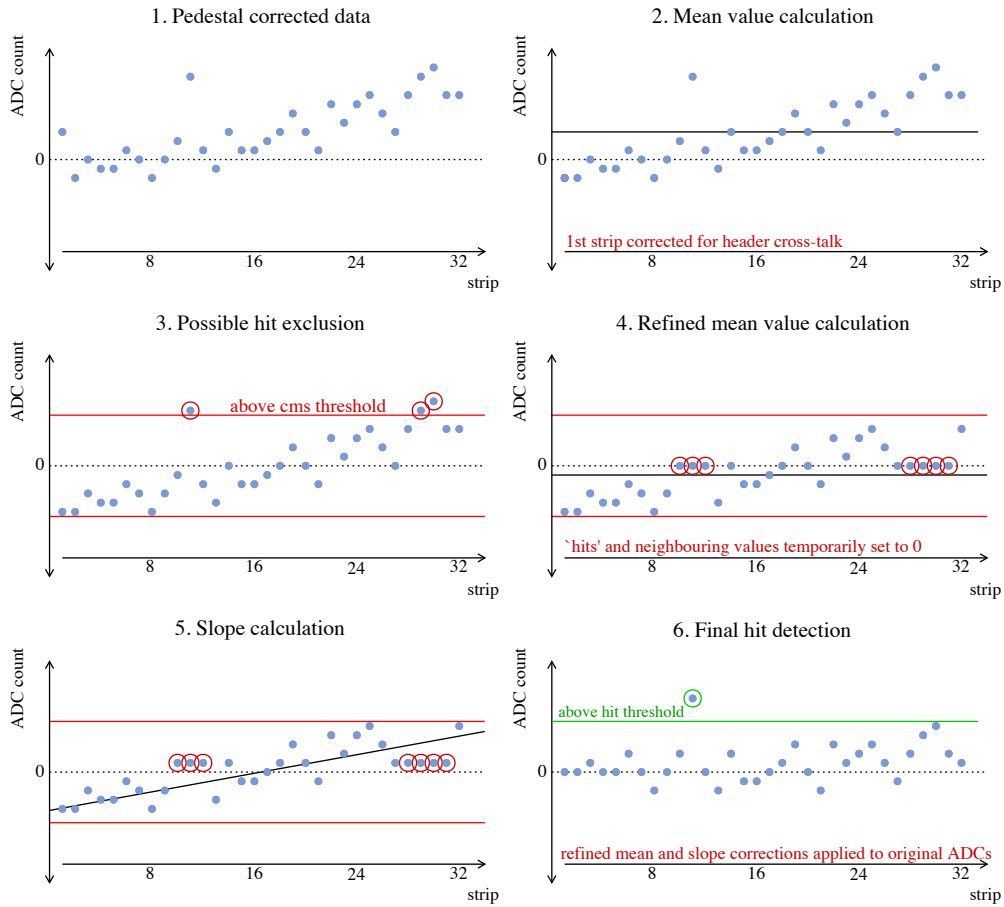


Figure 2.13: The ST linear common mode suppression algorithm. (1) The common mode suppression is applied on pedestal subtracted data. (2) The average ADC count of each link (32 strips) is calculated and subtracted. (3) Strips with an ADC values above CMS threshold (calculated per strip) are detected. (4) A second refined mean is calculated, with the possible hits and their neighbouring values set to 0. (5) A linear slope is calculated and corrected for. (6) The values which are above hit threshold (calculated per strip) are considered hits.

By estimating the slope in this manner the outer strips are weighted more than the inner strips. Therefore the noise in the outer strips is suppressed more, which causes a 'bumpy' structure in the noise distribution.

### 2.3.2 Clustering

Three thresholds are used in the Silicon Tracker clustering process after the noise subtraction.

## 2.3. Emulation of the ST TELL1 algorithms

---

1. *Hit threshold.* Hit thresholds are determined per strip and the ADC value of the strip must be above hit threshold in order for a strip to be part of a cluster. Its value typically ranges from 5 to 7 ADC.
2. *Sum threshold.* When a cluster is created, its total ADC count must be above sum threshold. The sum threshold can vary per half Beetle. Most thresholds are 7 to 9 ADC.
3. *Spill-over threshold.* The spill-over threshold is also set per half Beetle. Its value is considerably higher at around 25 ADC. When the total ADC count of a cluster exceeds the spill-over threshold, the spill-over bit of the cluster is set to 1. This information is used to discriminate between real clusters and clusters from previous bunch crossings.

The clustering is performed per Beetle. The TELL1 processes two Beetle halves simultaneously, looping over all strips, starting with the first strip of each Beetle half. A new cluster is created when the ADC value of a strip is above its hit threshold. If the ADC value of the following strip is also above its hit threshold, it is added to the existing cluster. A maximum of 4 strips are allowed per cluster, thereafter a new cluster is created. If a cluster is created, but its total charge is below the sum threshold, the cluster is discarded. Clusters can be created across Beetle half boundaries. When the ADC value of the first strip of the second Beetle half is above threshold, the TELL1 considers the last 3 strips of the first Beetle half and will create a cluster across the boundary where applicable. Only when the last 4 strips of the first Beetle half are all over hit threshold, the clustering process will be performed on each Beetle half separately.

### 2.3.3 Results from early data taking

#### **Pedestal stability**

A pedestal stability study has been performed to determine the need of real time pedestal following. Different samples of NZS data, collected over a time interval of 20 days, show minor pedestal shifts fluctuating around 0. The difference pedestal values is plotted in Figure 2.14.

Based on these results the pedestal following will not be performed real time by default. Pedestals will be read from a stored database and can be updated periodically.

#### **2010 data results**

The performance of the emulator was tested on 2010 data. In this case, the choice not to run pedestal following is essential as the NZS data that is used to verify the FPGA algorithms, is not stored every event. Over 40 runs were randomly selected between March and November 2010. Running over the first data file of each run approximately 20 million clusters were created in the TT and IT each.

The 20,940,733 clusters created in the TT were emulated perfectly. The exact same number of clusters was found, on exactly the same strips and with exactly the same total ADC counts. An

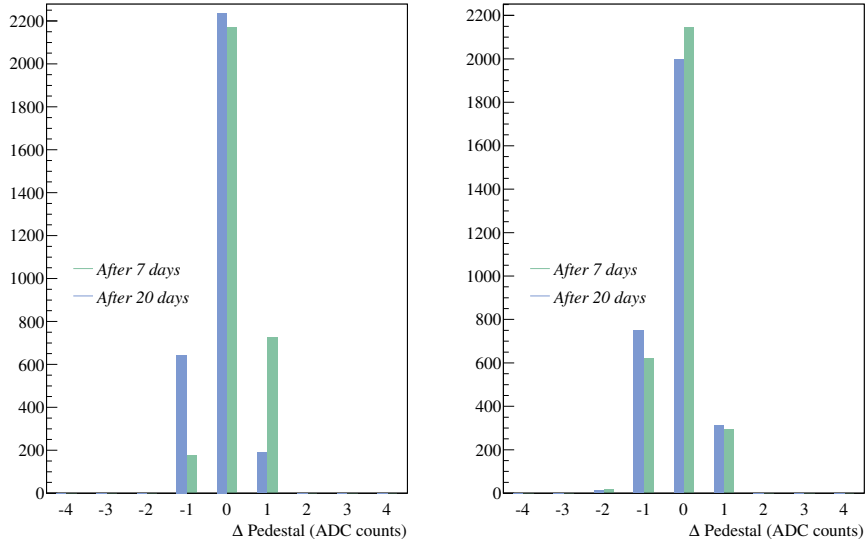


Figure 2.14: The difference in pedestal after 7 days (green) and 20 days (blue) for IT TELL1 13 (left) and TT TELL1 10 (right).

accuracy of 100%.

For the IT an inaccuracy of 0.025% was found. The clusters which were inconsistent between TELL1 and emulator were all created on 4 analog links. Of the clusters created on the three faulty links of TELL1 8, 87.3% was perfect, 12.4% contained the correct strips but with different charge and 0.3% was not created by the emulator. Of the clusters created on the faulty link of TELL1 64, 44.2% was perfect, 46.4% contained the correct strips but with different total ADC counts and 9.4% was not created by the emulator.

The 19,322,793 clusters created on all other analog links of the IT were created with 100% accuracy.

## 2.4 Particle identification

To distinguish between different particles and therefore identify different B decays, particle identification is required over a large momentum range for several types of particles. The LHCb particle identification system is divided into three sub-systems.

- The calorimeter system, subdivided into a Scintillator Pad Detector (SPD), a PreShower (PS), an electromagnetic calorimeter and an hadronic calorimeter. These subdetectors are optimised to identify hadrons, photons and electrons and to measure their energy.
- The muon detector, used for  $\mu$  identification.

- Two Cherenkov detectors (RICH1 and RICH2), which are designed for optimal  $\pi/K$  separation from a few GeV/c to  $\sim 100$  GeV/c.

### 2.4.1 Calorimeters

The calorimeter system measures the energy and the position of particles by their absorption. All particles, except muons, are absorbed in the calorimeters. Through the interaction of the incident particle with bulk material, its energy decreases and it is finally absorbed. The result is a shower of secondary particles, which on their turn loose energy in the bulk material until they are absorbed. The ionisations induced by this particle cascade excite atoms in the scintillator material, which emit scintillation light as they return to their ground state. The total amount of scintillation light in the shower is a measure for the initial energy of the particle.

The LHCb calorimeter system consists of the following detectors arranged in downstream direction

- A 15 mm thick Scintillating Pad Detector (SPD) which identifies charged particles. It is used to improve the rejection of neutral pion background with high transverse energy.
- A PreShower (PS) detector, which is a second 15 mm thick scintillating detector and follows a lead 12 mm thick plate. The PS identifies electromagnetic particles. This is particularly useful to reject the charged hadronic background in electron identification.
- An electromagnetic calorimeter (ECAL) to identify electrons and photons and to measure their energy. The ECAL uses the shashlik technology with 66 alternating layers of 2 mm thick lead and of 4 mm thick scintillator.
- An hadronic calorimeter (HCAL) to measure the energy of charged hadrons, in particular pions and kaons, and to measure their energy. The HCAL structure chosen is an iron-scintillating tile calorimeter read out by wave length shifting fibers. The scintillators are 4 mm thick and the iron plates are 16 mm thick. Its total thickness is 1.2 m.

### 2.4.2 Muon system

Muons traverse the full calorimeter system before being detected by the muon system. The muon system is used in the Level-0 trigger, described in Section 2.6, as well as in the offline event reconstruction. In the Trigger the muon system is used to identify the muons among the tracks found by the tracking stations and to select those muons with a high transverse momentum. This is achieved by performing a stand-alone muon track reconstruction and transverse energy estimation. The muon detector is equipped with 5 double layer ( $x$  $y$ ) stations (labelled M1 to M5). The most upstream muon station, M1, is located in front of the SPD detector, the remaining four detectors are positioned downstream of the calorimeters.



Between these last four stations, 80 cm thick iron plates act as a muon filter. Multi-wire proportional chambers (MWPC) are used for all regions except the inner region of station M1 where the expected particle rate exceeds safety limits for ageing. In this region triple-gas electron multiplier (triple-GEM) detectors are used. The fast drift gas inside the MWPCs, Ar/CO<sub>2</sub>/CF<sub>4</sub> with 40% Ar and variable concentrations of CO<sub>2</sub>/CF<sub>4</sub>, is used to satisfy trigger requirements.

In the fast and standalone track reconstruction, particles are selected which traverse through all five muon stations. The trigger algorithm starts with hits in the middle station and searches for additional hits in the other stations in order to define a muon track. The slope of the track between M1 and M2 is used to estimate the the particle momentum assuming that it originated from the interaction point and combined with the knowledge of the integrated magnetic field  $\int B \cdot dl$ .

### 2.4.3 RICH detectors

The purpose of the Ring Imaging Cherenkov (RICH) detectors is to differentiate species of charged particles. When charged particles traverse any transparent medium faster than the local speed of light in that medium, photons are emitted coherently. These Cherenkov<sup>1</sup> photons travel away from the charged particle at a specific angle with respect to the trajectory of the particle depending on its velocity,  $\beta$ , and the refractive index,  $n$ , of the medium. This relation is given in Equation 2.4.

$$\cos(\theta_c) = \frac{1}{n\beta} \quad \text{with } \beta = \frac{v}{c} = \frac{p}{E} = \frac{1}{\sqrt{1 + (m/p)^2}} \quad (2.4)$$

When the momentum of a particle is known and its velocity is measured based on the Cherenkov angle, the particle can be identified by the calculation of its mass.

As momentum values increase and the value of  $\cos(\theta_c)$  tends to zero, it becomes difficult to distinguish between different particles. The rate at which this happens depends on the refractive indices of the chosen medium. To be able to identify particles over the full momentum range, LHCb employs two RICH detectors; one upstream of the magnet and the second following the IT and OT tracking stations.

The first RICH detector (RICH1) is designed to separate pions from kaons with momentum in the range of 1-60 GeV. The RICH1 covers the full acceptance of LHCb and consists of two radiator materials with different low refractive indices: a 5 cm layer of aerogel (SiO<sub>2</sub>) and 85 cm of C<sub>4</sub>F<sub>10</sub> gas. The first enables kaon identification above 2 GeV and pion-kaon separation up to 10 GeV. The second enables pion-kaon separation up to 50 GeV.

Higher momentum particles will continue to traverse the second RICH detector (RICH2), which covers an angular acceptance of 15-120 mrad in  $x$ - and 15-100 mrad in  $y$ -direction. It

---

<sup>1</sup>named after the physicist Pavel Alekseyevich Cherenkov.

provides pion-kaon separation from 15-100 GeV. The RICH2 operates with  $CF_4$  gas as single radiator material.

Both detectors use plane mirrors in addition to the principle curved mirrors, to reflect the Cherenkov light onto the Hybrid Photon Detectors (HPDs) that are placed outside the acceptance, where they are protected from the magnetic field by shielding structures.

The result of the pion-kaon separation, based on summer 2011 data which is consistent with the data used for the study in this thesis, is depicted in Figure 2.15. The separation efficiency is shown as a function of particle momentum. It is shown that if a high kaon likelihood is selected, all pions are suppressed, but the efficiency of the kaon selection is reduced at higher momentum values. If a lower likelihood is required, all kaons are selected, but the suppression of pion selection is reduced at higher momentum values.

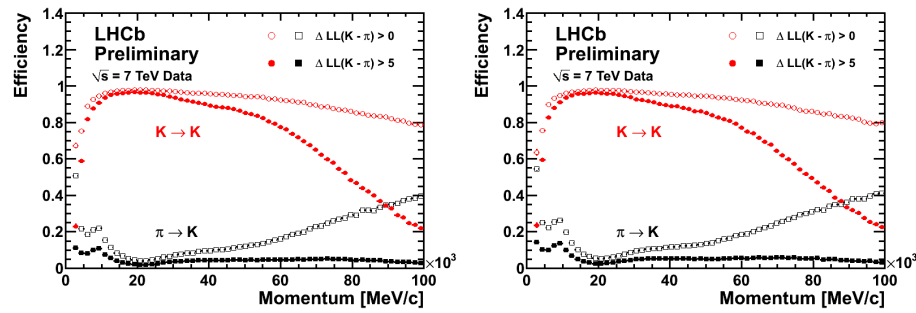


Figure 2.15: The efficiency of pion-kaon separation as a function of particle momentum based on summer 2011 data. The results are obtained with the magnetic downward polarity (left) and the upward polarity (right).

## 2.5 Vertex Locator

The Vertex Locator (VELO) is the detector of LHCb which is closest to the interaction region and it is separated from the beam vacuum by only a thin foil of aluminium. The VELO is contained within a vacuum vessel of 1.7 m length and 1.1 m diameter, which is part of the LHC beam pipe and is sealed by a 2 mm thick aluminium exit window. The VELO strip detectors are distributed over two secondary vacuum boxes which are separated from the LHC beam vacuum.

The VELO contains 21 detector stations, which are distributed over a length of about 1 meter and positioned perpendicular to the beam line. The LHCb interaction region is enclosed by the VELO stations, which also cover the backward region to provide the optimal vertexing of the interaction point. Tracks are reconstructed when a particle has traversed a minimum of three stations. The VELO acceptance thus exceeds the angular acceptance of the LHCb spectrometer.

## Chapter 2. The LHCb experiment

---

Because the VELO is used to reconstruct particle trajectories near the vertex, the innermost radius of these stations should be as small as possible, since a short track extrapolation distance leads to a more precise impact parameter reconstruction. The innermost radius of a VELO strip detector is 8.2 mm; the outer radius 42.0 mm.

Since this distance to the beam is smaller than the 30 mm aperture required by LHC during injection, each station is divided in two halves, a left and a right half module, each spanning 182 degrees to allow for a small overlap to obtain full azimuthal coverage and to accommodate for the relative alignment. The stations reside on a common support system that can be retracted during injection to a save position clear from LHC's required aperture. This retracted position is called the open VELO mode. When the beams have stabilised the VELO returns to its closed mode. To enable full closure, the VELO halves are staggered. Deep inner corrugations in the foil close to the beam axis reduce the material, traversed by particles before the first measured point, to a minimum. The corrugations also allow for the overlap of the left side and right side detector box.

A module consists of two 300  $\mu\text{m}$  thick silicon sensors, a  $\Phi$  sensor and an  $R$  sensor. The two sensors of a module are each mounted on a hybrid. The hybrids are glued back to back on a carbon fibre paddle and base, leaving a distance of 2 mm between the sensors. Each hybrid is cooled to a temperature below zero degrees Celsius by direct thermal contact of cooling pads mounted on the base.

Both the  $R$  and the  $\Phi$  sensor contain 2048 readout strips. The  $R$  sensor contains curved concentric strips and determines the  $r$  radius of a transversing particle. The  $R$  sensor is divided into 4 azimuthal sectors of approximately 45 degrees each and thus they contain 512 strips each. Based on  $R$  measurements alone tracks can be tested if they come from a common vertex or from a secondary decay. Segmenting the  $R$  sensors into 4 sectors increases the track finding efficiency. The distance between the centre of strips, the pitch, varies linearly with  $R$  from 40  $\mu\text{m}$  to 101  $\mu\text{m}$ , with the smallest pitch closest to the beam axis.

The  $\Phi$  sensor contains straight radial strips and, together with the  $R$  coordinate, determines the  $\phi$  angle. This sensor is divided into 2 radial sectors, an inner and an outer sector. The  $\Phi$  strips are tilted with a stereo angle, which is different in sign and magnitude for the inner (20 degrees) and outer (-10 degrees) sector. If extending the strips, their distance of closest approach to the beam axis would be 2.8 mm for the inner sector and 3.1 mm for the outer sector. Its inner sector contains 683 strips and runs from  $r = 8.2$  to  $r = 17.2$  mm, with a pitch width varying from 35.5 to 78.3  $\mu\text{m}$ . The outer sectors thus contains 1365 strips running from  $r = 17.3$  to  $r = 42.0$  mm, with its pitch varying from 39.3 to 96.6  $\mu\text{m}$ . The geometry of the  $r$  and  $\phi$  sensors is depicted in Figure 2.16.

From data collected in 2011, the signal over noise ratio (S/N) is measured to be 19 or 22, for  $r$  and  $\phi$  sensors respectively. The primary vertex resolution in  $x$  and  $y$  is measured to range from 0.010 to 0.037 mm, depending on the number of tracks used in the reconstruction. In  $z$  direction the resolution ranges from 0.05 to 0.25 mm. The impact parameter (IP) resolution

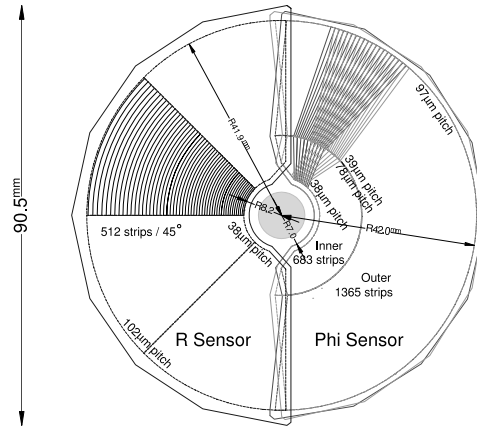


Figure 2.16: Sketch illustrating the  $r\phi$  geometry of the VELO sensors. For clarity, only a portion of the strips are illustrated [17].

results are depicted in Figure 2.17. It shows the IP resolution has a linear dependency to the inverse transverse momentum.

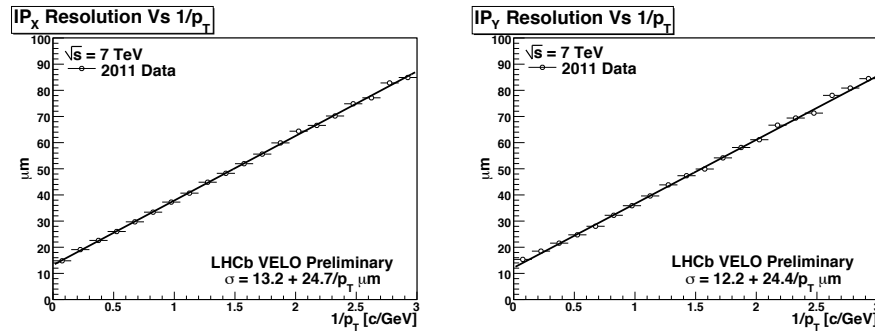


Figure 2.17: The impact parameter (IP) resolution measured in  $x$  (left) and  $y$  (right) as a function of inverse transverse momentum, based on 2011 data.

## 2.6 The Trigger

The LHCb Trigger system consists of three stages: the Level-0 (L0) trigger and the High Level Triggers 1 and 2 (HLT1 and HLT2). The L0 trigger is the hardware trigger, which decision is based on information received from the calorimeter, the muon system and pile-up system, which consists of two dedicated silicon layers and is located upstream of the VELO subdetector. The calorimeter registers the cluster with the highest transverse energy and a particle hypothesis of either photon, electron or hadron is assigned to it. The muon system selects the two muons with the highest transverse momentum. The pile-up system registers how many

interactions take place each bunch crossing and vetoes those events with too many collisions. The measured transverse energy and momenta need to exceed a certain threshold in order for the event to be triggered. After the L0 trigger the event rate is reduced from 40 MHz to approximately 1 MHz, which is the maximum rate at which the detector can be read out. The thresholds are chosen to meet this requirement.

After the event has been selected by the L0 trigger, the higher level trigger algorithms are performed on a computing farm. The HLT1 is designed to confirm or reject the L0 trigger decision. Its decision is based on a partial event reconstruction which includes the tracks or clusters that triggered the L0 decision. This process is split up into alleys, where each alley addresses one of the trigger types of the L0 trigger.

The combined output rate of the events accepted by the HLT1 alleys is sufficiently low to allow an offline track reconstruction. The information obtained through this full track reconstruction is used for the HLT2 decision. Prior to the final selection, composite particles are created from the reconstructed tracks based on loose cuts on momentum and impact parameter. These particles are used to support the HLT2 decision. This decision either selects exclusive decay modes of interest or inclusive decays based on special event topologies.

The  $B^0 \rightarrow D^{*-} \tau^+ \nu_\tau$  decay, as studied in this thesis, is a multi-body decay and suffers from low transverse momentum per particle, which results in a low L0 efficiency. However,  $\bar{D}^0 \rightarrow K^+ \pi^-$  and  $\tau^+ \rightarrow \pi^+ \pi^+ \pi^- \bar{\nu}_\tau$  result in 2-prong and 3-prong vertices, which can be sufficiently displaced to pass the topological trigger.

## 2.7 LHCb Software

The experiment-wide software (C++) framework known as Gaudi [24] is used for the generation and processing of data. It ensures availability of all LHCb tools and algorithms across the experiment and enforces global consistency of LHCb analyses. Its main components can be separated in terms of

- *Generation:* The LHCb software package Gauss is responsible for the generation of Monte Carlo (MC) simulation data. In this step, the primary  $pp$  beams collisions are simulated using PYTHIA [25] and the B particles that are produced decay according to the EvtGen [26] decay model.
- *Digitisation:* The response of the LHCb detector to the generated particles is handled by the Boole application. A model of the LHCb detector based on GEANT4 [27] is used to simulate the digital output. The digitised data is the MC equivalent of real measured data. From this point, both pass through the same reconstruction chain.
- *Reconstruction:* The Brunel application handles the reconstruction of the digitised output of the detector responses. Signal hits in the detector are clustered and associating tracks are constructed. Particle properties such as momentum are determined and PID

measurements are performed. The output of Brunel is a full reconstructed dataset known as a 'Data Storage Tape' (DST) file.

- *Analysis:* Offline analyses are performed using the DaVinci package. The DaVinci application allows for reconstructed particles to be combined and determines primary and secondary vertices as well as kinematic quantities, such as invariant masses of decayed particles and their distance of flight.

Individual algorithms store their produced data in a Transient Event Store (TES), which is consecutively used as an input location for the following process. A global conditions database [28] contains all parameters required for the current running conditions of the experiment.

The MC samples used in this thesis are labelled MC10 and are generated using parameters compatible with the LHCb 2011 data sample.



### 3 Studies of $\tau$ reconstruction using simulated events

The goal of this chapter is to demonstrate the principle of event reconstruction methods for various interesting processes in which one or two  $\tau$  leptons are involved. Since the purpose is to demonstrate the methods, simulated data signal samples are used. In order to understand the signal properties, only tracks coming from the process of interest are considered. However, to understand the effect of the detector resolution, both generated quantities and reconstructed quantities are used in the study.

The momentum of the  $\tau$  particle is notoriously difficult to reconstruct. All its major decay channels contain a  $\tau$  neutrino,  $\nu_\tau$ . The neutrino traverses LHCb undetectably and therefore causes missing energy in the decay. As LHCb doesn't have a full solid angle coverage, only a subset of particles from each collision traverses the detector. A vast amount of energy is lost in all events. It is therefore impossible to determine the amount of energy that is lost due to an undetectable neutrino. The  $\tau$  mass can thus not be calculated by combining its daughter particles' measured momenta.

An exception is the neutrinoless flavour violating decay of  $\tau^- \rightarrow \mu^+ \mu^- \mu^-$ . This rare  $\tau$  decay is fully reconstructable, but its branching fraction is yet to be measured. Section 3.1 shortly discusses the measurement possibilities for this decay at LHCb. A difficulty in the determination of the  $\tau^- \rightarrow \mu^+ \mu^- \mu^-$  branching fraction is choosing a  $\tau$  normalisation channel.

The decay mode of  $\tau^- \rightarrow \pi^+ \pi^- \pi^- \nu_\tau$  has been considered as a possible normalisation channel. It is found that when the origin and decay vertex of the  $\tau$  particle are reconstructable and the missing mass is limited to a single neutrino, the  $\tau$  momentum can be calculated up to a twofold ambiguity, which is shown in Section 3.2. This requires that the  $\tau$  lepton decays into a three-prong of charged particles to enable the reconstruction of the decay vertex. The branching fraction of such events, with no additional neutral particles, is approximately 9.8% [5]. Although other decay reconstruction possibilities have arisen from the possible reconstruction of  $\tau^- \rightarrow \pi^+ \pi^- \pi^- \nu_\tau$ , the channel is insufficient as a  $\tau^- \rightarrow \mu^+ \mu^- \mu^-$  normalisation channel due to overwhelming physics background.



### Chapter 3. Studies of $\tau$ reconstruction using simulated events

---

The decay channel of  $B^0 \rightarrow D^{*-} \tau^+ \nu_\tau$  contains two  $\tau$  neutrinos when required that the  $\tau$  lepton decays as  $\tau^+ \rightarrow \pi^+ \pi^+ \pi^- \bar{\nu}_\tau$ . Both neutrinos originate from particles (the  $\tau$  lepton and  $B^0$  meson) of which the production vertex and decay vertex are measurable. At the generation level, its reconstruction is thus equivalent to that of a single  $\tau^- \rightarrow \pi^+ \pi^- \pi^- \nu_\tau$  decay. However, the additional information available can be used to constrain its reconstruction. Chapter 4 is dedicated to the analysis of the  $B^0 \rightarrow D^{*-} \tau^+ \nu_\tau$  decay channel, in which also its application to real data is discussed.

The decay into a single  $\tau$  particle can be extended to a  $\tau$  pair originating from a known common vertex. Its reconstruction is discussed in Section 3.3, which focuses on the  $Z^0 \rightarrow \tau^+ \tau^-$  decay mode.

When additional information is available, the production vertex of the  $\tau$  lepton does not always need to be known for its full reconstruction. A more complicated problem is that of a  $\tau$  pair coming from an unknown displaced vertex, which occurs in the decay channel  $B_s^0 \rightarrow \tau^+ \tau^-$ . Section 3.4 deals with this more elaborate mathematical reconstruction.

Section 3.5 shortly discusses other interesting reconstruction possibilities. In the lepton flavour violating (LFV) decay of  $B_s^0 \rightarrow \tau^+ \mu^-$  one of the  $\tau$  particles is replaced by a  $\mu$  lepton, constraining the allowed location of the  $\tau$  production vertex. Instead of replacing one of the  $\tau$  particles, it is also possible to add an additional track in order to constrain the vertex location, which is the case for the rare  $B^+ \rightarrow K^+ \tau^+ \tau^-$  decay. This is the first decay that is fully constrained without fixing the mass of the B particle. The last considered reconstruction is that of the rare  $B^0 \rightarrow K^* \tau^+ \tau^-$  decay mode. Here, the fully reconstructable  $K^*$  particle fixes the  $\tau$  production vertex completely.

Theoretically, all these decays can be reconstructed analytically. However, due to measurement errors in particle momenta, production and decay vertices, an analytical solution is not always possible. The reconstruction possibilities can be improved using computational methods. Even when an analytical solution exists, the accuracy may be increased by a constrained event fit.

#### 3.1 The lepton flavour violating decay $\tau^- \rightarrow \mu^+ \mu^- \mu^-$

In the Standard Model, lepton flavour conservation is explicitly assumed. However with the discovery of neutrino oscillations, charged lepton decays can now violate the lepton flavour conservation. The  $\tau^- \rightarrow \mu^+ \mu^- \mu^-$  branching fraction through neutrino oscillation is proportional to the term  $(m_\nu/m_W)^4 \sim 10^{-50}$ , where  $m_\nu$  and  $m_W$  are the neutrino and  $W$  mass respectively. This rate is immeasurably small by many orders of magnitude compared to what could be measured by any experiment. However, New Physics models, like mediating boson models or supersymmetry (SUSY) models, predict much higher branching fractions. The non-universal  $Z'$  model predicts a branching fraction of the order  $10^{-8}$  [29], whereas the minimal supersymmetric model predicts it to be  $10^{-9}$  [30].

### 3.1. The lepton flavour violating decay $\tau^- \rightarrow \mu^+ \mu^- \mu^-$

The lepton flavour violating decay  $\tau^- \rightarrow \mu^+ \mu^- \mu^-$  is an ideal decay mode for LHCb to probe. The muons are easily identified and triggered upon by their penetration through iron shielding. The decay can be reconstructed with high efficiency and precision, using the vertex detector which is specifically designed to identify secondary vertices. This results in a precise determination of the  $\tau$  vertex location and an excellent  $\tau$  mass resolution, since there is no missing neutrino. As most  $\tau$  leptons come from b and c hadrons, its vertex will be sufficiently displaced to pass the impact parameter requirements, designed to select B mesons in the LHCb trigger.

Upper limits on the branching fraction have been set by BaBar and Belle. BaBar has obtained a limit of  $3.3 \cdot 10^{-8}$  [31], but the strongest limit of  $2.1 \cdot 10^{-8}$  [32] is currently set by Belle at a 90% confidence limit. These limits are in the range of many New Physics predictions and any improvement will have a direct effect on the understanding of New Physics.

#### 3.1.1 Estimation of measurement limit at LHCb

Based on PYTHIA estimations [25], the total  $\tau$  cross section at LHCb is calculated to be  $\sim 111 \mu\text{b}$  at  $\sqrt{s} = 14 \text{ TeV}$ . A nominal year ( $10^7$  seconds) of data taking yields  $2 \text{ fb}^{-1}$  of data and  $2.22 \cdot 10^{11}$   $\tau$  particles will be produced. The geometrical efficiency of the  $\tau$  leptons decaying to three muons, i.e. all three daughters are in the acceptance of LHCb ( $10 \text{ mrad} < \theta < 400 \text{ mrad}$ ), is estimated from simulation to be  $\sim 19.5\%$ . The branching fraction of this decay is currently known to be smaller than  $2.1 \cdot 10^{-8}$  (Belle's limit). There are therefore less than 910 signal events in LHCb per nominal year. The reconstruction efficiency, with minimal pre-selection, is  $\sim 25\%$ , resulting in less than 228 signal events before applying any selection criteria.

Around half -52%- of the signal  $\tau$  particles come from prompt  $D_s$  mesons, 34% come directly from B mesons and the remaining 14% come from  $D_s$  mesons through B meson decays. Prompt  $\tau$  particles are estimated to contribute  $< 1\%$  to the total source of  $\tau$  particles, but is to a large extent uncertain. The main source of background originates from  $\mu$  lepton pairs produced in b and  $\bar{b}$  quark decays combined with one random track.

An initial study, based on Monte Carlo signal and di- $\mu$  background events, estimates the signal selection efficiency to be  $\sim 5\%$  [33]. Based on this selection and including all  $\tau$  sources, an upper limit on the branching fraction of  $3.2 \cdot 10^{-8}$  could be set with a 90% confidence level within one nominal year of data taking at  $\sqrt{s} = 14 \text{ TeV}$ . This number matches BaBar's current limit, but would not be an improvement on Belle's limit. Within the lifetime of LHCb, which corresponds to  $10 \text{ fb}^{-1}$ , the limit on the branching fraction would improve to  $1.3 \cdot 10^{-8}$ .

#### 3.1.2 Normalisation difficulties

After a certain number of signal candidates are selected, it is necessary to know how many candidates there were to start with in order to determine a branching fraction. To overcome this problem, the signal candidates can be normalised using the number of candidates selected from a different decay of which the branching fraction is already well-measured. A difficulty

### Chapter 3. Studies of $\tau$ reconstruction using simulated events

with any  $\tau$  normalisation channel which conserves lepton flavour, is that it suffers from missing energy.

The decay channel of  $\tau^- \rightarrow \pi^+ \pi^- \pi^- \nu_\tau$  has been considered as a possible normalisation channel. This decay is unique in the sense that it is fully reconstructable. However, because the prompt  $\tau$  cross section is significantly small compared to the inclusive b and c cross sections, this decay channel is dominated by physics background.

The background mode  $D^- \rightarrow \pi^+ \pi^- \pi^- \pi^0$  has a similar signature as the considered  $\tau^- \rightarrow \pi^+ \pi^- \pi^- \nu_\tau$  channel. Although the  $D^\pm$  meson is heavier than the  $\tau$  lepton, reconstructable mass is lost through the  $\pi^0$ , resulting in a mass similar to that of the  $\tau$  lepton. Based on the cross section and branching fraction, the occurrence of prompt  $D^- \rightarrow \pi^+ \pi^- \pi^- \pi^0$  events can be estimated to be a factor 4,500 larger than prompt  $\tau^- \rightarrow \pi^+ \pi^- \pi^- \nu_\tau$  events. This abundant physics background is irreducible due to the similar signatures of the two decays. In Figure 3.1 the distributions<sup>1</sup> of the invariant  $3\pi$  mass is depicted for both decays.

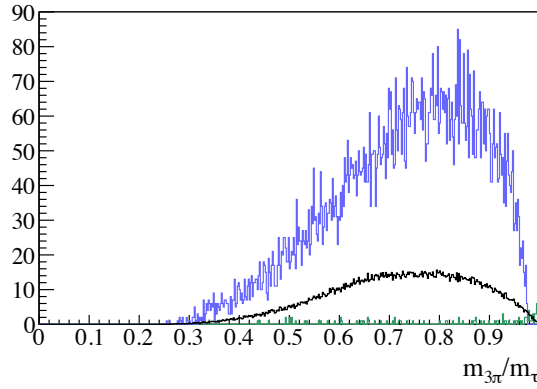


Figure 3.1: The  $3\pi$  invariant mass distributions of  $D^- \rightarrow \pi^+ \pi^- \pi^- \pi^0$  in blue, radiative  $D^- \rightarrow \pi^+ \pi^- \pi^- \gamma$  with missing photons in green and signal  $\tau^- \rightarrow \pi^+ \pi^- \pi^- \nu_\tau$  -scaled by a factor of 1,000- in black. The  $3\pi$  invariant mass is normalised to the  $\tau$  lepton mass.

To overcome normalisation difficulties, a current study considers only  $\tau$  leptons from  $D_s$  mesons, which is its main source. An attempt is being made to normalise these  $\tau$  leptons to the  $D_s$  decay channels  $D_s^- \rightarrow \phi(\mu^+ \mu^-) \pi^-$  and  $D_s^- \rightarrow \pi^+ \pi^- \pi^-$  [34].

Although using the decay channel  $\tau^- \rightarrow \pi^+ \pi^- \pi^- \nu_\tau$  as a  $\tau^- \rightarrow \mu^+ \mu^- \mu^-$  normalisation channel has been shown to be impossible, it has led to interesting new research. In the Sections 3.2-3.5.3 the reconstruction possibilities of this decay mode and its possible applications and physics interests are discussed.

<sup>1</sup>Whenever the focus is on the distribution shape or on the relative number of events between distributions, but not on the absolute number of events, the label "Events/bin size" is omitted.

### 3.2 Reconstruction of $\tau^- \rightarrow \pi^+ \pi^- \pi^- \nu_\tau$ from a known vertex

Interesting decays containing a  $\tau$  lepton from a known vertex are  $Z^0 \rightarrow \tau^+ \tau^-$ ,  $B^0 \rightarrow K^* \tau^+ \tau^-$  and  $B^0 \rightarrow D^{*-} \tau^+ \nu_\tau$ . The concept of single  $\tau$  lepton reconstruction does not distinguish between these decays when generated quantities are used. With reconstructed quantities however, the results depend on the accuracy of the reconstructed values and on additional event information.

Note that it is possible to select only those three-prongs which mass is close to the  $\tau$  lepton mass. The existence of the neutrino can then be neglected based on the assumption that all energy has been transferred to the hadrons. Using this method, only a small fraction of  $\tau$  decays is selected. In addition, the calculated  $\tau$  momentum is an approximation; its accuracy depends on the missing energy.

In this section full and exclusive  $\tau$  reconstruction is discussed. A majority of  $\tau$  decays can be accurately reconstructed and used in different physics analyses. A schematic representation of the  $\tau$  lepton decay is depicted in Figure 3.2.

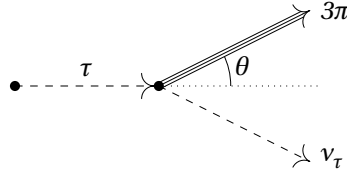


Figure 3.2: A schematic representation of  $\tau^- \rightarrow \pi^+ \pi^- \pi^- \nu_\tau$ .

#### 3.2.1 Analytic reconstruction

Two precepts are applied for the full  $\tau$  reconstruction: the  $\tau$  mass is fixed at its rest value,  $m_\tau = 1777$  MeV and the neutrino is massless,  $m_\nu = 0$ . The fixed value of the neutrino mass is necessary as the  $\nu_\tau$  4-momentum is unknown. The  $\tau$  decay daughters can therefore not contain more than one neutral particle, as their combined mass will be unknown. If no other information is available, the  $\tau$  production vertex needs to be known to allow the determination of the  $\tau$  4-momentum,  $p_\tau$ .

The combined  $3\pi$  4-momentum and the production and decay vertices of the  $\tau$  lepton are the known parameters in this calculation. The unit vector along the  $\tau$  momentum trajectory, given by the decay vertex minus the production vertex, is referred to by  $\vec{u}$ . The relations which

### Chapter 3. Studies of $\tau$ reconstruction using simulated events

need to be satisfied are:

$$0 = (p_\tau - p_{3\pi})^2 \quad (3.1)$$

$$m_\tau^2 = E_\tau^2 - |\vec{p}_\tau|^2 \quad (3.2)$$

$$\vec{p}_\tau = |\vec{p}_\tau| \cdot \vec{u} \quad (3.3)$$

Equations 3.1 and 3.2 ensure the correct  $\nu_\tau$  and  $\tau$  masses, respectively, whereas Equation 3.3 ensures the correct direction of the  $\tau$  3-momentum.

As Equation 3.3 introduces two unique relations, there are four unknowns and four relations. However, due to the quadratic nature of the mass constraints, there are two physically valid  $\tau$  momentum solutions, given by measured quantities only as

$$|\vec{p}_\tau| = \frac{(m_{3\pi}^2 + m_\tau^2) |\vec{p}_{3\pi}| \cos(\theta) \pm E_{3\pi} \sqrt{(m_\tau^2 - m_{3\pi}^2)^2 - 4m_\tau^2 |\vec{p}_{3\pi}|^2 \sin^2(\theta)}}{2(E_{3\pi}^2 - |\vec{p}_{3\pi}|^2 \cos^2(\theta))} \quad (3.4)$$

Here  $\theta$  is the angle between the  $\tau$  and  $3\pi$  momentum vectors. Having obtained the  $\tau$  momentum, all  $\tau$  4-momentum components are now derived using Equations 3.2 and 3.3. Figure 3.3 illustrates the distribution of the two allowed  $\tau$  momenta per measured angle for one event. The discrepancy between the two  $\tau$  momentum solutions is largest when the momentum of the three-prong and the  $\tau$  momentum are co-linear. At the maximal allowed angle there is a unique solution for the  $\tau$  momentum.

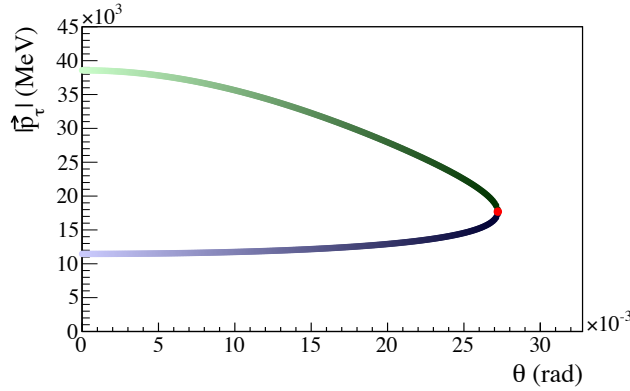


Figure 3.3: The two possible  $\tau$  momentum solutions as a function of the angle  $\theta$  for one event. The solutions with a positive discriminant are depicted in green, those with a negative one in blue. The red dot represents the unique solution where the discriminant is 0.

The two solutions for the neutrino momentum have equal transverse component with respect to the  $\tau$  lepton direction. In the  $\tau$  rest frame, the two neutrino solutions occur in opposite direction ( $180^\circ$  difference). Figure 3.4 illustrates the relation between the  $3\pi$  and  $\nu_\tau$  momentum solutions for a given  $\tau$  value in the lab frame. Each colour represents a possible solution. In

### 3.2. Reconstruction of $\tau^- \rightarrow \pi^+ \pi^- \pi^- \nu_\tau$ from a known vertex

green are those solutions where a higher energy is assigned to the three-prong. Each of these solutions has a counterpart solution in blue, where the transverse momentum of the particles is the same, but where less energy has been transferred to the three-prong. The solution depicted with red arrows, corresponds to the unique solution where the angle between the three-prong and the  $\tau$  lepton is maximal.

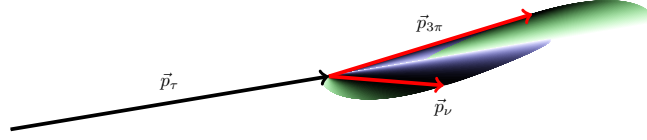


Figure 3.4: A schematic representation of the possible combinations of  $\tau$  and neutrino momenta. The red arrows represent the solution where the discriminant is equal to 0.

Although each  $\tau^- \rightarrow \pi^+ \pi^- \pi^- \nu_\tau$  decay has two physically valid solutions for the  $\tau$  momentum, there is naturally only one correct solution which matches with the true  $\tau$  momentum. Due to the rounding errors in the calculation, even when the generated quantities are used for the  $3\pi$  momentum and the production and decay vertices of the  $\tau$  lepton, the correct solution for the  $\tau$  momentum calculated using Equation 3.4 is not exactly the same as the generated value. To demonstrate this, Figure 3.5 shows the  $|\vec{p}_\tau|$  asymmetry defined as

$$\sigma(|\vec{p}_\tau|) = \frac{|\vec{p}_\tau| - |\vec{p}_\tau|_{MC}}{|\vec{p}_\tau| + |\vec{p}_\tau|_{MC}} \quad (3.5)$$

A FWHM of the asymmetry distribution of  $0.3 \cdot 10^{-3}$  corresponds to an error of  $(1 - 0.3 \cdot 10^{-3}) / (1 + 0.3 \cdot 10^{-3}) \sim 0.06\%$ .

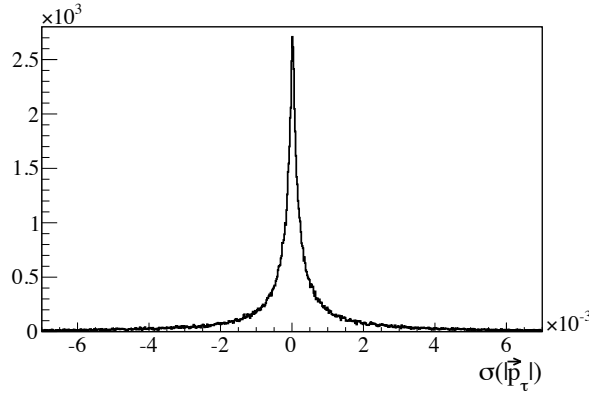


Figure 3.5: The asymmetry distribution between the generated momenta and the calculated momenta which match the MC information.

The size of the  $\tau$  momentum asymmetry between the correctly and incorrectly assigned

momentum solutions is related to the invariant  $3\pi$  mass; the less energy is given to the neutrino, the closer the two  $\tau$  momentum solutions. The  $3\pi$  invariant mass distribution and the asymmetry as a function of the invariant mass are shown in Figure 3.6. A  $3\pi$  invariant mass cut at  $m_{3\pi}/m_\tau > 0.9$  means that the absolute asymmetry is always smaller than 0.1, and thus that the correct  $\tau$  momentum is calculated with an error smaller than 20%. This mass cut keeps  $\sim 10\%$  of the decays.

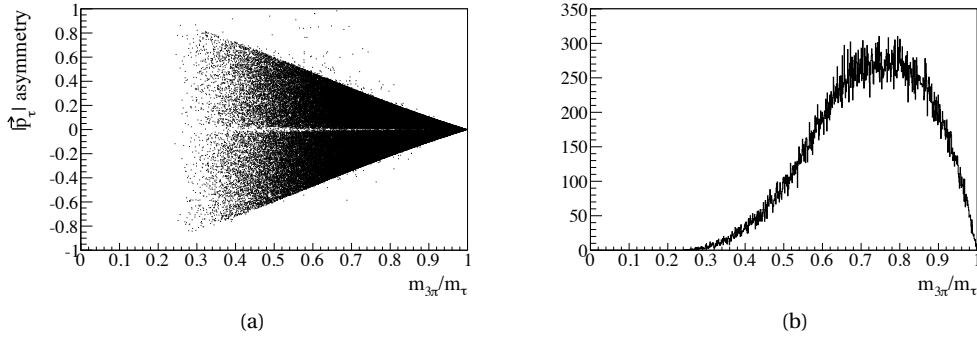


Figure 3.6: (a) The relation between  $\tau$  momentum asymmetry and the  $3\pi$  invariant mass and (b) the  $3\pi$  invariant mass distribution. Both invariant mass distributions are normalised to the  $\tau$  lepton mass.

### 3.2.2 Analytic limitations

As Equation 3.4 shows, a solution for the  $\tau$  momentum is only found when the angle  $\theta$  is equal to or smaller than a maximum allowed value based on the  $3\pi$  4-momentum, given by

$$\theta_{\max} = \text{asin}\left(\frac{m_\tau^2 - m_{3\pi}^2}{2m_\tau |\vec{p}_{3\pi}|}\right) \quad (3.6)$$

When  $\theta$  is measured to be larger than  $\theta_{\max}$  due to rounding or measurement error, it is impossible to calculate an analytic solution. Figure 3.7 shows the generated  $\tau$  momenta between  $|\vec{p}_\tau|_{\min}$  and  $|\vec{p}_\tau|_{\max}$  versus the calculated  $\theta$  with relation to  $\theta_{\max}$  (log scale) using generated values (orange) and using reconstructed values for prompt  $\tau$  leptons (grey). It demonstrates the calculation's sensitivity to errors as small as rounding and need of error exploitation. At generator level a solution is found for  $\sim 95.5\%$  of the  $\tau$  decays. For reconstructed data this efficiency falls to  $\sim 29\%$  based on prompt  $\tau$  leptons.

### 3.2.3 Constrained fit

The constrained fit exploits the errors on the measured quantities to find a best estimation of the  $\tau$  momentum when an exact calculation is not possible. Its aim is to minimise the value of

### 3.2. Reconstruction of $\tau^- \rightarrow \pi^+ \pi^- \pi^- \nu_\tau$ from a known vertex

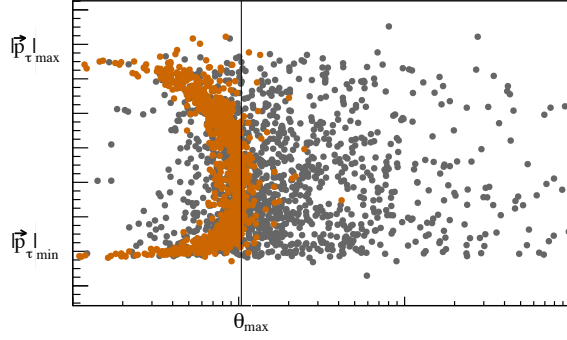


Figure 3.7: The generated  $\tau$  momentum versus the angle  $\theta$  as a function of  $\theta_{\max}$  for generated data (orange) and for reconstructed data (grey).

the  $\chi^2$ , defined as

$$\chi^2 = (m - h(x))^T W (m - h(x)) \quad (3.7)$$

The measured values are denoted by  $m$ . The description of the system,  $h(x)$ , contains the calculated values of the measured quantities based on parameters  $x$ .  $W$  is the weight matrix; the inverse of the covariance matrix of the measured quantities.

The function and its parameters need to be chosen to ensure convergence to a minimum  $\chi^2$  value. The standard measured quantities are the production vertex,  $\mathbf{pV}$ , the decay vertex,  $\mathbf{dV}$ , and the  $3\pi$  4-momentum,  $(E_{3\pi}, \vec{p}_{3\pi})$ . A small variation of the  $3\pi$  energy and its momentum can lead to a negative  $3\pi$  invariant mass. It is therefore more stable to use the  $3\pi$  invariant mass in the description of the system rather than its energy and a convenient choice of variable is  $m_{3\pi}^2$ . The Jacobian matrix is applied to the covariance matrix in order to make it compatible with the change of variable. The chosen description consists of the following 10 quantities:

$$h(x) = \{ \mathbf{pV}, \mathbf{dV}, \vec{p}_{3\pi}, m_{3\pi}^2 \} \quad (3.8)$$

The parameters which are used to describe the system are the production vertex, the  $\tau$  momentum, the  $\nu_\tau$  momentum and the scaling factor  $L_\tau$ , defined by  $|\mathbf{dV} - \mathbf{pV}| = L_\tau |\vec{p}_\tau|$ :

$$x = \{ \mathbf{pV}, \vec{p}_\tau, \vec{p}_\nu, L_\tau \} \quad (3.9)$$

The  $\tau$  and neutrino mass are inserted directly into the description of the system, by expressing the  $3\pi$  mass as

$$m_{3\pi}^2 = m_\tau^2 - 2E_\nu E_\tau + 2\vec{p}_\nu \cdot \vec{p}_\tau \quad (3.10)$$



with

$$E_\nu = |\vec{p}_\nu| \text{ and } E_\tau = \sqrt{m_\tau^2 + |\vec{p}_\tau|^2} \quad (3.11)$$

Minimising the  $\chi^2$  is equivalent to finding the root of its derivative. Root finding can be performed by the Newton-Raphson method. Initial values of the parameters,  $x_0$ , have to be provided.

It is essential that the initial guess is made close to the true values of the parameters to avoid local minima. At  $\theta = 0$  the region of allowed  $\tau$  momenta can be determined approximately; an initial guess in this region is as good as can be approximated.

The Newton-Raphson method is an iterative algorithm which reduces the parameters  $x$  by an amount  $\Delta x$  until a root has been found.  $\Delta x$  is defined as

$$\Delta x = \left( \frac{\partial^2 \chi^2}{\partial x^2} \right)^{-1} \left( \frac{\partial \chi^2}{\partial x} \right) = (H^T W H)^{-1} H^T W (m - h(x)) \quad (3.12)$$

Here  $H$  is the derivative matrix of the description of the system to its parameters [35]. To ensure convergence an extra term is added to the correction  $\Delta x$ . This term is based on the method of gradient descent and used in addition to the Newton-Raphson method in the Levenberg-Marquardt algorithm. The correction becomes

$$\Delta x = (H^T W H + \lambda \text{diag}(H^T W H))^{-1} H^T W (m - h(x)) \quad (3.13)$$

The value of  $\lambda$  determines the influence of this extra term. Starting with  $\lambda = 0$ , if the Newton-Raphson method does not converge, the value of  $\lambda$  is increased and the method of gradient descent takes over. Its convergence is slower than that of the Newton-Raphson method, but it is guaranteed (up to a local minimum). There is no predefined value for the increase of  $\lambda$ , but the best value can be determined after a convergence study. In this chapter  $\delta\lambda = 1 \cdot 10^{-6}$  is used. Each time the parameters are recalculated as  $x + \Delta x$  and the  $\chi^2$  is obtained. The algorithm is terminated when a set maximum of iterations has been reached or when the  $\chi^2$  changes less than 0.1% in 5 consecutive iterations.

When the best values of the measurables are found, the second solution can be calculated analytically.

### 3.2.4 Decay time distributions

The decay time distributions of the correct and incorrect  $\tau$  momentum solutions, separated based on known MC truth information, show a small systematic difference, depicted in Figure 3.8. However, based on a single  $\tau$  reconstruction it is not possible to separate the true solutions from the fake solutions.

As the decay time distributions are practically indistinguishable for the correct and incorrect

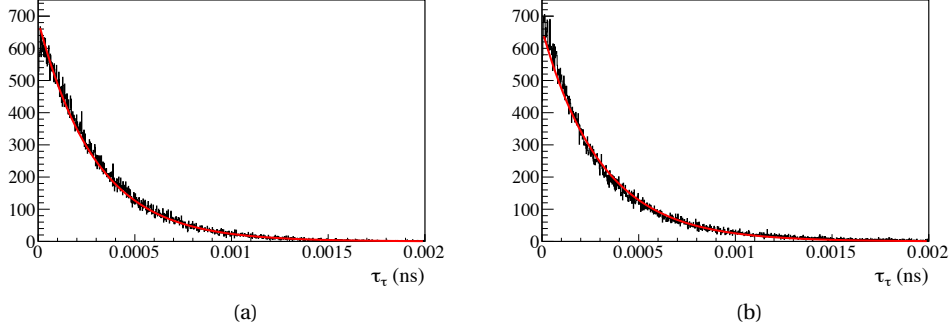


Figure 3.8: (a) The decay time distribution of the set of correct  $\tau$  momentum solutions with  $\tau_\tau = (2.978 \pm 0.009) \cdot 10^{-13}$  s. (b) The decay time distribution of the set of incorrect  $\tau$  momentum solutions which gives  $\tau_\tau = (3.037 \pm 0.011) \cdot 10^{-13}$  s.

momentum solutions based on generated quantities, it is unnecessary to differentiate between them. Decay time measurements can be weighed depending on the number of momentum solutions found in each event in order not to bias the distribution with a selection.

### 3.3 $Z^0 \rightarrow \tau^+ \tau^-$ reconstruction without mass cut

The Drell-Yan process of  $\gamma^*/Z^0 \rightarrow \tau^+ \tau^-$  is the prime example of a  $\tau$  pair produced at a known vertex, i.e. the primary vertex. Even though this reconstruction channel contains two neutrinos, no upper limit cut needs to be made on the mass of the mother particle. This means that the mass window can be widened to allow the search for heavier gauge bosons. A wide range of models predict extra neutral gauge bosons. Current experimental lower limits on the mass of the  $Z'$  boson are derived from searches using high-mass  $\tau$  pairs at the Tevatron experiments and are set to 400 GeV at 95% confidence level [36]. If such a heavier neutral boson exists then its decay through  $\tau$  leptons may be the ideal reconstruction channel, due to the favoured coupling to the  $\tau$  mass for certain New Physics models.

In Section 3.2 it has been shown that the  $\tau$  particle can be fully reconstructed when it originates and decays at a measurable point in space. The limitation is that there are two kinematically valid momentum candidates and without additional information from the event, it is impossible to distinguish between them. To analytically reconstruct the  $Z^0 \rightarrow \tau^+ \tau^-$  decay, the single  $\tau$  reconstruction is performed twice with a common production vertex for the two  $\tau$  leptons. It follows that there are four possible momentum solutions for the  $Z^0$  particle. Due to the width of the  $Z^0$  mass peak, it is unfavourable to fix this mass in order to constrain the event, but better to use the invariant mass distributions of the four combinations. Figure 3.9 depicts the analytically calculated  $\gamma^*/Z^0$  mass distributions using generated quantities for the four combinations of the possible two  $\tau$  momenta.

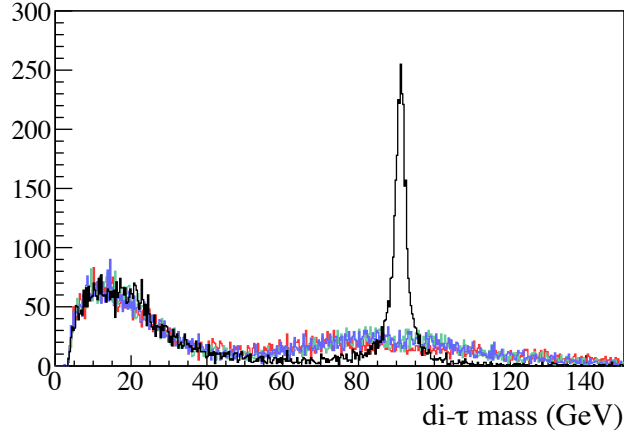


Figure 3.9: The mass distribution of the combined  $\tau$ -pair momentum solutions with: two correct reconstructions (black), one correct reconstruction (blue and green) and two incorrect reconstructions (red) based on the analytical reconstruction of generated quantities.

For reconstructed quantities, the efficiency of calculating the momentum of a  $\tau$  lepton pair analytically is  $\sim 8\%$ , the efficiency of a single  $\tau$  lepton reconstruction squared. It is therefore paramount to improve reconstruction efficiencies by using a computational method to determine the  $\tau$  lepton momenta.

### 3.3.1 Constrained fit

The constrained fit of a  $\tau$  lepton pair from a known vertex is equivalent to the method of reconstructing a single  $\tau$  lepton, as described in 3.2.3. However, the input parameters and the description of the system are adjusted. As the two tau leptons share the same production vertex, the problem expands to a 17 dimensional system: the primary vertex and two times the 7 parameters related to the reconstructed pions. The description of the system is thus given by

$$h(x) = \{\mathbf{pV}, \mathbf{dV}_1, \vec{p}_{13\pi}, m_{13\pi}^2, \mathbf{dV}_2, \vec{p}_{23\pi}, m_{23\pi}^2\} \quad (3.14)$$

and its parameters

$$x = \{\mathbf{pV}, \vec{p}_{1\tau}, \vec{p}_{1\nu}, L_{1\tau}, \vec{p}_{2\tau}, \vec{p}_{2\nu}, L_{2\tau}\} \quad (3.15)$$

### 3.3.2 Reconstruction efficiency and accuracy

To determine the accuracy of the constrained fit, the calculated  $\tau$  momenta are compared to the generated  $\tau$  momenta. For each decay, only the correct  $\tau$  momentum which best matches the MC truth is considered. Figures 3.10(a) and (b) depict the  $\tau$  momentum asymmetry dis-

### 3.3. $Z^0 \rightarrow \tau^+\tau^-$ reconstruction without mass cut

tributions for the analytically obtained momentum solutions and for those solutions where a computational method was necessary, respectively. In this last distribution, the decays for which an analytical momentum solution exist are thus omitted. A tail to the left of the asymmetry distribution is visible, which indicates a systematic underestimation of the  $\tau$  momentum. The FWHM (Full Width Half Maximum) of 0.042 corresponds to an error of  $\sim 8\%$ , whereas an FWHM of 0.036 corresponds to an error of  $\sim 7\%$ . When there is no analytical solution possible due to inaccurate measurement values, an increase in  $\tau$  momentum asymmetry error is expected.

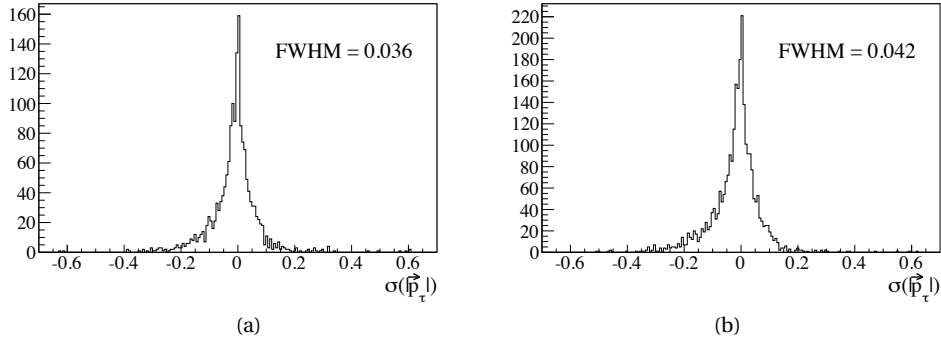


Figure 3.10: The distribution of the  $|\vec{p}_\tau|$  asymmetry between the generated momenta and (a) the analytically reconstructed momenta and (b) the computationally reconstructed momentum solutions (excluding those with an analytical solution).

If the  $\tau$  momentum is not analytically calculable, then the angle between the reconstructed  $\tau$  vertices and the  $3\pi$  momentum vector is too large. To estimate the  $\tau$  momentum, the angle can be set to its maximum allowed value. In order to demonstrate the advantage of a constrained fit of the decay over such an estimation, the momentum asymmetry between the estimated momenta and the generated momenta is shown in Figure 3.11. A large tail of underestimated  $\tau$  momenta is visible in addition to an increased FWHM value of 0.071, which corresponds to an error of  $\sim 13\%$ .

The efficiency of the analytical solution is  $\sim 8\%$ , whereas the efficiency of the constrained fit when cut at  $\chi^2 < 10$  is  $\sim 80\%$ . These efficiencies can improve after selection cuts.

#### 3.3.3 di- $\tau$ invariant mass distribution

The  $\tau$  pair invariant mass, where all the four di- $\tau$  combinations are added, results in a clear signature mass distribution, peaking at the  $Z^0$  mass. Figure 3.12 shows the di- $\tau$  mass distributions of the differently reconstructed momenta. An MC data sample corresponding to  $\sim 200 \text{ pb}^{-1}$  is used to produce the reconstructed di- $\tau$  invariant mass distributions. When the generated values are taken for the  $\tau$  vertices and  $3\pi$  momenta, a clear signal peak is seen at the  $Z^0$  mass. Combining the computationally reconstructed momenta results in a signal peak left of the  $Z^0$

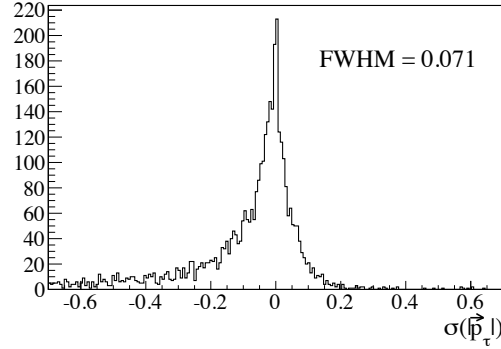


Figure 3.11: The distribution of the  $|\vec{p}_\tau|$  asymmetry between the generated momenta and the estimated momenta, where the angle between the  $\tau$  and  $3\pi$  momenta is maximal.

mass. This is consistent with the tail observed in the  $|\vec{p}_\tau|$  asymmetry distribution. The peak is less defined than the MC signal peak due to measurement error. When only selecting the analytic solutions, there is not enough data available to distinguish a peak. Setting a maximum angle between the  $\tau$  and  $3\pi$  momentum vectors further spreads the signal peak and pulls it to the left of the known  $Z^0$  mass peak.

### 3.3.4 Conclusion

Although it is unfavourable to fix the  $Z^0$  mass to constrain the decay due to its width, the di- $\tau$  invariant mass distribution is shown to peak at the established  $Z^0$  mass value. The open mass window allows for the search of heavier New Physics bosons, which favour a coupling to the heavy  $\tau$  lepton mass. It has been shown that by fitting the decay with constraints and allowing for measurement error, the reconstruction efficiency improves by a factor  $\sim 10$ . Although a  $\tau$  momentum estimation is possible by selecting the maximally allowed angle between the  $\tau$  and  $3\pi$  momenta, its accuracy after a decay fit is improved by approximately 38%.

## 3.4 Ideas on $B_s^0 \rightarrow \tau^+ \tau^-$ reconstruction

A principal goal for LHCb is the measurement of the branching fraction of the decay  $B_s^0 \rightarrow \mu^+ \mu^-$ . This decay is rare in the Standard Model as it occurs only via helicity suppressed loop diagrams. Its branching fraction can be significantly different in many New Physics models, especially with an extended Higgs sector. Therefore, the search for this decay provides a sensitive probe of physics beyond the Standard Model.

The decay rates of  $B_s^0 \rightarrow \ell^+ \ell^-$  are suppressed by a factor  $(m_\ell/m_B)^2$ . The suppression is therefore smallest for  $B_s^0 \rightarrow \tau^+ \tau^-$ , due to the large  $\tau$  mass.

Reconstructing  $B_s^0 \rightarrow \tau^+ \tau^-$  is a challenge and it is not clear that the Standard Model branching

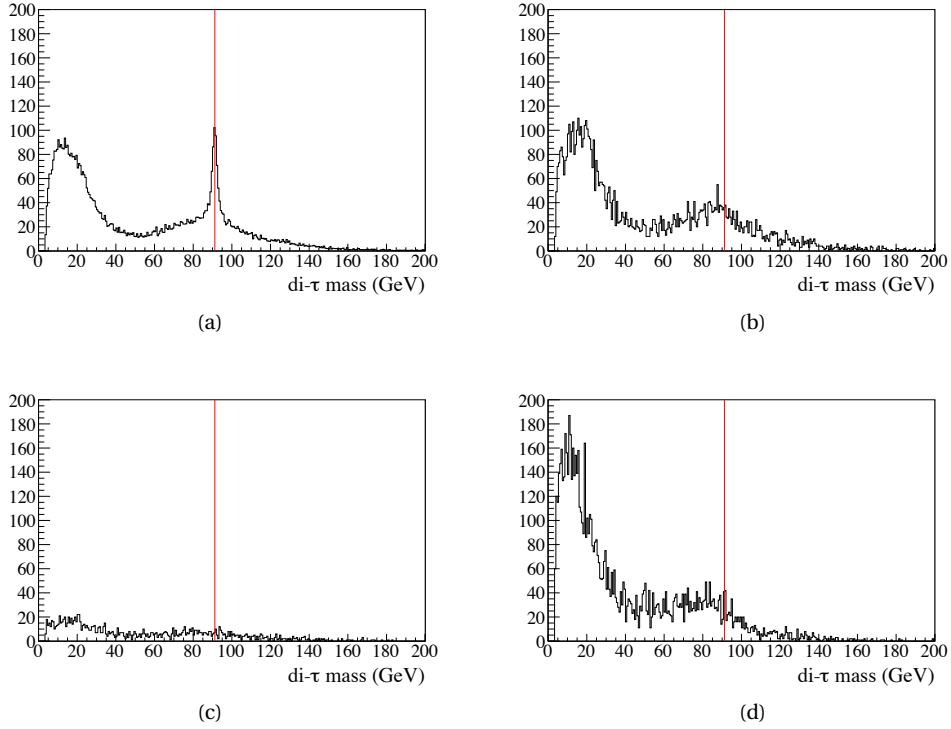


Figure 3.12: The mass distribution of the combined  $\tau$ -pair momentum solution of (a) the generated values, (b) the computationally reconstructed values, (c) the analytically reconstructed values and (d) the estimated values where a maximum angle between the  $\tau$  and  $3\pi$  momenta is assumed. The red lines indicate the value of the  $Z^0$  mass.

fraction can be measured within the lifetime of LHCb or its upgrade. However, the New Physics contribution may be considerable and it is well worth establishing an upper limit on the branching fraction of this decay.

### 3.4.1 Analytical calculation

The measurable variables of the  $B_s^0 \rightarrow \tau^+ \tau^-$  decay with  $\tau^- \rightarrow \pi^+ \pi^- \pi^- \nu_\tau$  are

- the B production vertex (primary vertex):  $\mathbf{pV}$ ,
- the two  $\tau$  decay vertices:  $\mathbf{dV}_1$  and  $\mathbf{dV}_2$ ,
- the 4-momenta of the two three-prongs:  $p_{13\pi}$  and  $p_{23\pi}$ .

The unknown quantities are

- the decay vertex of the B meson:  $\mathbf{bV}$ ,

### Chapter 3. Studies of $\tau$ reconstruction using simulated events

- the momentum of the B meson:  $\vec{p}_B$ ,
- the momenta of the two  $\tau$  leptons:  $\vec{p}_{1\tau}$  and  $\vec{p}_{2\tau}$ ,
- the momenta of the two neutrinos:  $\vec{p}_{1\nu}$  and  $\vec{p}_{2\nu}$ .

The masses of the B meson,  $\tau$  leptons and neutrinos are fixed to their experimentally determined values.

When two  $\tau$  leptons come from an unknown vertex, the reconstruction of their momenta is challenging. It is not possible to calculate the  $\tau$  momentum without knowing the angle between the  $\tau$  and  $3\pi$  momenta vectors [37] and it is not possible to calculate the B decay vertex without knowing the direction of the  $\tau$  momenta. A more convenient parameterization of the problem must therefore be found.

The B decay vertex must lie within the plane spanned by the three vertices  $\mathbf{pV}$ ,  $\mathbf{dV}_1$  and  $\mathbf{dV}_2$ . The vectors between the primary vertex and the first or second decay vertex are denoted by  $\vec{v}$  and  $\vec{w}$  respectively. The B and  $\tau$  momentum vectors are colinear with the spatial vectors between their production and decay vertices. Scale factors,  $L_{1\tau}$ ,  $L_{2\tau}$  and  $L_B$ , are used to relate the topological direction vectors to the particle momenta. The basic geometry of the plane in which the B and  $\tau$  momenta lie is depicted in Figure 3.13.

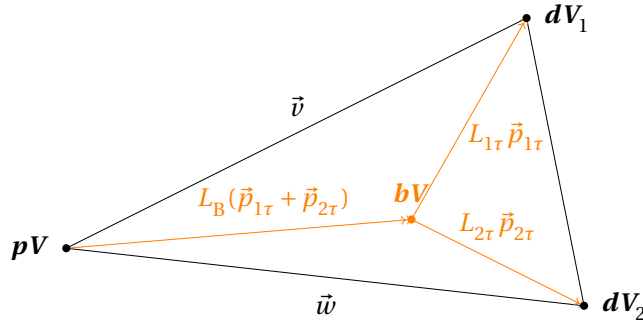


Figure 3.13: Geometry of the plane containing the B and both  $\tau$  momentum vectors.

The three relations linking the directional vectors to the momenta using scale factors are

$$\mathbf{dV}_1 - \mathbf{bV} = L_{1\tau} \vec{p}_{1\tau} \quad (3.16)$$

$$\mathbf{dV}_2 - \mathbf{bV} = L_{2\tau} \vec{p}_{2\tau} \quad (3.17)$$

$$\mathbf{bV} - \mathbf{pV} = L_B (\vec{p}_{1\tau} + \vec{p}_{2\tau}) \quad (3.18)$$

These relations can be rewritten to a single formula, eliminating the factors  $L_{1\tau}$ ,  $L_{2\tau}$  and  $L_B$ , as

$$\vec{v} \times \vec{p}_{1\tau} = -\vec{w} \times \vec{p}_{2\tau} \quad (3.19)$$

The second relation occurs through the fixing of the B mass:  $(p_{1\tau} + p_{2\tau})^2 = m_B^2$

$$E_{1\tau} E_{2\tau} - \vec{p}_{1\tau} \cdot \vec{p}_{2\tau} = \frac{1}{2} m_B^2 - m_\tau^2 \quad (3.20)$$

And finally two relations due to the fixing of the neutrino mass

$$(p_{1\tau} - p_{13\pi})^2 = (p_{2\tau} - p_{23\pi})^2 = 0 \quad (3.21)$$

and two from fixing the  $\tau$  mass

$$p_{1\tau}^2 = p_{2\tau}^2 = m_\tau^2 \quad (3.22)$$

The system to be solved thus consists of 8 equations and 8 unknowns, which are the two  $\tau$  4-momenta  $\{p_{1\tau}, p_{2\tau}\}$ . To simplify the algebra, the coordinate system is rotated such that the plane of the B decay lies on the  $xy$ -plane. By doing this the  $z$ -components of the two  $\tau$  momenta as well as the vectors  $\vec{v}$  and  $\vec{w}$  are set to 0. From this point onwards this will be assumed to be the case.

In 2D space the system reduces to 6 equations with 6 unknowns  $\{E_{1\tau}, p_{1\tau x}, p_{1\tau y}, E_{2\tau}, p_{2\tau x}, p_{2\tau y}\}$ . For a better overview Equations 3.19-3.22 can be rewritten with in 2D space with substituted variables as

$$x_1^2 + y_1^2 - z_1^2 = -1 \quad (3.23)$$

$$a_1 x_1 + y_1 + b_1 z_1 = c_1 \quad (3.24)$$

$$x_2^2 + y_2^2 - z_2^2 = -1 \quad (3.25)$$

$$a_2 x_2 + y_2 + b_2 z_2 = c_2 \quad (3.26)$$

$$k x_1 + l y_1 = m x_2 + y_2 \quad (3.27)$$

$$x_1 x_2 + y_1 y_2 - z_1 z_2 = d \quad (3.28)$$

Here  $x_1 = p_{1\tau x}/m_\tau$ ,  $y_1 = p_{1\tau y}/m_\tau$  and  $z_1 = E_{1\tau}/m_\tau$ . Thus  $a_1 = p_{13\pi x}/p_{13\pi y}$ ,  $b_1 = -E_{13\pi}/p_{13\pi y}$  and  $c_1 = (-m_\tau^2 - m_{13\pi}^2)/(2m_\tau p_{13\pi y})$ . The variables  $x_2, y_2, z_2$  and measurables  $a_2, b_2, c_2$  are defined similarly for the second  $\tau$  lepton. From Equation 3.20 it can be derived that  $d = (2m_\tau^2 - m_B^2)/(2m_\tau^2)$  and from Equation 3.19 that  $k = v_y/w_x$ ,  $l = -v_x/w_x$  and  $m = -w_y/w_x$ . Note that the space can still be conveniently rotated to set for instance  $m = 0$  or  $k = l$ ; here we will proceed without extra rotations applied.

Equation 3.23 represents a quadric surface: a hyperboloid of two sheets. Equation 3.24 is a plane. Together these two equations represent an ellipse in 3D space. This ellipse can be



### Chapter 3. Studies of $\tau$ reconstruction using simulated events

---

parameterized using one single variable, chosen to be  $t$ . To start the parameterization a point  $(x_0, y_0, z_0)$  on the ellipse is chosen. For a given value of  $z_0$ ,  $x_0$  is expressed as

$$x_0 = \frac{a_1(c_1 + b_1 z_0) \pm \sqrt{(a_1^2 + 1 - b_1^2)z_0^2 + 2b_1 c_1 z_0 - a_1^2 - b_1^2}}{1 + a_1^2} \quad (3.29)$$

Therefore there exists a solution for  $x_0$  if

$$(a_1^2 + 1 - b_1^2)z_0^2 + 2b_1 c_1 z_0 - a_1^2 - b_1^2 \geq 0 \quad (3.30)$$

As  $a_1^2 + 1 - b_1^2 < 0$  (the two components of the momentum squared are never larger than the energy squared), this represents a parabola which opens downward. It is therefore a safe choice to take

$$z_0 = \frac{-b_1 c_1}{a_1^2 + 1 - b_1^2} \quad (3.31)$$

as the starting value for  $z_0$ .

A pencil of planes, orthogonal to the  $xz$ -plane and crossing coordinate  $(x_0, y_0, z_0)$ , can be chosen as

$$x_1 = x_0 - t(z_1 - z_0) \quad (3.32)$$

where  $t$  is the new parameter in which the ellipse is parameterized. Substituting the variable  $x_1$  of Equation 3.24 by the relation given in Equation 3.32, the new expression can be combined with Equation 3.23 to give a quadratic solution for  $z_1$  expressed in terms of  $t$ . One of the solutions for  $z_1$  is known to be  $z_0$ . Discarding this known solution leaves a general algebraic expression for  $z_1$  in terms of  $t$ .

$$z_1 = \frac{(z_0 a_1^2 + z_0) t^2 + 2(x_0 - a_1 c_1 + a_1^2 x_0) t + 2b_1 y_0 + b_1^2 z_0 + z_0}{(a_1^2 + 1) t^2 - 2a_1 b_1 t + b_1^2 - 1} \quad (3.33)$$

It follows that  $x_1$  and  $y_1$  can be expressed in terms of  $t$  as

$$x_1 = \frac{(x_0 a_1^2 - x_0 + 2a_1 y_0) t^2 + 2(b_1 c_1 + b_1^2 z_0 - z_0) t + b_1^2 x_0 - x_0}{(a_1^2 + 1) t^2 - 2a_1 b_1 t + b_1^2 - 1}, \quad (3.34)$$

$$y_1 = \frac{(-y_0 a_1^2 + y_0 + 2a_1 x_0) t^2 + 2(a_1 z_0 - b_1 x_0 + a_1 b_1 y_0) t - b_1^2 y_0 - y_0 - 2b_1 z_0}{(a_1^2 + 1) t^2 - 2a_1 b_1 t + b_1^2 - 1} \quad (3.35)$$

Both the numerator and the denominator are of order 2 in  $t$  for  $x_1$ ,  $y_1$  and  $z_1$ . In addition, the three variables share the same denominator. These expressions will be denoted by

$$x_1 = \frac{t_x}{t_n}, \quad y_1 = \frac{t_y}{t_n} \quad \text{and} \quad z_1 = \frac{t_z}{t_n} \quad (3.36)$$

to retain the general overview.

Equations 3.26-3.28 are now used to express  $x_2$ ,  $y_2$  and  $z_2$  in terms of  $t$ . The result for each variable is a fraction with both the numerator and denominator of order 4 in  $t$ .

$$x_2 = \frac{(kt_x + lt_y)(-t_z - b_2 t_y) + t_n(c_2 t_z + b_2 d t_n)}{t_n(a_2 t_z - m t_z + b_2 t_x - m b_2 t_y)} \quad (3.37)$$

$$y_2 = \frac{(kt_x + lt_y)(b_2 t_x + a_2 t_z) - m t_n(c_2 t_z + b_2 d t_n)}{t_n(a_2 t_z - m t_z + b_2 t_x - m b_2 t_y)} \quad (3.38)$$

$$z_2 = \frac{(kt_x + lt_y)(a_2 t_y - t_x) + t_n(c_2 t_x - c_2 m t_y - a_2 d t_n + m d t_n)}{t_n(a_2 t_z - m t_z + b_2 t_x - m b_2 t_y)} \quad (3.39)$$

Equation 3.25 is so far unused and substituting the expressions of  $x_2$ ,  $y_2$  and  $z_2$  in terms of  $t$  into this relation leaves a single polynomial of order 8 in  $t$ . This polynomial will be referred to by  $p_0(t)$ .

**Polynomial solutions** The polynomial cannot be solved analytically. However, it has the advantage that parameter  $t$  is limited to an interval of approximately  $(-1, 1)$ . The distribution of  $t$  is depicted in Figure 3.14. Algorithms exist, like the algorithm of Sturm [38], that determine

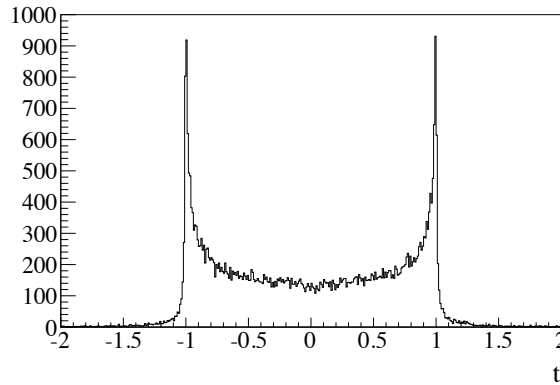


Figure 3.14: The distribution of parameter  $t$  as calculated from the generated 4-vectors of 25,000  $B_s^0 \rightarrow \tau^+ \tau^-$  events.

the number of roots within a certain interval. In order to apply Sturm's theorem the polynomial has to be expressed in its monomial basis. However, the values of the roots of  $p_0(t)$  are highly sensitive to perturbations in the coefficients of the polynomial. Expressing  $p_0(t)$  in its monomial basis changes the location of its roots significantly. Figure 3.15 shows the outcome of  $p_0(t)$  before and after bracket expansion. The true solution of the polynomial is lost after expansion. The problem is thus ill-conditioned (similar to Wilkinson's polynomial [39]). The solutions of  $p_0(t) = 0$  will therefore have to be located by scanning over a specified interval in small enough steps to result into the required roots.

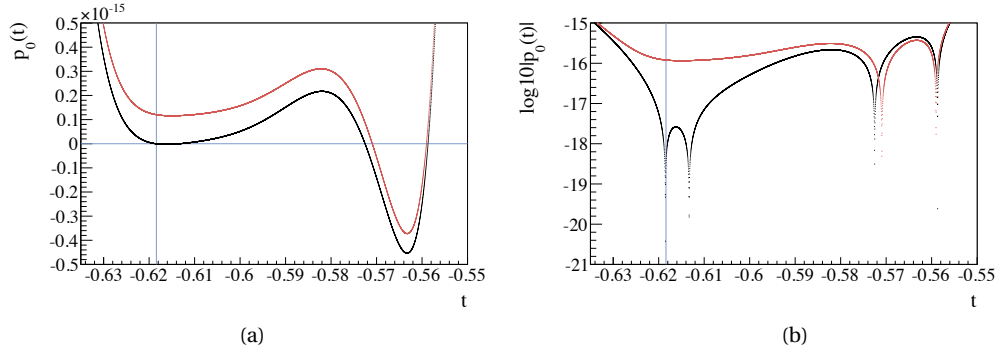


Figure 3.15: The outcome of the polynomial  $p_0$  as a function of  $t$  for a given event, depicted by (a) the value of  $p_0(t)$  and (b) the value of  $\log_{10}(|p_0(t)|)$ . In black the original unexpanded outcome and in red the outcome after expanding to a monomial basis. The blue line represents the true value of parameter  $t$ .

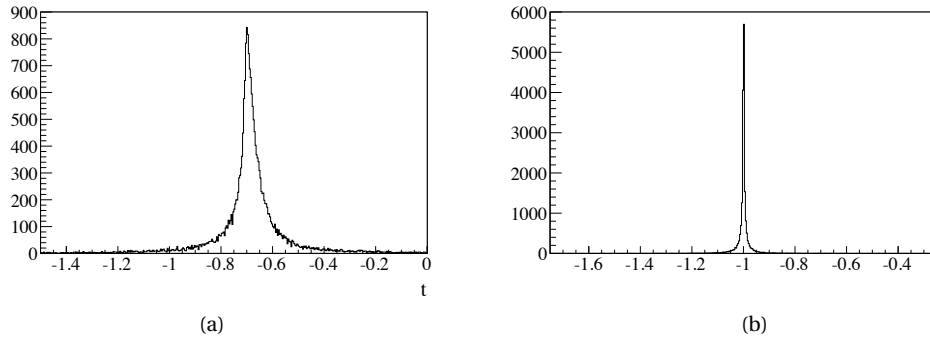
Although it is an 8<sup>th</sup> order polynomial, it has usually 2 or 4 roots, with one of them corresponding to the true solution. Whether it is possible to distinguish between these solutions depends on the  $B_s^0 \rightarrow \tau^+ \tau^-$  decay specific kinematic and topological distributions. In section 3.4.1 the decay time distribution is discussed.

**Additional space rotations** As mentioned in the previous section, an additional space rotation in the  $xy$ -plane can be made to simplify the problem. The space can be rotated such that  $k = l$  or  $m = 0$  for instance. This does not change the general outcome of the problem; there is still an 8<sup>th</sup> order polynomial to solve. But it simplifies the formulas and affects the distribution of parameter  $t$ .

The distributions of  $t$ , for the cases  $k = l$  and  $m = 0$ , are depicted in Figure 3.16. For both cases, the interval of possible  $t$  solutions has decreased compared to the case where no extra rotation is made.

**Accuracy and efficiency**

The accuracy and efficiency of the solutions found by solving  $p_0(t) = 0$  are dependent of the step size,  $\delta t$ , which is used to scan over the pre-defined interval  $[t_{\min}, t_{\max}] = [-2, 2]$  of possible solutions. For different step sizes, the calculation efficiency,  $\epsilon_{\text{cal}}$ , and the average number of roots found are given in Table 3.1. The efficiency is given by the percentage of decays for which at least one solution can be found for  $p_0(t) = 0$ , i.e. more than one solution per decay does not increase the efficiency. As shown in Table 3.1, the efficiency increases as the step size decreases. At the same time, the average number of roots increases. Additional real roots are found, but also duplicate roots are calculated as the value of  $p_0(t)$  may fluctuate around zero due to rounding errors, when there is only one true root.


 Figure 3.16: The  $t$  distribution after the  $xy$ -plane is rotated such that (a)  $k = l$  and (b)  $m = 0$ .

step size $\delta t$	efficiency $\epsilon_{\text{cal}}$	average number of roots
0.01	72.7%	2.529
0.005	80.5%	2.638
0.002	87.6%	2.749
0.001	90.7%	2.806
0.0005	92.4%	2.847
0.0002	93.5%	2.893
0.0001	93.9%	2.943
0.00005	94.1%	3.042
0.00002	94.1%	3.350

 Table 3.1: The calculation efficiency,  $\epsilon_{\text{cal}}$ , and the average number of roots found for different values of  $\delta t$ .

Figure 3.17 depicts the difference between the true value of  $t$  and the calculated value of  $t$  which is closest to the truth (referred to as the best calculated value). To better illustrate the resolution, the logarithm of the absolute value of the difference is taken. For larger step sizes, the resolution is dominated by the step size. This results in the sharp peak structures in Figure 3.17. For  $\delta t = 0.00002$ , this sharp peak structure does not show and for  $\delta t = 0.00005$  it has completely saturated.

However, it is also important to keep in mind the speed of the program. As the efficiency does not increase much for step sizes smaller than 0.0001 and as the effect on the resolution is limited, it is chosen to continue this study with  $\delta t = 0.0001$ . The plots shown and results quoted hereafter are thus based on the solutions found when using  $\delta t = 0.0001$ .

Although the parameter interval  $[t_{\min}, t_{\max}]$  after an extra space rotation is significantly reduced, it is not necessarily advantageous to do so. As the same number of solutions occur on a smaller interval, there are more fluctuations around zero. In the case of the extra space rotation such that  $m = 0$ , the average number of roots found for  $\delta t = 0.0002$  is 1.7, whereas for  $\delta t = 0.00002$  it is 14.3. Although it is a route which can be explored further, no extra space

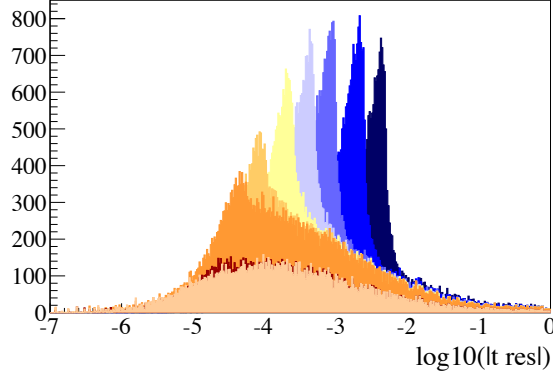


Figure 3.17: The difference between the true value of  $t$  and the best calculated value of  $t$  for step sizes  $\delta t = 0.01$  to  $\delta t = 0.00002$  (as in Table 3.1) ranging in colour from dark blue to light orange.

rotations are made to obtain the results in this thesis.

### With generated quantities

By solving  $p_0(t) = 0$  possible  $\tau$  lepton momenta, B momentum and B decay vertices are determined that satisfy all topological and kinematic constraints. However, only one of the solutions corresponds best to the truth. The solution which corresponds best to the truth based on the  $t$  resolution (referred to as the best solution) is chosen to determine the accuracy with which the variables  $|\vec{p}_\tau|$ ,  $|\vec{p}_B|$  and  $bV$  can be calculated. Here, the generated values of the momenta and vertices are used to calculate the solutions.

Figure 3.18 shows the asymmetry distributions of the  $\tau$  and B momenta. An FWHM of  $2.0 \cdot 10^{-4}$  for the  $\tau$  momentum and  $2.9 \cdot 10^{-4}$  for the B momentum corresponds to a relative error of 0.04% and 0.06% respectively.

In Figure 3.19 the resolutions of the B decay vertex are depicted. Note that only the  $x$ -component,  $bV_x$ , and  $y$ -component,  $bV_y$ , are depicted, as the coordinate system has been rotated such that the  $z$ -component of the B decay vertex is equal to the  $z$ -component of the primary vertex and is therefore fixed. These  $x$  and  $y$ -components are thus not the conventional  $x$  and  $y$ -components of the LHCb frame. Resolutions of  $0.30 \mu\text{m}$  in  $x$  and  $0.42 \mu\text{m}$  in  $y$  are obtained.

### With reconstructed quantities

In this section, reconstructed particles that match to the signal decay are selected. Before the efficiency of the calculation can be determined, the reconstruction efficiency needs to be

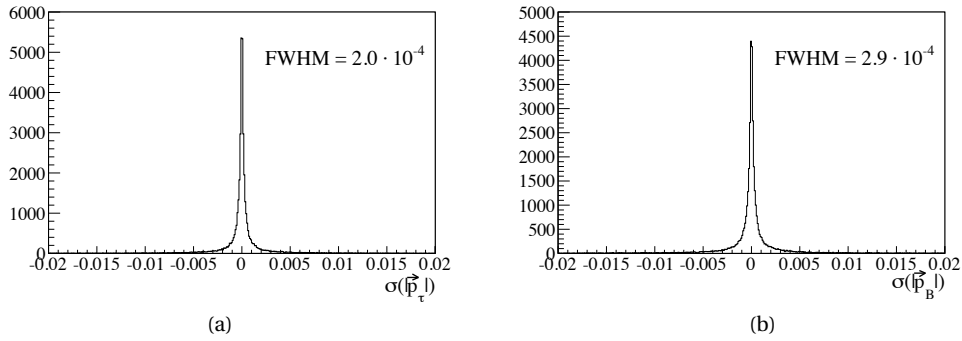


Figure 3.18: The (a)  $|\vec{p}_\tau|$  and (b)  $|\vec{p}_B|$  asymmetries between the best calculated momentum and the true momentum.

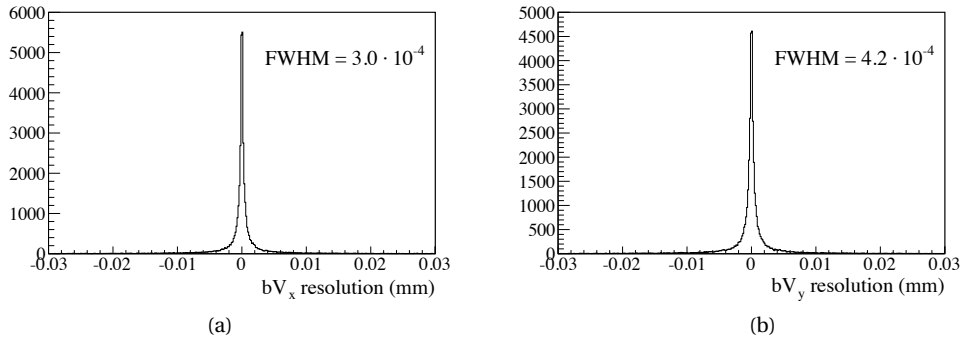


Figure 3.19: The (a)  $bV_x$  and (b)  $bV_y$  resolution between the best calculated vertex and the true vertex.

considered. The reconstruction efficiency is the percentage of decays for which all six final state pions are reconstructed in LHCb. The MC data sample solely contains events for which all decay daughters travel within 400 mrad of the beam axis. Of these events approximately 5.7% is fully reconstructed in LHCb. No cuts on the reconstructed particles have been made.

When the six pions are fully reconstructed, 47% of decays can be formulated by the polynomial  $p_0(t)$ . The likelihood of finding a solution is approximately 33%. That means, in 33% of the events, one or more roots of the polynomial  $p_0(t)$  can be determined. The remaining 14% of decays results in a valid polynomial, but no roots are found. For the other 53% of the cases, either the system of Equations 3.23 and 3.24 or of Equations 3.25 and 3.26 does not have an analytical solution. The plane of possible  $\tau$  momenta that obey the  $\tau$  mass constraint does not intersect the hyperboloid of possible momenta that obey the neutrino mass constraint. Therefore an ellipse cannot be constructed nor parameterized.

Figure 3.20 shows the asymmetries  $\sigma(|\vec{p}_\tau|)$  and  $\sigma(|\vec{p}_B|)$  of the reconstructed  $\tau$  and B momenta.

### Chapter 3. Studies of $\tau$ reconstruction using simulated events

The FWHM of the distributions are 0.07 and 0.06, which corresponds to a relative error of 15% and 13% respectively.

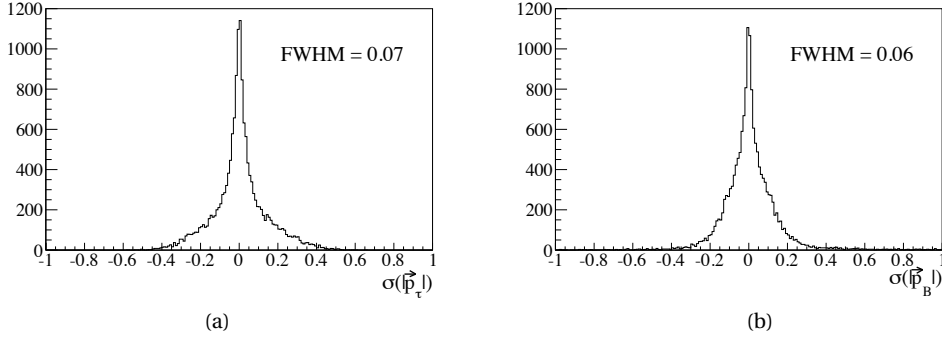


Figure 3.20: The (a)  $|\vec{p}_\tau|$  and (b)  $|\vec{p}_B|$  asymmetries between the best reconstructed momentum and the true momentum.

In Figure 3.21 the resolutions of the B decay vertex are depicted. Resolutions of 1.4 mm in  $x$  and 1.8 mm in  $y$  are obtained.

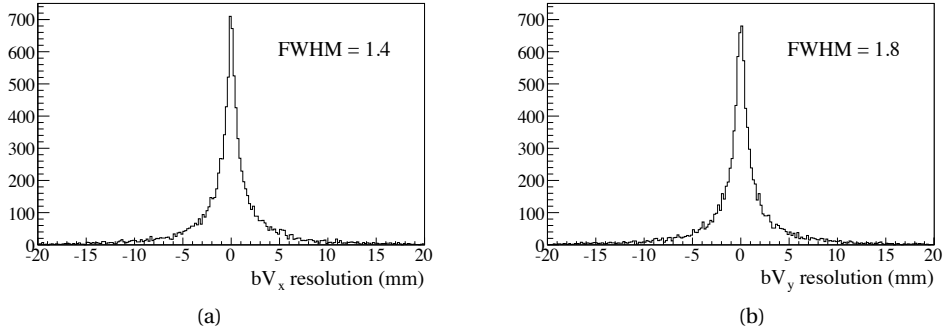


Figure 3.21: The (a)  $bV_x$  and (b)  $bV_y$  resolution between the best reconstructed vertex and the true vertex.

The calculation efficiency and selection efficiency are not uncorrelated. It is likely that in any selection only decay vertices are selected which are sufficiently distant from the primary vertex. Figure 3.22 shows the different vertex distance distributions of the decays with and without a successfully calculated solution. It shows that for small distances between the primary vertex and either of the  $\tau$  decay vertices, it is less likely to find a solution. When a cut is made at  $|dV_z - pV_z| > 4$  mm for both vertices in the LHCb coordinate system, the calculation efficiency for the remaining candidates goes up from 33% to 42%. The momentum asymmetries are not notably affected by this cut. Additional selection cuts may improve the calculation efficiency further.

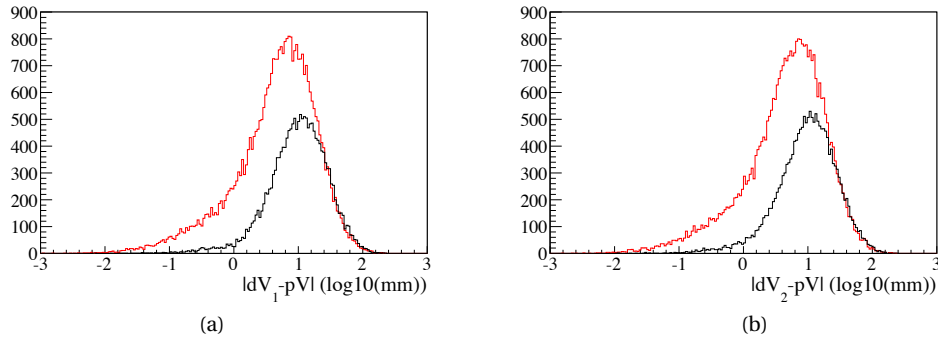


Figure 3.22: The distances between the primary vertex and the (a)  $\tau_1$  decay vertex and the (b)  $\tau_2$  decay vertex. In black the distances of the decays for which a solution was successfully calculated and in red the distances of the decays for which no solution was found.

### Decay time distributions

Generally there are 2 or 4 possible B vertices, of which only one matches the true vertex. Whether it is possible to distinguish between correct and incorrect solutions will be dependent on the decay specific distributions of kinematic and topological variables. In this section, only the decay time distributions of the  $\tau$  lepton and B meson are discussed. The  $\tau$  lifetime value is  $\tau_\tau = (2.906 \pm 0.010) \cdot 10^{-13}$  s, whereas the B lifetime is  $\tau_B = (1.452 \pm 0.041) \cdot 10^{-12}$  s [5].

In Figures 3.23 and 3.24 the  $\tau$  and B distributions of the calculated decay time determined with the generated quantities are depicted. The figures show the  $\tau$  and B decay time distributions of (a) the best calculated solutions and of (b) the remaining solutions. The best calculated solutions correspond to those of which parameter  $t$  differs least from its true value. Figure 3.25 shows (left) the  $\tau$  and (right) the B decay time distribution of the reconstructed particles for the best calculated solutions in black and for the remaining solutions in blue (scaled). Although there are differences between the distributions, they are not large enough to distinguish between solutions and are negligible for reconstructed data.

It can be concluded that the decay time distributions of the best and remaining reconstructed particles are indistinguishable. To model the decay time distribution, it is therefore unnecessary to determine the correct solution. The different decay times found per event can be weighted according to the number of solutions found. The result will be the same decay time distribution.

### 3.4.2 Constrained fit

A constrained fit as discussed in Section 3.2.3 can also be applied here. However, an appropriate new description of the system and corresponding parameters need to be chosen carefully to ensure convergence to a minimum  $\chi^2$  value. The standard measured quantities are the



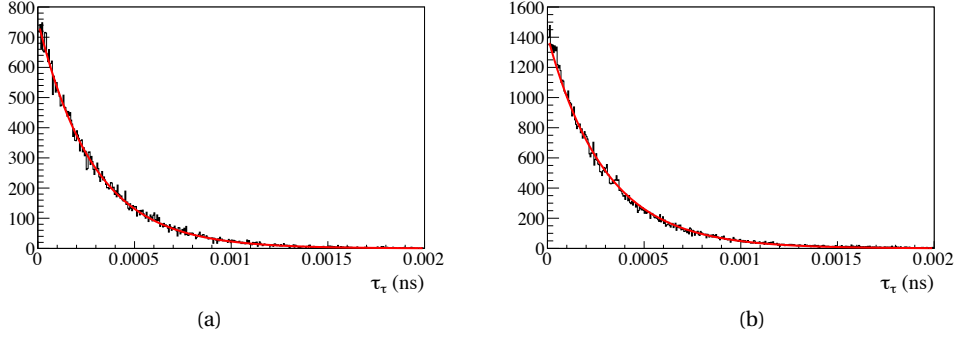


Figure 3.23: The decay time distribution of (a) the set of best  $\tau$  momentum solutions which gives  $\tau_\tau = (2.826 \pm 0.020) \cdot 10^{-13}$  s and (b) the set of remaining  $\tau$  momentum solutions calculated on generation level with  $\tau_\tau = (2.934 \pm 0.016) \cdot 10^{-13}$  s. In red the exponential functions fitted to the data.

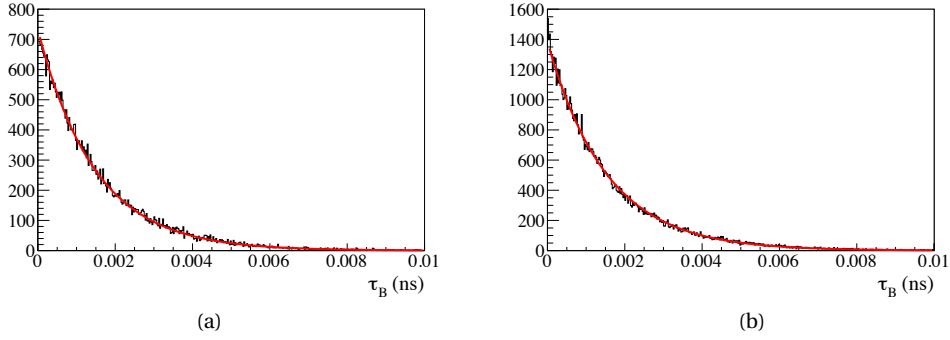


Figure 3.24: The decay time distribution of (a) the set of best B momentum solutions which give  $\tau_B = (1.451 \pm 0.010) \cdot 10^{-12}$  s and (b) the set of remaining B momentum solutions calculated on generation level with  $\tau_B = (1.510 \pm 0.008) \cdot 10^{-12}$  s. In red the exponential functions fitted to the data.

primary vertex,  $\mathbf{pV}$ , and for both  $\tau$  leptons the decay vertex,  $\mathbf{dV}$ , and the  $3\pi$  4-momentum,  $(E_{3\pi}, \vec{p}_{3\pi})$ . In addition, the combined momentum of the 6 pions,  $(E_{6\pi}, \vec{p}_{6\pi})$ , is calculated. A small variation of the  $3\pi$  energy and its momentum can lead to a negative  $3\pi$  mass. It is therefore more stable to use the  $3\pi$  mass in the description rather than its energy and a convenient choice of variable is  $m_{3\pi}^2$ . The same holds for the  $6\pi$  mass. The chosen description of the system consists of the following 21 quantities

$$h(x) = \left\{ \mathbf{pV}, \mathbf{dV}_1, \vec{p}_{13\pi}, m_{13\pi}^2, \mathbf{dV}_2, \vec{p}_{23\pi}, m_{23\pi}^2, \vec{p}_{6\pi}, m_{6\pi}^2 \right\} \quad (3.40)$$

The value of  $m_{6\pi}$  is needed to constrain the B mass in the description of the model. It can be used because it is not a linear combination of the other variables. The  $6\pi$  momentum is fully

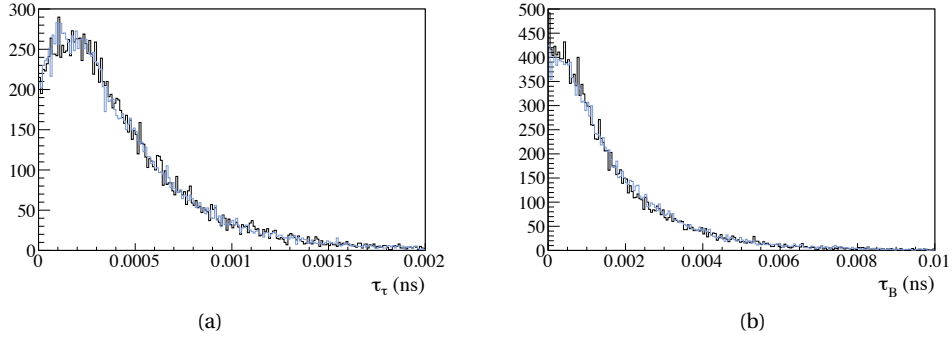


Figure 3.25: The decay time distributions of (a) the  $\tau$  momentum solutions and (b) the B momentum solutions calculated on reconstruction level. The decay time distribution of the set of best calculated momenta is drawn in black and the decay time distribution of the set of remaining momenta in blue (scaled).

determined by the addition of momenta of the two  $3\pi$  pairs. However, the  $6\pi$  momentum is included because a momentum covariance matrix is assigned to each combined particle. The full covariance matrix consists of the individual particle covariance matrices, which do not relate the two  $3\pi$  momenta to the combined  $6\pi$  momentum. The matrix is therefore still invertible to obtain a well-defined weight matrix. If the value of  $m_{6\pi}$  is linked to the individual  $3\pi$  momenta, it is possible to take the redundant values of  $\vec{p}_{6\pi}$  out of the equation.

The Jacobian matrix is applied to the covariance matrix in order to make it compatible with the change of variable. The vertices and momenta of the measured variables together with their components in the covariance matrix are rotated such that the  $z$ -components of the B and  $\tau$  momenta are 0.

The free parameters which are chosen to describe the system are the primary vertex,  $\mathbf{pV}$ , the three scale factors,  $L_{1\tau}$ ,  $L_{2\tau}$  and  $L_B$ , the  $\tau$  momenta,  $\vec{p}_{1\tau}$  and  $\vec{p}_{2\tau}$  and the neutrino momenta  $\vec{p}_{1\nu}$  and  $\vec{p}_{2\nu}$ . There are thus 16 parameters.

$$x = \left\{ \mathbf{pV}, L_{1\tau}, L_{2\tau}, L_B, p_{1\tau x, y}, \vec{p}_{1\nu}, p_{2\tau x, y}, \vec{p}_{2\nu} \right\} \quad (3.41)$$

The  $\tau$  masses are fixed by defining  $E_\tau = \sqrt{m_\tau^2 + |\vec{p}_\tau|^2}$ . The relation used to describe the  $3\pi$  mass

$$m_{3\pi}^2 = m_\tau^2 - 2E_\tau |\vec{p}_\nu| + 2\vec{p}_\tau \cdot \vec{p}_\nu \quad (3.42)$$

fixes the neutrino masses to 0. The  $6\pi$  mass is used to then fix the B mass through the following

relation:

$$\begin{aligned}
 m_{6\pi}^2 = & m_B^2 - 2|\vec{p}_{1\nu}|\sqrt{m_B^2 + |\vec{p}_{1\tau} + \vec{p}_{2\tau}|^2} + 2\vec{p}_{1\nu} \cdot (\vec{p}_{1\tau} + \vec{p}_{2\tau}) \\
 & - 2|\vec{p}_{2\nu}|\sqrt{m_B^2 + |\vec{p}_{1\tau} + \vec{p}_{2\tau}|^2} + 2\vec{p}_{2\nu} \cdot (\vec{p}_{1\tau} + \vec{p}_{2\tau}) \\
 & + 2|\vec{p}_{1\nu}||\vec{p}_{2\nu}| - 2\vec{p}_{1\nu} \cdot \vec{p}_{2\nu}
 \end{aligned} \tag{3.43}$$

The topological constraints are given by

$$d\mathbf{V}_1 = \mathbf{pV} + L_B(\vec{p}_{1\tau} + \vec{p}_{2\tau}) + L_{1\tau}\vec{p}_{1\tau} \tag{3.44}$$

$$d\mathbf{V}_2 = \mathbf{pV} + L_B(\vec{p}_{1\tau} + \vec{p}_{2\tau}) + L_{2\tau}\vec{p}_{2\tau} \tag{3.45}$$

Two methods of minimisation are considered. The first uses TMinuit [40], a pre-programmed minimisation algorithm. The second is the Newton-Raphson method, which tries to find the root of the  $\chi^2$  derivative. Both methods rely on well chosen initial values of the parameters to avoid getting stuck in local minima.

### Fit result and efficiency

The fit methods are used consecutively; i.e. if the problem does not converge with one of the methods, the other method is applied. These results are thus based on the best combined result of the two fit methods. TMinuit has the advantage that lower and upper limits can be set for each variable.

For 24 degrees of freedom, the  $\chi^2$  distribution theoretically obeys the following proportions

	90%	95%	99%
$\chi^2$	33.2	36.4	42.0

In this study, for a  $\chi^2 < 33.2$ , the fit efficiency is 43%. The  $\chi^2$  of many decays does therefore not reach its global minimum, which must be due to an insufficient initial values. The solutions of the decays which have converged to the smallest  $\chi^2$  must be verified to be valid solutions.

Figure 3.26 depicts the true distributions of scale factors  $L_B$  and  $L_{1\tau}$  (which is equivalent to the distribution of  $L_{2\tau}$ ). Based on this distribution, the lower and upper limits of the TMinuit constraints for all scale factors have been set to  $10^{-7}$  and  $10^{-3}$  respectively. The solution is expected within these limits.

Figure 3.27 shows that  $L_B$  often converges to zero during the fitting process. The same is true for the  $L_{1\tau}$  and  $L_{2\tau}$  scale factors. The  $\chi^2$  value in this case can be sufficiently low, but represents a faulty solution. As can be seen in Figure 3.27(b), the decay time then also approaches zero. These solutions should therefore not be taken into account when calculating the fit efficiency. When a scale factor tends to zero, the topological constraint on either the B or on one of the  $\tau$

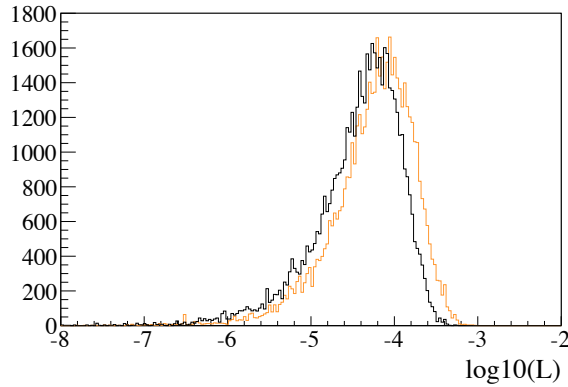


Figure 3.26: The generated values of the scale factors  $L_B$  (orange) and  $L_{1\tau}$  (black).

momenta disappears and the particles ‘decouple’, which results in an invalid solution with a low  $\chi^2$ .

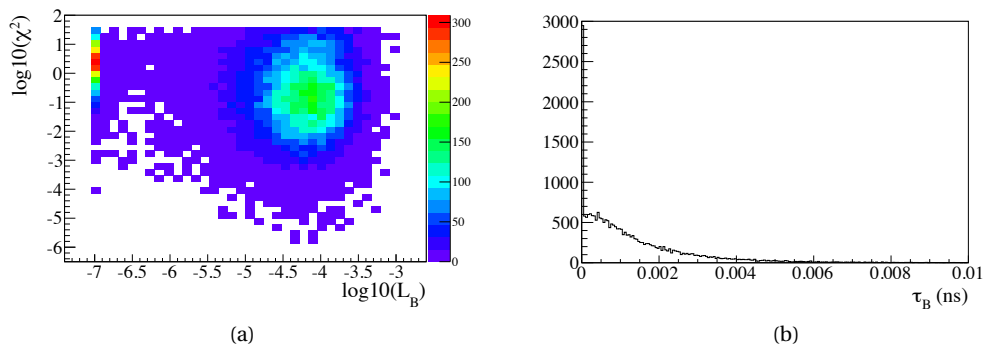


Figure 3.27: (a) The value of  $\log_{10}(\chi^2)$  versus the scale factor value  $\log_{10}(L_B)$ . (b) The decay time distribution of the B momenta obtained by fitting the signal decay using constraints.

Eliminating the fit solutions where one of the scale factors has decreased below  $10^{-6}$  leaves a fit efficiency of 33%. This is equivalent to the efficiency of the analytical calculation method.

It is possible that the zero decay time solutions can still be used in analyses when solely the  $\tau$  momentum obtained in the fit is considered. This possibility needs to be further investigated. Chapter 4 discusses the  $\tau$  momentum solutions that correspond to zero decay time solutions.

### 3.4.3 Conclusion

The  $B_s^0 \rightarrow \tau^+ \tau^-$  decay with  $\tau^- \rightarrow \pi^+ \pi^- \pi^- \nu_\tau$  is theoretically reconstructable. In order to find the B and  $\tau$  momenta solutions, the roots of an 8<sup>th</sup> order polynomial need to be determined. These roots are limited to a specified interval and can be calculated by scanning this interval

in a certain number of steps.

The efficiency of this calculation is approximately 33%. However, no selection cuts are made prior to the calculation. It has been shown that the calculation efficiency and the selection efficiency are not uncorrelated. Therefore the final calculation efficiency cannot be determined until a selection has been established.

Albeit an 8<sup>th</sup> order polynomial, it generally has either 2 or 4 roots. Only one of these roots matches the truth. Whether it is possible to distinguish between the solutions is dependent on the decay specific topological and kinematic characteristics. The decay time distributions for all solutions are very similar and do not give any usable information on which solution best matches the truth. As the distributions are practically indistinguishable, it is not necessary to choose one of the solutions. The decay time solutions can be weighted according to the number of roots found for the decay.

Exploiting the errors on the measured quantities by using a fit method has not been beneficial to the overall efficiency. Perhaps it is possible to avoid the tendency of the scale factors to reduce to zero by formulating the system differently. There may also be a better educated initial guess that can be used by the fit programs, which does not use the calculation described in Section 3.4.1.

Reconstructing  $B_s^0 \rightarrow \tau^+ \tau^-$  remains a challenge, but is not impossible. Further study needs to be performed in order to fully understand the possibilities and restrictions of the signal reconstruction, in addition to its efficiency on background reduction.

The Standard Model predicts a branching fraction of  $\mathcal{B}(B_s^0 \rightarrow \tau^+ \tau^-) = 8.9 \times 10^{-7}$  [41]. This is two orders of magnitude larger than the  $B_s^0 \rightarrow \mu^+ \mu^-$  branching fraction, due to helicity suppression. Taking into account that both tau leptons have to decay into three pions and a neutrino reduces the benefit to a factor 2.3. At LHCb the trigger efficiency can be estimated to be  $\sim 20\%$  and the reconstruction efficiency is approximately 5.7%. This reduces the number of relevant  $B_s^0 \rightarrow \tau^+ \tau^-$  events reconstructed in LHCb to be 2.6% of the  $B_s^0 \rightarrow \mu^+ \mu^-$  events, before the selection process starts. However, New Physics contributions could enhance the  $B_s^0 \rightarrow \tau^+ \tau^-$  branching fraction more than its muonic counterpart.

### 3.5 Further event reconstruction possibilities including a $\tau$ lepton

Although the study of  $B_s^0 \rightarrow \tau^+ \tau^-$  is interesting, its reconstruction is the most complicated. There are other decay channels, which reconstruction is simplified by an additional track or vertex, that also deserve consideration. In this section the reconstruction possibilities of the rare decays  $B_{(s)}^0 \rightarrow \mu^+ \tau^-$ ,  $B^+ \rightarrow K^+ \tau^+ \tau^-$  and  $B^0 \rightarrow K^* \tau^+ \tau^-$  are discussed.

### 3.5. Further event reconstruction possibilities including a $\tau$ lepton

#### 3.5.1 The lepton flavour violating decay $B_{(s)}^0 \rightarrow \mu^+ \tau^-$

As it has been established that the neutrino is not massless, it is conceivable that the lepton flavour violating decay of  $B_{(s)}^0 \rightarrow \mu^+ \tau^-$  could occur through a box diagram involving an exchange of a neutrino. However, with the expected neutrino mass below the eV range, this decay is suppressed to the extent that it is unmeasurable at the LHC experiments. The observation of this decay would therefore be evidence of New Physics. The current best measured limit is  $\mathcal{B}(B^0 \rightarrow \mu^+ \tau^-) < 2.2 \cdot 10^{-5}$  by the BaBar collaboration [42]. No limit has been set on the  $B_s^0 \rightarrow \mu^+ \tau^-$  decay channel.

Topologically, this decay is a simplification of the  $B_s^0 \rightarrow \tau^+ \tau^-$  decay, as one of the  $\tau$  leptons is replaced by a fully reconstructable track. The reconstruction plane of the  $B_{(s)}^0 \rightarrow \mu^+ \tau^-$  decay is defined by the production vertex of B (the primary vertex) and the  $\mu$  momentum vector. Rotating the coordinate system such that these vectors lie solely in the  $xz$ -plane, transforms the decay into a 2D planar problem.

The reconstruction process can be simplified by choosing a transformation such that the reconstructed  $\mu$  track coincides with the  $z$ -axis. In this case, the equations above simplify by using the fact that  $p_{\mu z} = |\vec{p}_\mu|$ . In addition, it follows that the  $x$ -component of the production vertex,  $bV_x$ , of the  $\tau$  lepton is a constant chosen to be 0.

The relations between the known vertices and the momenta are given by

$$dV - bV = L_\tau \vec{p}_\tau \quad (3.46)$$

$$bV - pV = L_B (\vec{p}_\tau + \vec{p}_\mu) \quad (3.47)$$

From its  $x$  and  $z$ -components it follows that

$$p_{\tau z} = \frac{pV_z - dV_z}{pV_x - dV_x} p_{\tau x} - \frac{pV_x |\vec{p}_\mu|}{pV_x - dV_x} = a p_{\tau x} + b \quad (3.48)$$

Although the  $\tau$  momentum solution can be parameterized using the  $\tau$  mass and neutrino mass constraints, as demonstrated in Section 3.4.1, the simpler solution is obtained directly through substitution. The neutrino mass constraint of Equation 3.1 allows the  $\tau$  energy to be expressed linearly in terms of  $p_{\tau x}$  as

$$E_\tau = \frac{p_{3\pi x} + a p_{3\pi z}}{E_{3\pi}} p_{\tau x} + \frac{m_\tau^2 + m_{3\pi}^2 + 2b p_{3\pi z}}{2E_{3\pi}} = c p_{\tau x} + d \quad (3.49)$$

In addition, the  $\tau$  mass constraint of Equation 3.2 limits the relation between  $\tau$  energy and  $p_{\tau x}$  quadratically as

$$E_\tau^2 = (1 + a^2) p_{\tau x}^2 + 2ab p_{\tau x} + m_\tau^2 + b^2 = e p_{\tau x}^2 + f p_{\tau x} + g \quad (3.50)$$

### Chapter 3. Studies of $\tau$ reconstruction using simulated events

Combining these relation results in the single equation

$$0 = (e - c^2)p_{\tau x}^2 + (f - 2cd)p_{\tau x} + (g - d^2) \quad (3.51)$$

with the two solutions for  $p_{\tau x}$  given by

$$p_{\tau x} = \frac{-(f - 2cd) \pm \sqrt{(f - 2cd)^2 - 4(e - c^2)(g - d^2)}}{2(e - c^2)} \quad (3.52)$$

Figures 3.28(a) and (b) show the analytical B mass results created with generated quantities and with MC truth matched reconstructed data, respectively. The distribution which is based on the  $\tau$  momenta which match the true values best is depicted in black, the distribution obtained by the other solutions in blue. Using generated values for the reconstruction a FWHM of 4 MeV is obtained for the B mass resolution. Performing the same calculation with reconstructed quantities increases the width to approximately 120 MeV. Due to the quadratic nature of the solution, the  $\tau$  momentum can be calculated in 47% of the cases.

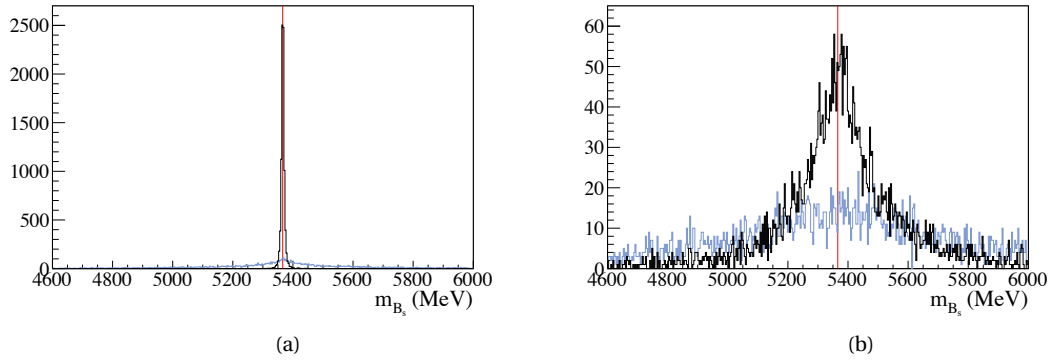


Figure 3.28: Analytically calculated B mass distribution for (a) generated data and (b) MC truth matched reconstructed data. The MC truth matching distribution is depicted in black, the other solutions are shown in blue. The red line indicates the theoretical value of the B mass.

Fitting the decay improves both the B mass width and the reconstruction efficiency. As measured particles the  $3\pi$  4-momentum is available as well as the combined  $3\pi-\mu$  4-momentum. In addition, the primary vertex,  $\mathbf{pV}$ , is measured. The description of the system used for the constrained fit thus becomes:

$$h(x) = \{\mathbf{pV}, \mathbf{dV}, \vec{p}_{3\pi}, m_{3\pi}^2, \vec{p}_{3\pi-\mu}, m_{3\pi-\mu}^2\} \quad (3.53)$$

The chosen parameters are

$$x = \{\mathbf{pV}, L_\tau, L_B, \vec{p}_\tau, \vec{p}_\nu, \vec{p}_\mu\} \quad (3.54)$$

### 3.5. Further event reconstruction possibilities including a $\tau$ lepton

For the fitting of the decay TMinuit is used. A total of 98% of the events were reconstructed with a  $\chi^2 < 10$ . The result on the B mass is shown in Figure 3.29. The constrained fit reduces the FWHM of the B mass to 24 MeV.

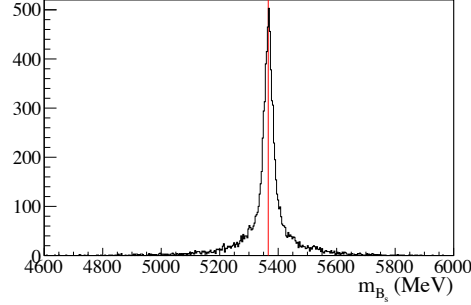


Figure 3.29: Computationally calculated B mass distribution of MC truth matched reconstructed data. The red line indicates the theoretical value of the B mass.

It is possible to fix the mass of the B meson by requiring the relation

$$m_B^2 = (p_\tau + p_\mu)^2 = m_\tau^2 + m_\mu^2 + 2E_\tau E_\mu - 2p_{\tau z} |\vec{p}_\mu| \quad (3.55)$$

to hold. This equation gives another linear relation between  $E_\tau$  and  $p_{\tau x}$ , resulting in a unique solution for the  $\tau$  momentum. However, the B mass can then no longer be used to evaluate any background contributions.

#### 3.5.2 An extra track: $B^+ \rightarrow K^+ \tau^+ \tau^-$

The  $B^+ \rightarrow K^+ \tau^+ \tau^-$  decay is a rare  $B^\pm$  decay that is induced by flavour changing neutral currents (FCNC). This process is forbidden at tree level and must occur via higher order diagrams. It is therefore sensitive to New Physics contributions. In the case of  $b \rightarrow s \ell^+ \ell^-$ , where the lepton is a muon or electron, the neutral Higgs boson effects (NHB) can be neglected. However, in the case of a  $\tau$  lepton, the predicted contributions are sizable. The SM prediction is  $\mathcal{B}(B^+ \rightarrow K^+ \tau^+ \tau^-) \sim 4.3 \cdot 10^{-7}$ . A measured branching fraction higher (or lower) than this would imply New Physics.

Due to the extra track compared to the  $B_s^0 \rightarrow \tau^+ \tau^-$  decay, the B-vertex will no longer lie in the space spanned by the vectors between the primary vertex and the  $\tau$  decay vertices. It is therefore impossible to make this a 2D problem. What is known is that the B-vertex lies along the kaon track. Therefore, by rotating the coordinate system such that the K momentum lies on the  $z$ -axis, the  $x$  and  $y$ -components of the B-vertex are equal to 0.

Although the  $B^+ \rightarrow K^+ \tau^+ \tau^-$  decay mode contains two neutrinos, one from each  $\tau$  particle, it is stronger constrained than the  $B_{(s)}^0 \rightarrow \mu^+ \tau^-$  mode. The known primary and  $\tau$  decay vertices are used to linearly relate the two  $\tau$  momentum components. Including the extra track, the



### Chapter 3. Studies of $\tau$ reconstruction using simulated events

---

relations between the vertices and the momenta are given by

$$d\mathbf{V}_1 - \mathbf{bV} = L_{1\tau} \vec{p}_{1\tau} \quad (3.56)$$

$$d\mathbf{V}_2 - \mathbf{bV} = L_{2\tau} \vec{p}_{2\tau} \quad (3.57)$$

$$\mathbf{pV} - \mathbf{bV} = L_B(\vec{p}_{1\tau} + \vec{p}_{2\tau} + \vec{p}_K) \quad (3.58)$$

Eliminating the scale factors,  $L_{1\tau}$ ,  $L_{2\tau}$  and  $L_B$ , the relations between the different components of the same particle are given to be

$$p_{i\tau y} = \frac{dV_{iy}}{dV_{ix}} p_{i\tau x} = a_i p_{i\tau x} \quad (3.59)$$

with  $i = 1, 2$  for the two  $\tau$  particles. The cross components are proportionally related as

$$p_{2\tau x} = \frac{a_1 \mathbf{pV}_x - \mathbf{pV}_y}{-a_2 \mathbf{pV}_x + \mathbf{pV}_y} p_{1\tau x} = d p_{1\tau x} \quad (3.60)$$

By expressing the  $x$  and  $y$ -components of both  $\tau$  particles solely in terms of  $p_{1\tau x}$ , the  $z$ -component of the scale factor equations gives the relation between the  $p_{1\tau x}$  and the  $z$ -component of the momentum. Using the intermediate step that

$$p_{2\tau z} = \frac{-dV_{1z} + dV_{2z}}{dV_{2x}} d p_{1\tau x} + \frac{dV_{1x}}{dV_{2x}} d p_{1\tau z} = e p_{1\tau x} + f p_{1\tau z} \quad (3.61)$$

is follows that

$$p_{1\tau z} = \frac{(d+1)(\mathbf{pV}_z - dV_{1z}) - \mathbf{pV}_x e}{-(d+1)dV_{1x} + p_{V_x}(f+1)} p_{1\tau x} + \frac{-\mathbf{pV}_x |\vec{p}_K|}{-(d+1)dV_{1x} + p_{V_x}(f+1)} = b_1 p_{1\tau x} + c_1 \quad (3.62)$$

and

$$p_{2\tau z} = (efb_1) p_{1\tau x} + (fc_1) = g p_{1\tau x} + h \quad (3.63)$$

Note that due to the rotation  $p_{Kz} = |\vec{p}_K|$ . Using the available scale factor relations, all momentum components of both  $\tau$  particles are expressed in terms of the single variable  $p_{1\tau x}$ .

Equations 3.1 and 3.2 reduce to a single relation by eliminating the  $E_\tau$  term which occurs in both equations. The unknown variables in the resulting equations are the  $\tau$  momentum components. Each of these components can be written in terms of  $p_{1\tau x}$ . This relation holds for both  $\tau$  particles, and thus results in two quadratic equations in terms of  $p_{1\tau x}$ .

### 3.5. Further event reconstruction possibilities including a $\tau$ lepton

$$\begin{aligned}
0 &= \left[ \left( \frac{p_{13\pi x} + a_1 p_{13\pi y} + b_1 p_{13\pi z}}{E_{13\pi}} \right)^2 - (1 + a_1^2 + b_1^2) \right] p_{1\tau x}^2 \\
&+ \left[ \frac{(m_\tau^2 + m_{13\pi}^2 + 2c_1 p_{13\pi z})(p_{13\pi x} + a_1 p_{13\pi y} + b_1 p_{13\pi z})}{E_{13\pi}^2} - 2b_1 c_1 \right] p_{1\tau x} \\
&+ \left( \frac{m_\tau^2 + m_{13\pi}^2 + 2c_1 p_{13\pi z}}{2E_{13\pi}} \right)^2 - m_\tau^2 - c_1^2 \\
&= r p_{1\tau x}^2 + j p_{1\tau x} + k
\end{aligned} \tag{3.64}$$

and

$$\begin{aligned}
0 &= \left[ \left( \frac{d p_{23\pi x} + a_2 d p_{23\pi y} + g p_{23\pi z}}{E_{23\pi}} \right)^2 - (d^2 + a_2^2 d^2 + g^2) \right] p_{1\tau x}^2 \\
&+ \left[ \frac{(m_\tau^2 + m_{23\pi}^2 + 2h p_{23\pi z})(d p_{23\pi x} + a_2 d p_{23\pi y} + g p_{23\pi z})}{E_{23\pi}^2} - 2gh \right] p_{1\tau x} \\
&+ \left( \frac{m_\tau^2 + m_{23\pi}^2 + 2h p_{23\pi z}}{2E_{23\pi}} \right)^2 - m_\tau^2 - h^2 \\
&= l p_{1\tau x}^2 + s p_{1\tau x} + n
\end{aligned} \tag{3.65}$$

These two equations combined lead to the final expression of

$$p_{1\tau x} = \frac{rn - lk}{lj - rs} \tag{3.66}$$

There is a single possible  $\tau$  momentum solution when using all the information available to rebuild a  $B^+ \rightarrow K^+ \tau^+ \tau^-$  event. In addition, there is always a solution because the final relation is not quadratic. The B mass is not used as a constraint in this procedure and can therefore be used to extract the signal.

Figure 3.30 shows the analytical results on the B mass using (a) generated quantities and (b) reconstructed quantities matched to the MC truth.

The result based on reconstructed data does not show a B mass peak. The calculation assumes the scale factors ( $L_{1\tau}$ ,  $L_{2\tau}$  and  $L_B$ ) to be equal for all momentum components. Although for reconstructed values this must also be true, some components are better measured than others, resulting in different central values and measurement errors. Due to the different central values, this calculation already proves insufficient at Equation 3.59. It is however possible to fit the decay by exploiting its measurement errors and requiring the scale factors to be equal for all momentum components. As measured particles the two  $3\pi$  combinations are available as well as the  $6\pi$ -K combination. In addition, the primary vertex,  $\mathbf{pV}$ , is measured.

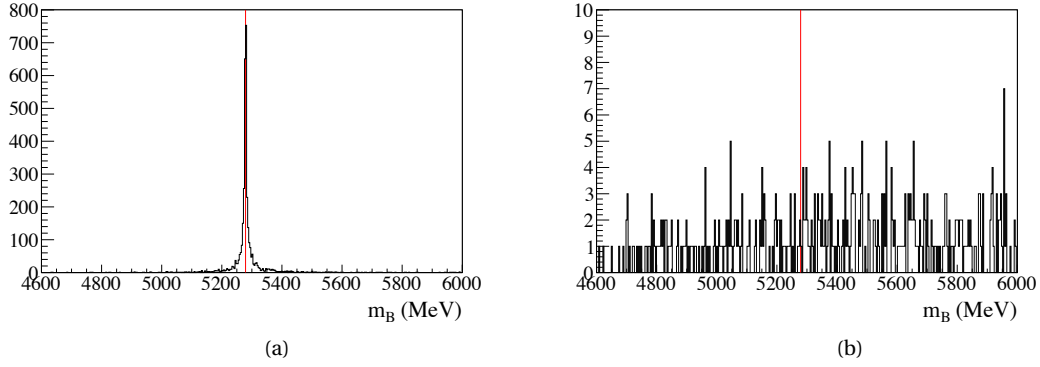


Figure 3.30: Analytically calculated B mass distribution using (a) generated quantities and (b) reconstructed data. The red line indicates the theoretical value of the B mass.

The description of the system thus becomes:

$$h(x) = \{\mathbf{pV}, \mathbf{dV}_1, \vec{p}_{13\pi}, m_{13\pi}^2, \mathbf{dV}_2, \vec{p}_{23\pi}, m_{23\pi}^2, \vec{p}_{6\pi-K}, m_{6\pi-K}^2\} \quad (3.67)$$

The chosen parameters are

$$x = \{\mathbf{pV}, L_{1\tau}, L_{2\tau}, L_B, \vec{p}_{1\tau}, \vec{p}_{1\nu}, \vec{p}_{2\tau}, \vec{p}_{2\nu}, \vec{p}_K\} \quad (3.68)$$

TMinuit is used to fit the decay. 95% of the events were rebuilt with a  $\chi^2 < 10$ . The result of the B mass distribution is shown in Figure 3.31. A clear mass peak is visible, with its mean value consistent with the theoretical B mass.

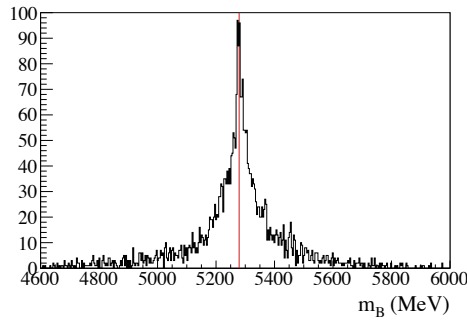


Figure 3.31: Computationally calculated B mass distribution of MC truth matched reconstructed data. The red line indicates the theoretical value of the  $B^\pm$  mass.

The FWHM of the mass peak based on MC data is 4 MeV. After the constrained fit of the decay, the mass width based on reconstructed data is approximately 45 MeV and exhibits large tails.

### 3.5. Further event reconstruction possibilities including a $\tau$ lepton

#### 3.5.3 An extra vertex: $B^0 \rightarrow K^* \tau^+ \tau^-$

The  $B^0 \rightarrow K^* \tau^+ \tau^-$  decay process also occurs through flavour changing neutral currents. This decay is an important candidate among rare B decays, due to its relatively large SM predicted branching fraction which is approximately 3 times the  $B^+ \rightarrow K^+ \tau^+ \tau^-$  branching fraction.

Due to the fact that  $K^* \rightarrow \pi^- K^+$ , the  $K^*$  vertex, which is also the  $\tau$  production vertex, is fully reconstructable. In the  $B^0 \rightarrow K^* \tau^+ \tau^-$  decay a  $\tau$  pair thus originates at a known vertex. Whereas in the reconstruction of the  $Z^0 \rightarrow \tau^+ \tau^-$  decay this resulted in four possible  $\tau$  momentum solutions, the  $B^0 \rightarrow K^* \tau^+ \tau^-$  decays offers extra information in the form of the known direction of the B particle. This extra constraint pins down the correct  $\tau$  momentum solution without the necessity to fix the B to its theoretical mass. In addition, and as shown in the previous section, the final result is not quadratic and therefore a solution is always found.

The relations between the known vertices and the momenta are given by Equations 3.56-3.58, where in this case  $\vec{p}_K = \vec{p}_{K^*}$  represents the momentum of the  $K^*$  particle. In contrast to Section 3.5.2, all  $bV$  components are known.

Separating the first of these relations into components, allows the  $p_{1\tau y}$  and  $p_{1\tau z}$  components to be expressed in terms of  $p_{1\tau x}$  as follows

$$p_{1\tau y} = \frac{dV_{1y} - bV_y}{dV_{1x} - bV_x} p_{1\tau x} = a_1 p_{1\tau x} \quad (3.69)$$

$$p_{1\tau z} = \frac{dV_{1z} - bV_z}{dV_{1x} - bV_x} p_{1\tau x} = b_1 p_{1\tau x} \quad (3.70)$$

Equivalently, for the second  $\tau$  particle, the relations  $p_{2\tau y} = a_2 p_{2\tau x}$  and  $p_{2\tau z} = b_2 p_{2\tau x}$  hold. Using the components of Equation 3.58, the momentum of the second  $\tau$  particle can be expressed in terms of the first particle as

$$p_{2\tau x} = \frac{-(bV_z - pV_z) + b_1(bV_x - pV_x)}{(bV_z - pV_z) - b_2(bV_x - pV_x)} p_{1\tau x} + \frac{(bV_x - pV_x)p_{K^*z} - (bV_z - pV_z)p_{K^*x}}{(bV_z - pV_z) - b_2(bV_x - pV_x)} \quad (3.71)$$

$$= c p_{1\tau x} + d \quad (3.72)$$

Fixing the neutrino and  $\tau$  masses, for each  $\tau$  lepton, Equations 3.1 and 3.2 hold. Combining both relations can eliminate the unknown  $\tau$  energy from the equation. Expressing  $p_{1\tau y}$  and  $p_{1\tau z}$  in terms of  $p_{1\tau x}$  leaves a single quadratic equation, in which  $p_{1\tau x}$  is the only unknown.

$$0 = \left[ \left( \frac{p_{13\pi x} + a_1 p_{13\pi y} + b_1 p_{13\pi z}}{E_{13\pi}} \right)^2 - (1 + a_1^2 + b_1^2) \right] p_{1\tau x}^2 + \frac{(m_\tau^2 + m_{13\pi}^2)(p_{13\pi x} + a_1 p_{13\pi y} + b_1 p_{13\pi z})}{E_{13\pi}^2} p_{1\tau x} + \left( \frac{m_\tau^2 + m_{13\pi}^2}{2E_{13\pi}} \right)^2 - m_\tau^2 \quad (3.73)$$

$$= e_1 p_{1\tau x}^2 + f_1 p_{1\tau x} + g_1 \quad (3.74)$$

### Chapter 3. Studies of $\tau$ reconstruction using simulated events

Equivalently for the second  $\tau$  lepton the relation  $0 = e_2 p_{2\tau x}^2 + f_2 p_{2\tau x} + g_2$  holds. In combination with Equation 3.72, this relation becomes

$$0 = (e_2 c^2) p_{1\tau x}^2 + (2e_2 cd + f_2 c) p_{1\tau x} + e_2 d^2 + f_2 d + g_2 \quad (3.75)$$

Equations 3.74 and 3.75 are quadratic relations, dependent of the single unknown  $p_{1\tau x}$ . Eliminating the quadratic term leaves a single linear relation, which expresses  $p_{1\tau x}$  in terms of known variables as

$$p_{1\tau x} = \frac{e_2 c^2 g_1 - e_1 e_2 d^2 - e_1 f_2 d - e_1 g_2}{2e_1 e_2 cd + e_1 f_2 c - e_2 f_1 c^2} \quad (3.76)$$

The values of the remaining unknowns follow directly from this solution.

The system is overconstrained. As shown in Section 3.5.2, the  $K^*$  vertex is an unnecessary bonus. This fact can however be used to extend the reconstruction by allowing one of the  $\tau$  leptons to decay as  $\tau^- \rightarrow \pi^- \nu_\tau$ . This replaces a known vertex by a track and can also be fully reconstructed.

Figure 3.32 shows the analytical results on the B mass, using (a) generated quantities and (b) reconstructed quantities matching the MC truth.

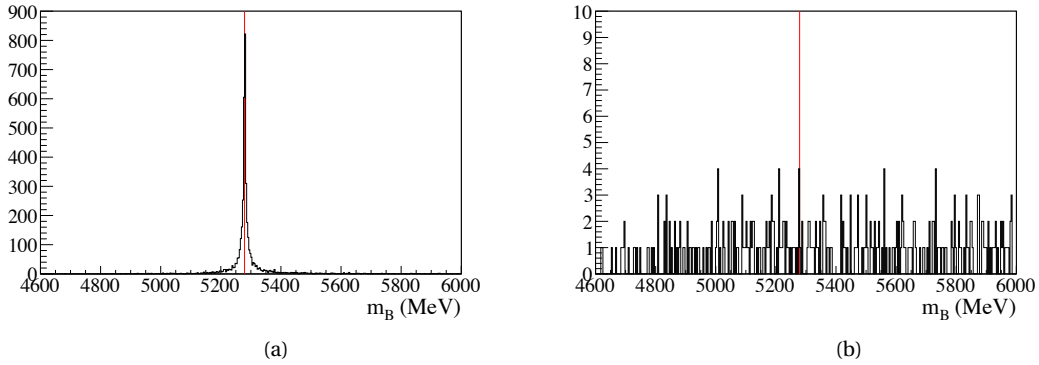


Figure 3.32: Analytically calculated B mass distribution using (a) generated quantities and (b) reconstructed data. The red line indicates the theoretical value of the B mass.

As in the previous section, the mass FWHM of the distribution based on generated quantities is approximately 4 MeV, whereas the calculation based on reconstructed data does not produce a clear signal peak. Therefore a constrained fit is applied with the description of the system given by

$$h(x) = \{\mathbf{pV}, \mathbf{dV}_1, \vec{p}_{13\pi}, m_{13\pi}^2, \mathbf{dV}_2, \vec{p}_{23\pi}, m_{23\pi}^2, \mathbf{bV}, \vec{p}_{K^*}, m_{K^*}^2\} \quad (3.77)$$

### 3.5. Further event reconstruction possibilities including a $\tau$ lepton

Where  $\mathbf{bV}$  is the actual  $K^*$  and thus  $\tau$  production vertex. The chosen parameters are

$$x = \{\mathbf{pV}, L_{1\tau}, L_{2\tau}, L_B, \vec{p}_{1\tau}, \vec{p}_{1\nu}, \vec{p}_{2\tau}, \vec{p}_{2\nu}, \vec{p}_{K^*}, m_{K^*}\} \quad (3.78)$$

The fit was successful for 73% of the events with a  $\chi^2 < 10$  using a TMinuit fit. As there are more constraints available, there is less freedom to find a fitting result. The result of the  $B^0$  mass distribution is shown in Figure 3.33.

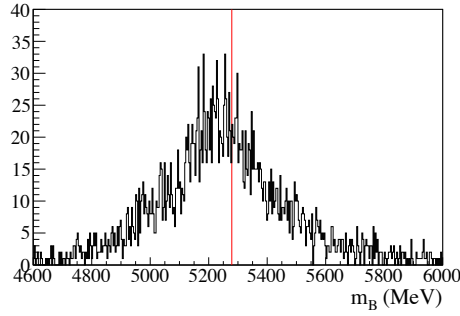


Figure 3.33: Computationally calculated B mass distribution of MC truth matched reconstructed quantities. The red line indicates the theoretical value of the B mass.

The result is reminiscent of the di- $\tau$  mass result from  $Z^0 \rightarrow \tau^+ \tau^-$  decays, as shown in figure 3.12. In both cases the production vertex is fully constrained and the resulting mass peak leans to the low side of the theoretical mass value. The mass FWHM obtained is approximately 200 MeV, which is much more than seen in previous and less constrained reconstructions.

#### 3.5.4 Conclusion

There are many possibilities of event reconstructions that include  $\tau$  leptons. The missing energy caused by the undetected neutrino does not automatically mean that the event cannot be fully or exclusively reconstructed. It is however possible that due to measurement errors, the analytical solution is insufficient and does not produce the required result. In this case, a full constrained fit of the decay in which topological and kinematic relations are forced to be fulfilled within measurement errors, may be a solution. If the decay is not fully constrained, there is a lot of freedom to find a solution which matches all requirements well within measurement errors. However, the more a problem becomes constrained, the less freedom there is within the boundaries. This causes the constrained fit to pull on the established boundaries and to produce inexact results. This phenomenon is demonstrated by the number of events which can be reconstructed within a fit performance value ( $\chi^2 < 10$ ), the improvement on the width of the reconstructed mother mass and its (shifted) mean.

However, less constraints also mean that more a viable solutions will be found in background events that fit the requirements. A full background study is necessary to access the difficulty

### Chapter 3. Studies of $\tau$ reconstruction using simulated events

---

of its suppression and the advantages versus the disadvantages of dealing with a not fully constrained problem. If the reconstructed values are not used to model the decay, the goodness of the fit can still be used as a mean of background suppression. In Chapter 4, the fit  $\chi^2$  is used as a selection cut to suppress background to extract the signal decay of  $B^0 \rightarrow D^{*-} \tau^+ \nu_\tau$ .

## 4 The study of $B^0 \rightarrow D^{*-} \tau^+ \nu_\tau$

In this chapter the exclusive  $\tau$  reconstruction is applied in an attempt to extract the signal decay of  $B^0 \rightarrow D^{*-} \tau^+ \nu_\tau$  from real data. The study is based on  $0.37 \text{ fb}^{-1}$  of 2011 data.

The method of exclusive decay reconstruction is discussed. Following the structure of Chapter 3, the proof of principle and the results which are shown are based on simulation data.

The next step involves the pre-selection of real data candidates. The goal of the pre-selection is to maintain as much of the signal candidates, while discarding the vast majority of combinatoric and physics backgrounds. Once the initial candidates are selected, the full reconstruction of the B and  $\tau$  momenta is performed. The goodness of the constrained fit is used as an offline selection tool. In addition, the candidate selection is improved by requirements that were not applied in the initial pre-selection.

The final selection of candidates consists of signal, physics background and combinatoric candidates. The distribution of the  $3\pi$  invariant mass is used to distinguish between real  $\tau$  candidates and fake ones. After the data is corrected for the combinatoric background, the real  $D^*$  candidates are selected and a model of the  $3\pi$  invariant mass is created. This model is solely based on the simulation models of the signal and the physics background components.

### 4.1 Final state reconstruction

The reconstruction of the  $B^0 \rightarrow D^{*-} \tau^+ \nu_\tau$  decay is complicated by the presence of neutrinos. In Chapter 3 the reconstruction method of different decays including one or two  $\tau$  leptons was discussed. The  $B^0 \rightarrow D^{*-} \tau^+ \nu_\tau$  decay can be rebuilt in a similar manner. Despite fixing the B mass to its established value, there are up to four possible  $\tau$  momentum solutions due to the fact that there are two neutrinos in the decay.

Because one of the neutrinos originates from the B particle, it is not possible to linearly relate the  $\tau$  momentum to the B momentum. The decay channel can be separated into two equivalent parts.



#### Chapter 4. The study of $B^0 \rightarrow D^{*-} \tau^+ \nu_\tau$

- The decay  $\tau^+ \rightarrow (\pi^+ \pi^+ \pi^-) \bar{\nu}_\tau$  from a known vertex
- The decay  $B^0 \rightarrow (D^{*-} \tau^+) \nu_\tau$  from a known vertex

The brackets are used to indicate the part of the decay which is directly measurable. The first of these can be reconstructed as described in Section 3.2. The result gives two valid  $\tau$  momentum solutions. For each reconstructed  $\tau$  momentum, the  $B^0 \rightarrow (D^{*-} \tau^+) \nu_\tau$  then equivalently has two B momentum solutions. This means that there are four solutions in general. However, when the calculated invariant mass of one of the  $D^*$  and  $\tau$  combinations exceeds the B mass, the number of solutions is reduced to two. A schematic representation of the decay chain is given in Figure 4.1.

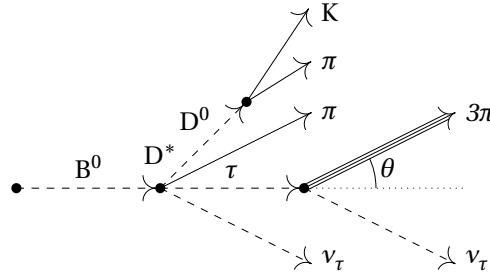


Figure 4.1: A schematic representation of  $B^0 \rightarrow D^{*-} \tau^+ \nu_\tau$  with  $D^{*-} \rightarrow \pi^- (\bar{D}^0 \rightarrow K^+ \pi^-)$  and  $\tau^+ \rightarrow \pi^+ \pi^+ \pi^- \bar{\nu}_\tau$ .

There is a large error on the  $D^*$  vertex measurement, due to the slow pion (low transverse momentum) coming from its decay. Good vertex reconstruction accuracy is important to allow the analytical calculation of the  $\tau$  and B momenta. Before any selection the reconstruction efficiency is approximately 9%.

This efficiency can be improved by performing a constrained fit on the decay, as described in Section 3.2.3. The complete decay chain is fitted simultaneously, with the advantage that the  $D^*$  vertex is constrained as the B decay vertex as well as the  $\tau$  production vertex. The description of the system is given by

$$h(x) = \{\mathbf{pV}, \mathbf{dV}, \vec{p}_{3\pi}, m_{3\pi}^2, \mathbf{bV}, \vec{p}_{D^*}, m_{D^*}^2\} \quad (4.1)$$

The chosen parameters are

$$x = \{\mathbf{pV}, \vec{p}_\tau, \vec{p}_{1\nu_\tau}, L, \vec{p}_B, \vec{p}_{2\nu_\tau}, L_B\} \quad (4.2)$$

Here the momentum of the  $\tau$ -neutrino that originated from the  $\tau$  particle is denoted by  $p_{\nu_\tau}$ , whereas the momentum of the  $\tau$ -neutrino that originated from the B particle is denoted by  $p_{2\nu_\tau}$ . The  $\tau$  mass is fixed through the determination of the  $m_{3\pi}$  value described by Equation

3.10. The calculation of the  $D^*$  mass is used to fix the B mass to its established value as

$$m_{D^*}^2 = m_B^2 + m_\tau^2 - 2(E_B E_\tau + E_B E_{2\nu_\tau} - E_\tau E_{2\nu_\tau}) + 2(\vec{p}_B \cdot \vec{p}_\tau + \vec{p}_B \cdot \vec{p}_{2\nu_\tau} - \vec{p}_\tau \cdot \vec{p}_{2\nu_\tau}) \quad (4.3)$$

with

$$E_{2\nu_\tau} = |\vec{p}_{2\nu_\tau}| \text{ and } E_B = \sqrt{m_B^2 + |\vec{p}_B|^2} \quad (4.4)$$

The parameters that describe the system with the smallest error are selected. Using the fitted values, the multiple solutions for the  $\tau$  and B momenta are calculated.

In this section, the results of the decay reconstruction are demonstrated using simulated signal data. The decay time distribution from the obtained result is shown in Figure 4.2(a). The distribution peaks significantly close to zero decay time. The decay time values for which the distance between vertices is smaller than 0.07 mm are shown in red. This is similar to the fitted  $\tau$  decay time from the  $B_s^0 \rightarrow \tau^+ \tau^-$  decay, as depicted in Figure 3.27. However, when solely considering the reconstructed  $\tau$  momentum values, the  $p_\tau$  asymmetry as defined in Equation 3.5, does not exhibit the same behaviour. The momentum asymmetries of those decays where the distance between vertices is small are of the same magnitude as the others, as shown in Figure 4.2(b).

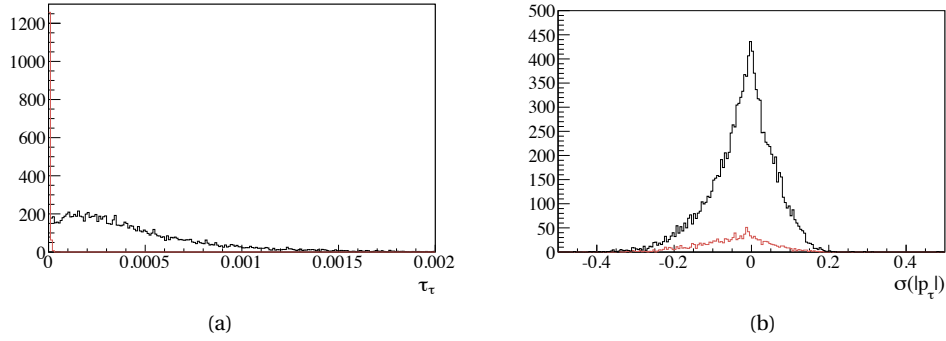


Figure 4.2: (a) The decay time distribution and (b)  $p_\tau$  asymmetry distribution of reconstructed  $\tau$  particles, which best match the MC truth value for  $|\mathbf{dV} - \mathbf{bV}| < 0.07$  mm in red and  $|\mathbf{dV} - \mathbf{bV}| > 0.07$  mm in black.

It is possible to use the reconstructed  $\tau$  momentum and the measured vertices (not obtained by the decay fit) to determine a decay time distribution. The result is shown in Figure 4.3(a). A negative component of the decay time is obtained. In addition, the average decay time is much larger than the known  $\tau$  decay time. This is due to the fact that the average measured distance between vertices is larger than the generated distances, as shown in Figure 4.3(b).

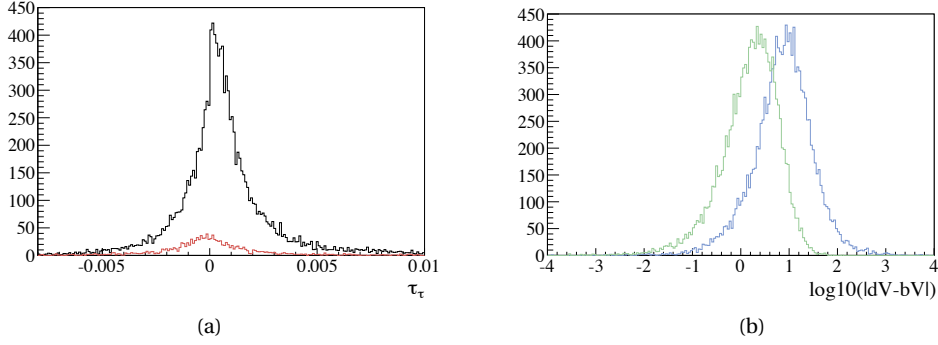


Figure 4.3: (a) The decay time distribution of reconstructed  $\tau$  particles, which best match the MC truth value for  $|\mathbf{dV} - \mathbf{bV}| < 0.07$  mm in red and  $|\mathbf{dV} - \mathbf{bV}| > 0.07$  mm in black, based on the measured vertices and (b) the  $\log_{10}(|\mathbf{dV} - \mathbf{bV}|)$  distribution of the measured vertices in blue and generated vertices in green.

## 4.2 Event pre-selection

At LHCb, after successfully passing the trigger, events of interest are collected and partially reconstructed for further processing. Each physics channel is analysed with its own pre-selection algorithms, called stripping lines. If an event has been selected by a stripping line, it is fully re-reconstructed and written to the stripping line specific output location.

As the  $B^0 \rightarrow D^{*-} \tau^+ \nu_\tau$  decay channel had not been studied before, a new dedicated stripping line was created and named '*Bd2DstarTauNu*'. The study performed in this thesis is based on  $0.37 \text{ fb}^{-1}$  of 2011 data, which corresponds to stripping version 13b. The performance of each stripping line is tested by its retention rate and its CPU timing. The required figures are a retention rate less than 0.05% within 0.5 ms per event.

The '*Bd2DstarTauNu*' stripping line selects  $D^{*\mp} \tau^\pm$  combinations, as well as same-sign  $D^{*\pm} \tau^\pm$  pairs. The reconstructed right-sign (RS)  $D^{*\mp} \tau^\pm$  combinations includes the signal decay mode as well as physics backgrounds. The reconstruction of same-sign or wrong-sign (WS)  $D^{*\pm} \tau^\pm$  pairs is included to study the shape and number of the combinatoric background. The different background components considered in this analysis are described in Section 4.4.

In order to reconstruct a  $B^0 \rightarrow D^{*-} \tau^+ \nu_\tau$  decay, six hadrons need to be combined. With an abundance of pions and kaons in the detector, this can be a time consuming task. To speed up the process,  $D^*$  particle candidates made with loose requirements are selected. The additional cuts on the  $D^*$  particle are chosen to coincide with the cuts used in the  $B^0 \rightarrow D^{*-} \mu^+ \nu_\mu$  stripping line. Although not subject of this thesis, this is a convenient choice for the possible normalisation to the semi-muonic decay. The application of the cuts on the  $D^*$  meson eliminates 98.5% of events before the reconstruction of the  $\tau$  particle is performed.

The cuts on the individual pions considered for the  $\tau$  reconstruction significantly reduce the

combinatorics involved in the  $\tau$  creation process. The reconstruction of the  $\tau$  particle is split into two steps, as it is significantly faster to combine two particles than it is to combine three. First a di- $\pi$  particle is created. This pion pair is subject to the strongest cuts to reduce the number of possibilities. It is found that the mass of the di- $\pi$  combination with the highest mass is highly correlated to the  $3\pi$  mass. It is therefore possible to apply a strong cut in order to reduce the background while maintaining the signal events. The di- $\pi$  mass cut chosen is  $750 \text{ MeV} < m_{2\pi} < 1500 \text{ MeV}$ . Approximately 18% of the events are excluded by the cuts on the di- $\pi$  combination. An additional cut of  $1200 \text{ MeV} < m_{3\pi} < 1780 \text{ MeV}$  is made on the  $3\pi$  mass. Figure 4.4 depicts the combined mass distributions and indicates the area of selected values. Applying the  $3\pi$  combination cuts, a further 44% of the events is excluded. The final cuts on the creation of the B particle exclude a final 90%.

The complete set of selection cuts is given in Section 4.2.1. This method of reconstruction allows the same three pions to be selected in different order to form an identical  $3\pi$  combination. However, during the offline selection only one  $3\pi$  combination is selected per event which is described in Section 4.3

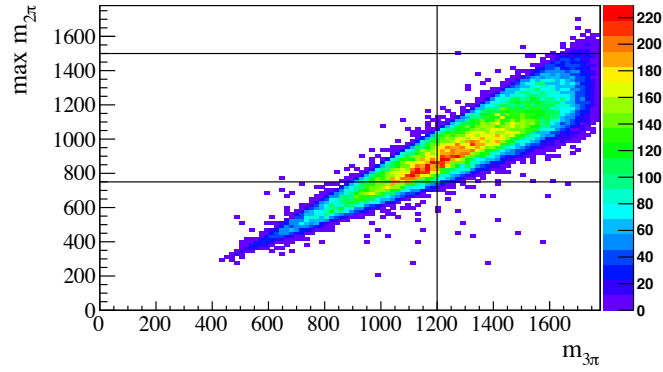


Figure 4.4: MC distribution of the maximum di- $\pi$  mass as a function of the  $3\pi$  mass. Black lines enclose the selected values in Stripping 13b.

Even though the signal decay channel suffers from missing energy, the cut on the reconstructed B mass is chosen above its nominal value. This allows the possibility to normalise the measured signal to the  $B^0 \rightarrow D^{*-} \pi^- \pi^+ \pi^+$  decay mode. This channel has the exact same final state as the signal mode, but is fully reconstructable. To allow for its selection in the same stripping line simplifies its normalisation, as the effect of different selection cuts is nullified.

#### 4.2.1 Stripping Cuts

The pre-selection cuts performed in the '*Bd2DstarTauNu*' stripping line with the aim to select  $B^0 \rightarrow D^{*-} \tau^+ \nu_\tau$  events are given in Table 4.1. The  $D^*$  particle is required to decay through the  $D^{*-} \rightarrow (\bar{D}^0 \rightarrow K^+ \pi^-) \pi^-$  mode. The  $\pi$  particle originating from the  $D^*$  meson is referred to as the slow pion.

## Chapter 4. The study of $B^0 \rightarrow D^{*-} \tau^+ \nu_\tau$

$\tau$ stripping cuts		$D^*$ stripping cuts	
pion parameters		Kaon parameters	
$p_T$	> 150 MeV	$p_T$	> 350 MeV
min IP $\chi^2$	> 4	long track	true
track $\chi^2/\text{dof}$	< 5	track $\chi^2/\text{dof}$	< 8
PIDK	< 8	min IP	> 0.04 mm
di-pion parameters		min IP $\chi^2$	> 4
$p_T$	> 600 MeV	PIDK	> -5
$m$	> 750 MeV	pion parameters	
$m$	< 1500 MeV	$p_T$	> 350 MeV
vertex $\chi^2/\text{dof}$	< 9	long track	true
DIRA	> 0.99	track $\chi^2/\text{dof}$	< 8
min IP $\chi^2$	> 5	min IP	> 0.04 mm
min IP $\chi^2$ for $\pi_1$ or $\pi_2$	> 20	min IP $\chi^2$	> 4
$\tau$ -resonance parameters		$D^0$ -resonance parameters	
$p_T$	> 800 MeV	$p_T$	> 1600 MeV
$m$	> 1200 MeV	$ m - m_{D^0} $	< 40 MeV
$m$	< 1780 MeV	$(D^0 \text{ vertex} - \text{PV})\chi^2$	> 50
vertex $\chi^2/\text{dof}$	< 9	vertex $\chi^2/\text{dof}$	< 10
DIRA	> 0.99	Slow pion parameters	
min IP $\chi^2$	> 5	$p_T$	> 110 MeV
$B^0$ stripping cuts		long track	true
$B^0$ -resonance parameters		track $\chi^2/\text{dof}$	< 8
$m - m_{B^0}$	> -1279 MeV	min IP	> 0.04 mm
$m - m_{B^0}$	< 300 MeV	$D^*$ -resonance parameters	
DIRA	> 0.99	vertex $\chi^2/\text{dof}$	< 20
$(\tau \text{ vertex} - D^* \text{ vertex})$	> -3.0 mm	$m - m_{D^0}$	< 160 MeV
$(D^0 \text{ vertex} - B^0 \text{ vertex})_z$	> -3.0 mm	$p_T$	> 1250 MeV
$(B^0 \text{ vertex} - \text{PV})_z$	> -5.0 mm	$ m - m_{D^*} $	< 50 MeV

Table 4.1: Cuts made in the designated 'Bd2DstarTauNu' stripping line with the aim to select  $B^0 \rightarrow D^{*-} \tau^+ \nu_\tau$  events.

The variables used to discriminate between signal and background are defined as

- $p_T$ : the transverse energy of a reconstructed particle.
- $m$ : the measured mass of a combined particle.
- $m_A$ : the theoretical mass of particle  $A$ .
- vertex  $\chi^2/\text{dof}$ : the  $\chi^2$  of the fit to the decay vertex of a reconstructed particle divided by the number of degrees of freedom.
- track  $\chi^2/\text{dof}$ : the  $\chi^2$  of the fit of a reconstructed track divided by the number of degrees of freedom.

- (A vertex - B vertex): the signed distance between the decay vertices of particles A and B. One of the vertices can also relate to the primary vertex, denoted by PV.
- (A vertex - PV)  $\chi^2$ : gives the  $\chi^2$  of the fit to the vertex of particle A assuming it coincides with the primary vertex.
- min IP: the minimum distance of a particle's trajectory to each reconstructed primary vertex.
- min IP  $\chi^2$ : returns the minimum  $\chi^2$  distance of a particles' trajectory to each reconstructed primary vertex.
- DIRA: the cosine of the angle between the reconstructed momentum of a particle and its reconstructed flight direction, based on the best matching primary vertex as its production vertex.
- long track: a track that is reconstructed from hits in the VELO and the TT as well as the IT or OT.
- PIDK: the delta-log-likelihood for the kaon PID hypothesis with respect to the pion, given by  $\Delta \log \mathcal{L}_{K-\pi}$ .

#### 4.2.2 Results

A stripping line with a retention rate of 0.0456 within 0.576 ms per event is obtained and approved. The rate corresponds to 21 accepted reconstructed particles in 50,000 events. No slow events are flagged.

Determined from simulation, the reconstruction efficiency of the  $B^0 \rightarrow D^{*-} \tau^+ \nu_\tau$  decay is approximately 6.7%. Of these reconstructable candidates, 0.9% pass the strong pre-selection cuts, resulting in a total efficiency of 0.06%.

After applying the stripping cuts, only 2.9% of all selected signal candidates can be reconstructed analytically. This shows the importance of the constrained fit to include more candidates.

### 4.3 Offline selection

For the selection of the signal decay, the invariant mass is of the combined  $D^*$  and  $3\pi$  system is cut at  $m_{D^*+3\pi} < 5000$  MeV.

#### 4.3.1 The value of $\chi^2$ as a selection cut

Despite the strong pre-selection cuts, more than one B candidate can be selected in each event. The  $\chi^2$  value of the constrained fit is chosen to quantify the goodness of the candidates.

The candidate with the lowest  $\chi^2$  value per event is selected, while all others are discarded.

As much as 91% of the selected candidates exhibit a  $\chi^2$  value smaller than 10. The cut  $\chi^2 < 10$  thus maintains most of the signal events. Only 16% of candidates reconstructed from real data are kept after the cut on the  $\chi^2$ .

Figure 4.5 shows the  $\log_{10}(\chi^2)$  distributions of the simulated signal and the reconstructed candidates in real data.

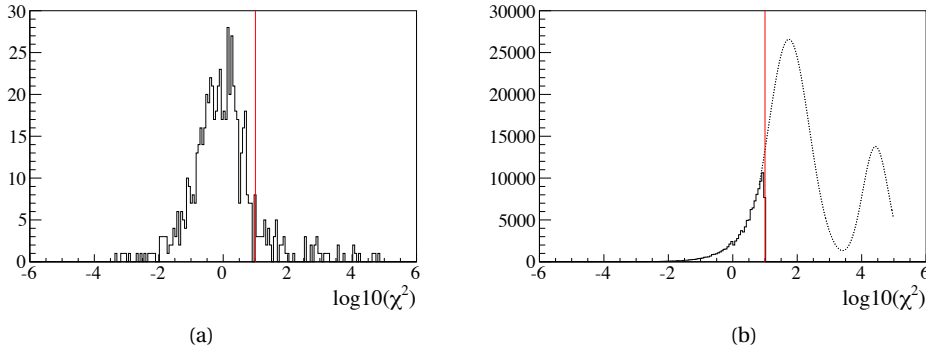


Figure 4.5: The  $\log_{10}(\chi^2)$  distributions corresponding to the performance of the decay fit of (a) the MC signal decay  $B^0 \rightarrow D^{*-} \tau^+ \nu_\tau$  and (b) real data combinations. The dotted line represents the shape of the  $\chi^2$  distribution for  $\chi^2 > 10$ . The red line indicates the applied offline selection cut.

### 4.3.2 Tuning of the selection criteria

Due to the strong selection cuts needed for a six-particle hadronic decay to satisfy the stripping requirements and due to the strong selection cut provided by the constrained fit  $\chi^2$ , only little additional background rejection is required. Four additional cuts are implemented which lead to the final selected data set. For each of these cuts, the given efficiency is determined independently of the other three cuts.

- $m_{D^*+\tau} < 5000 \text{ MeV}$ : In the decay fit the mass of the B meson is fixed. As all decays must satisfy this requirement, the invariant mass of the  $D^*$  plus  $\tau$  system must be smaller than the fixed B mass. In the case that this is not a favorable solution, the invariant mass is forced to its maximum allowed value. This effect is shown in Figure 4.6. A hard cut is made on the invariant mass to, in addition, eliminate all fully reconstructable background. The chosen cut keeps 91% of signal candidates, whereas it keeps 79% of real data candidates.
- $vertex \chi^2/dof < 2$ : The value of the  $3\pi$  vertex  $\chi^2/dof$  was already required to be smaller than 9 by the online stripping selection. However, as shown in Figure 4.7 this cut can be

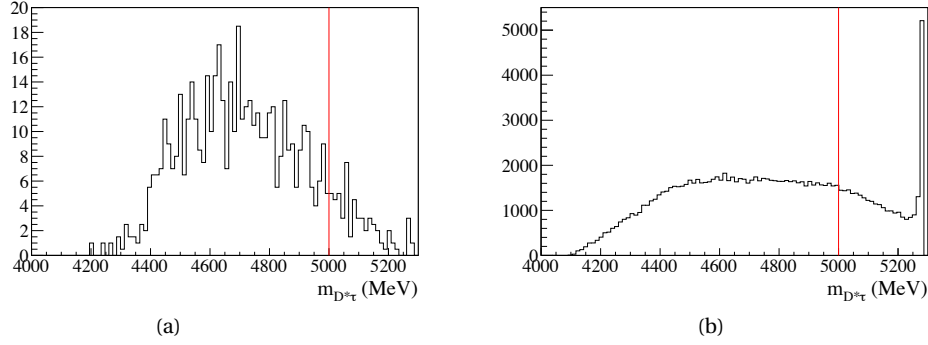


Figure 4.6: The invariant  $D^* \tau$  mass distributions of (a) MC signal and (b) real data candidates. The red line depicts the chosen cut value.

tightened in order to reduce the background significantly, while a large fraction of signal candidates is kept. Requiring the vertex  $\chi^2/\text{dof}$  to be smaller than 2 keeps 76% of the signal candidates. The real data candidates are reduced to 27%.

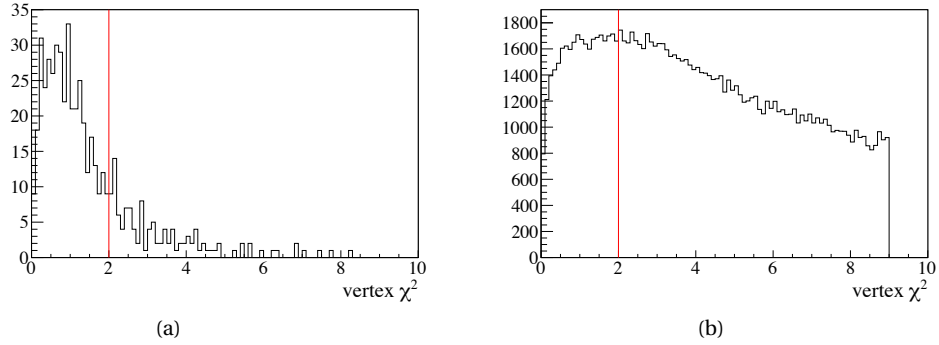


Figure 4.7: The  $3\pi$  vertex  $\chi^2/\text{dof}$  distributions of (a) MC signal and (b) real data candidates. The red line depicts the chosen cut value.

- *isolation* > 1.5: The isolation cut requires the three pions to be the only particles coming from the same vertex. For all other particles in the event, the value of the vertex  $\chi^2$  is considered when this particle plus the reconstructed  $3\pi$  particle are combined to originate from one vertex. This new value, denoted by vertex  $\chi_i^2$ , must be large for all particles to ensure no other track originated from the  $3\pi$  vertex. The isolation cut is defined as the minimum value of  $\log_{10}(\text{vertex } \chi_i^2 - \chi^2)$ , where  $i = 1 \dots \text{number of particles}$ . This cut selects 85% percent of the signal candidates and 79% of the real data candidates, as is depicted in Figure 4.8.
- *PIDK* < -6: The strongest cut is applied on the PIDK value of the three pions coming from the  $\tau$  particle. Each pion has to have a PIDK value smaller than -6. This strong



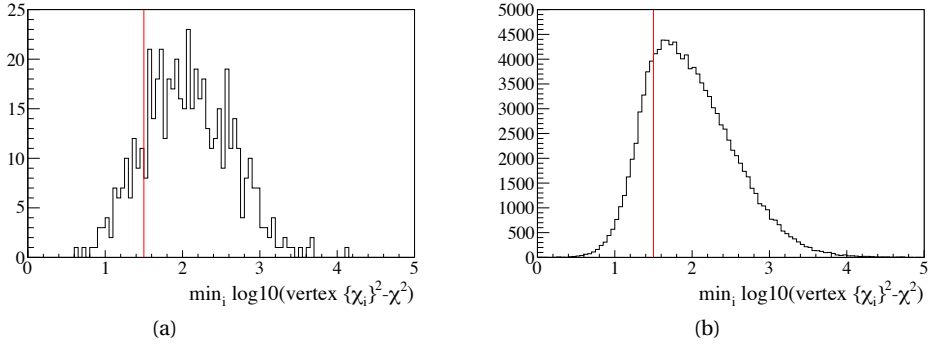


Figure 4.8: The distribution of the  $\min_i \log_{10}(\text{vertex } \chi_i^2 - \chi^2)$  vertex isolation value, where  $i = 1 \dots$  number of particles for (a) MC signal and (b) real data candidates. The red line depicts the chosen cut value.

cut is needed to eliminated kaonic backgrounds. Although this cut only selects 53% of signal events, it efficiently reduces the real data candidates to 6%.

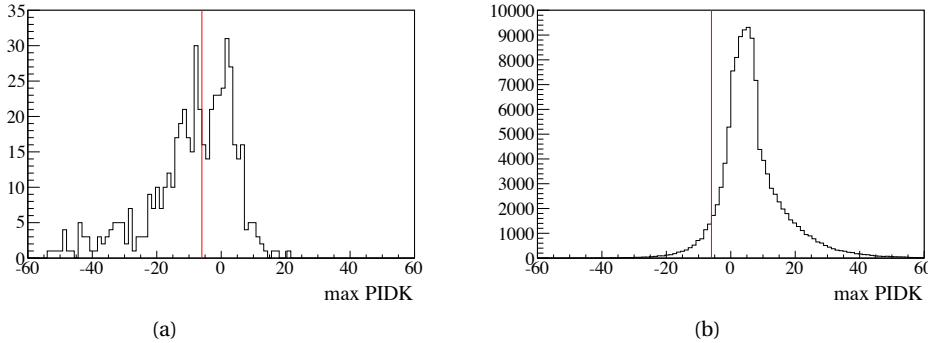


Figure 4.9: The distribution of the maximum PIDK value of the pions from the reconstructed  $3\pi$  particle for (a) MC signal and (b) real data candidates. The red line depicts the chosen cut value.

### 4.3.3 Results

The simulated signal is reconstructed with a total efficiency of 0.0145%. The  $m_{D^*} - m_{D^0}$  and  $m_{3\pi}$  signal distributions are shown in Figure 4.10. These distributions are chosen for their distinguishable signal and background shapes. The first is used to extract real  $D^*$  particles, whereas the  $3\pi$  invariant mass distribution is used to extract real  $\tau$  leptons. The  $m_{3\pi}$  shape is modeled using a RooKeysPdf which is a one-dimensional kernel estimation model based on the superposition of Gaussian kernels [43]. A Gaussian shape is used to represent the  $m_{D^*} - m_{D^0}$  distribution for demonstration purposes. The  $m_{3\pi}$  distribution is independent of

the constrained fit, which is only used as an effective selection tool.

The  $0.37 \text{ fb}^{-1}$  data set is reduced to 3517 events. Figure 4.11 shows clear background components in both the  $m_{D^* - m_{D^0}}$  and  $m_{3\pi}$  distributions. In Section 4.4 different background contributions are considered to explain the shape of the data distributions.

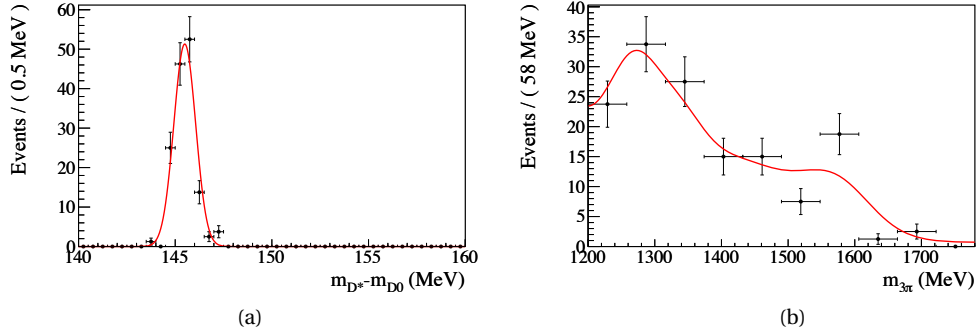


Figure 4.10: The simulated (a)  $m_{D^* - m_{D^0}}$  and (b)  $m_{3\pi}$  distributions belonging to the real  $D^*$  and  $\tau$  particles from the signal decay after all selection cuts are applied. A fixed Gaussian shape is used to represent the  $m_{D^* - m_{D^0}}$  signal shape, whereas the  $m_{3\pi}$  distribution is modeled using a RooKeysPdf.

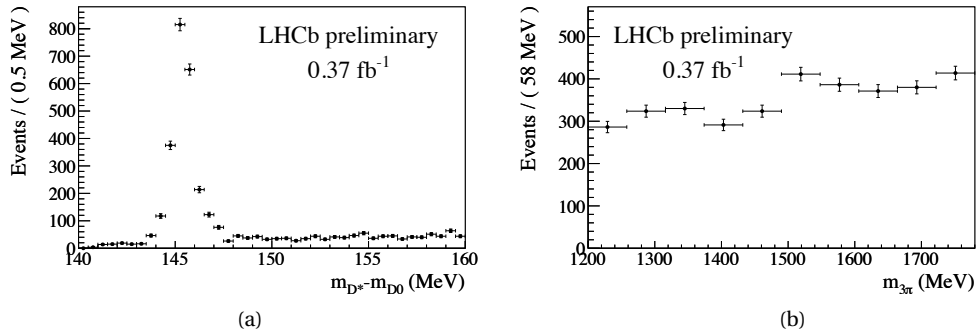


Figure 4.11: The (a)  $m_{D^* - m_{D^0}}$  and (b)  $m_{3\pi}$  distributions obtained from real data after the complete selection process.

As shown in Section 4.3.2, strong offline cuts were made on the pion PID values and the  $3\pi$  vertex  $\chi^2$ . The  $m_{3\pi}$  distribution is chosen to model and extract the signal  $\tau$  leptons, but this distribution suffers from strong cuts at stripping level. It is feasible that the selection can be improved by stronger online PID and vertex cuts in favour of a lower  $m_{3\pi}$  cut.

#### 4.4 Background contributions

Contributions from combinatoric and physics backgrounds are considered. The number of combinatoric events and their shapes are determined by selecting  $D^{*\pm} \tau^{\pm}$  events. As the combined particles have the same charge these are physically impossible combinations when reconstructing a B particle and are therefore addressed as wrong-sign (WS) combinations. These combinations do not come from one decay chain and are therefore considered combinatoric background. The obtained distributions are depicted in Figure 4.12.

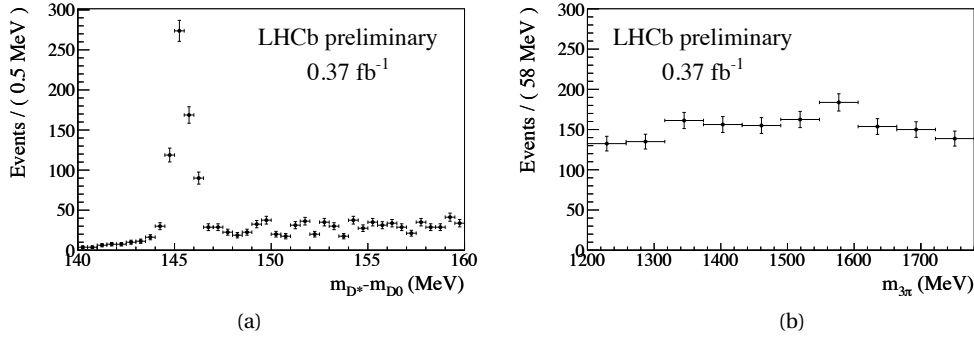


Figure 4.12: The (a)  $m_{D^*} - m_{D^0}$  and (b)  $m_{3\pi}$  distributions obtained from WS combinatoric background that has passed all selection cuts.

The considered physics background contributions can be split into four categories:

- *Decays with a real  $D^*$  particle, but no  $\tau$  particle:* The inclusive MC samples of  $B_d \rightarrow DX$ ,  $B_u \rightarrow DX$ ,  $B_s \rightarrow DX$  and  $\Lambda_b \rightarrow DX$  decays are considered as potential background contributions. These samples do not include  $\tau$  leptons and the signal decay is therefore not included. Due to an incomplete decay description, the contribution of the  $B^0 \rightarrow D^* \pi \pi \pi^0$  decay is considered separately.
- *Decays with no  $D^*$  particle, but with a real  $\tau$  particle:* Candidates from the exclusive decays of  $B^0 \rightarrow D^0 \pi^- \tau^+ \nu_{\tau}$  and  $B^0 \rightarrow D^- \tau^+ \nu_{\tau}$ , with  $D^- \rightarrow K^- \pi^- \pi^+$  are considered the most likely background contributions.
- *Decays with no  $D^*$  particle and with no  $\tau$  particle:* As no  $\tau$  is present, the inclusive  $B \rightarrow DX$  samples also cover the fake  $D^*$  and fake  $\tau$  candidates.
- *Decays with a real  $D^*$  particle and a real  $\tau$  particle:* If the real  $\tau$  particle does not originate from the B particle, the decay is considered background. The main contributor is thought to be  $B^0 \rightarrow D^{*-} D_s^{(*)+}$  with  $D_s^+ \rightarrow \tau^+ \nu_{\tau}$ . This decay has exactly the same final state as the signal decay. Decay chains in which the  $\tau$  lepton decays into three pions, a neutrino and additional neutral particles is also considered a main background source.

The distributions of all physics background models are based on MC information. For the inclusive  $B_d \rightarrow DX$  and  $B_u \rightarrow DX$  decays, MC samples of 40M events are used. The  $B_s \rightarrow DX$  and  $\Lambda_b \rightarrow DX$  decays are modeled based on a 10M event sample each. To model the exclusive contributions, a sample of 1M events is used for each decay.

The main background source of fake  $\tau$  leptons is found to come from inclusive  $b \rightarrow cX$  events. The obtained  $m_{D^*} - m_{D^0}$  and  $m_{3\pi}$  distribution shapes from the main components are depicted in Figure 4.13. The background sources of  $B_s \rightarrow DX$  and  $\Lambda_b \rightarrow DX$  are neglected, as the number of candidates that pass all selection cuts is not sufficient to create a model and their contribution is small compared to that of their  $B_d \rightarrow DX$  and  $B_u \rightarrow DX$  counterparts. The contribution of the  $B^0 \rightarrow D^{*-}\pi^-\pi^+\pi^0$  decay mode is considered individually, however it is technically part of the  $B_d \rightarrow DX$  contribution.

Of the considered fake  $D^*$  sources of  $B^0 \rightarrow D^0\pi^-\tau^+\nu_\tau$  and  $B^0 \rightarrow D^-\tau^+\nu_\tau$  only a couple of events pass the selection. As these are not sufficient to base a model upon and as their branching fractions are not exceptionally large, these background contributions are neglected.

The second main background contribution comes from a source of real  $D^*$  mesons and real  $\tau$  lepton. The decay of  $B^0 \rightarrow D^{*-}D_s^{(*)+}$  with  $D_s^+ \rightarrow \tau^+\nu_\tau$  has exactly the same final state as the signal decay and due to the elongated  $D_s$  plus  $\tau$  lifetime, its trigger efficiency is higher. Besides those decays in which  $\tau^+ \rightarrow \pi^+\pi^+\pi^-\bar{\nu}_\tau$  which is the required mode by the constrained fit,  $\tau$  lepton decays with extra missing energy are also considered. The real  $\tau$  background contributions are depicted in Figure 4.14. Interestingly, the decay chains with an extra neutral pion have a higher total selection efficiency. Although the selection cuts are based on a single missing neutrino, the  $B^0 \rightarrow D^{*-}\tau^+\nu_\tau$  decay with  $\tau^+ \rightarrow \pi^+\pi^+\pi^-\bar{\nu}_\tau\pi^0$  arguably also classifies as signal  $B^0 \rightarrow D^{*-}\tau^+\nu_\tau$  and both come from a real  $\tau$  source.

## 4.5 Signal extraction

In order to extract the signal, the combinatoric background is treated first. Under the assumption that the number of combinatoric candidates is the same for the WS and RS combinations, the  $m_{D^*} - m_{D^0}$  and  $m_{3\pi}$  distributions of the WS candidates are subtracted from the RS data distributions. The subtraction is performed by adding the two data sets while assigning negative weights to the values of the WS candidates. The resulting distributions are depicted in Figure 4.15.

As depicted in Section 4.4, any fake  $D^*$  combination is highly suppressed in the physics backgrounds. It is therefore chosen not to model this background component, but to use a RooFit SPlot [44] in order to extract the  $m_{D^*} - m_{D^0}$  signal component. The SPlot technique unfolds distributions of different sources based on a likelihood fit. The  $m_{D^*} - m_{D^0}$  data distribution is fitted with a double Gaussian to represent the real  $D^*$  particles. The predefined RooDstD0BG distribution shape is used to model the fake  $D^*$  particles. In figure 4.16 these signal and background distributions are depicted. The fake  $D^*$  particle component is shown

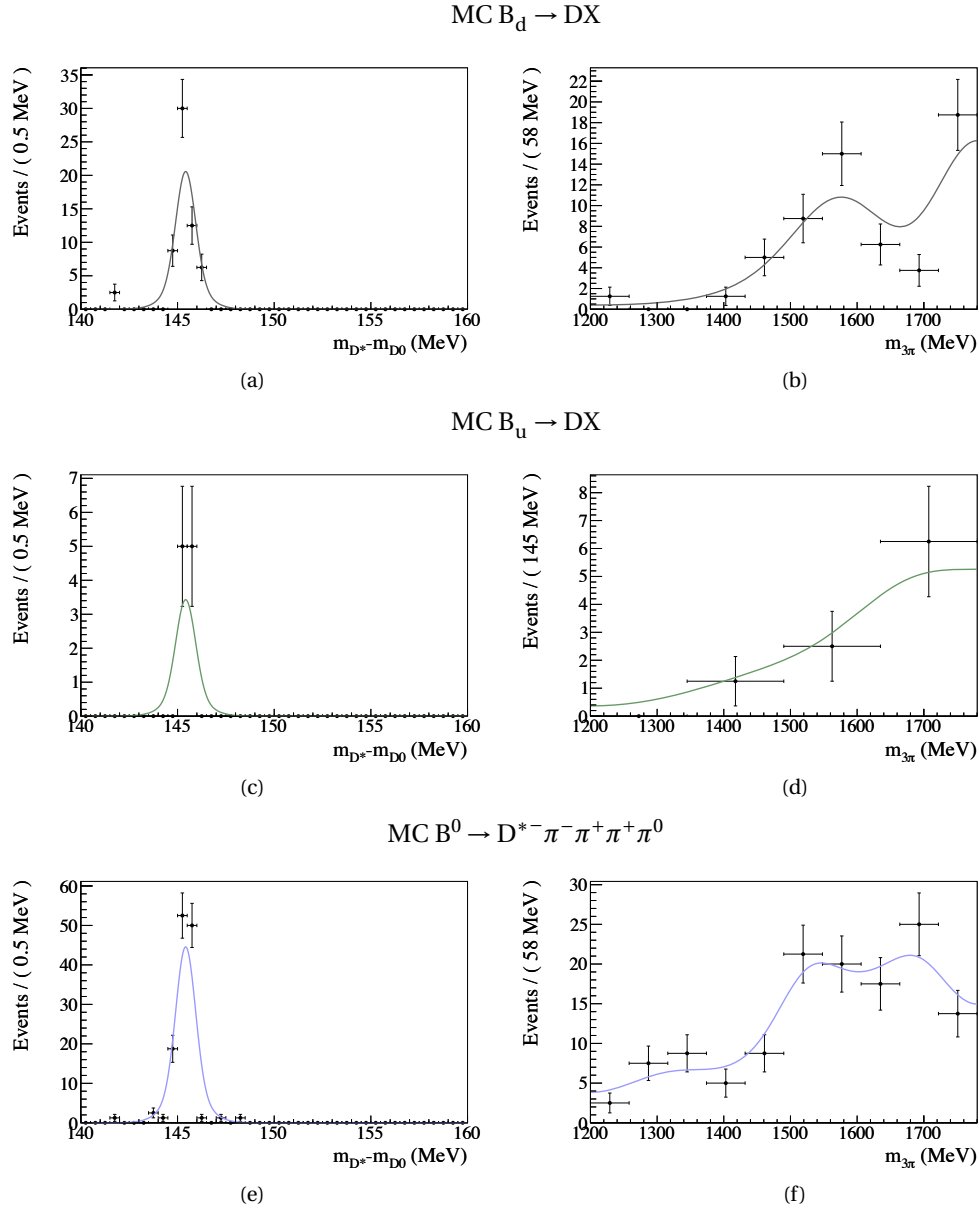


Figure 4.13: The (left)  $m_{D^*} - m_{D^0}$  and (right)  $m_{3\pi}$  distributions from the (top) MC  $B_d \rightarrow DX$ , (middle) MC  $B_u \rightarrow DX$  and (bottom) MC  $B^0 \rightarrow D^{*-} \pi^- \pi^+ \pi^+ \pi^0$  samples after all selection cuts are applied. A fixed Gaussian shape is used to represent the  $m_{D^*} - m_{D^0}$  signal shape, whereas the  $m_{3\pi}$  distribution is modeled using a RooKeysPdf.

with a dashed line.

By reweighing the data set with SPlot weights, the  $m_{3\pi}$  distribution that corresponds to the real  $D^*$  particles is singled out. In order for this to work the two distributions must be uncorrelated. The resulting  $3\pi$  invariant mass distribution is shown in Figure 4.17. These remaining events

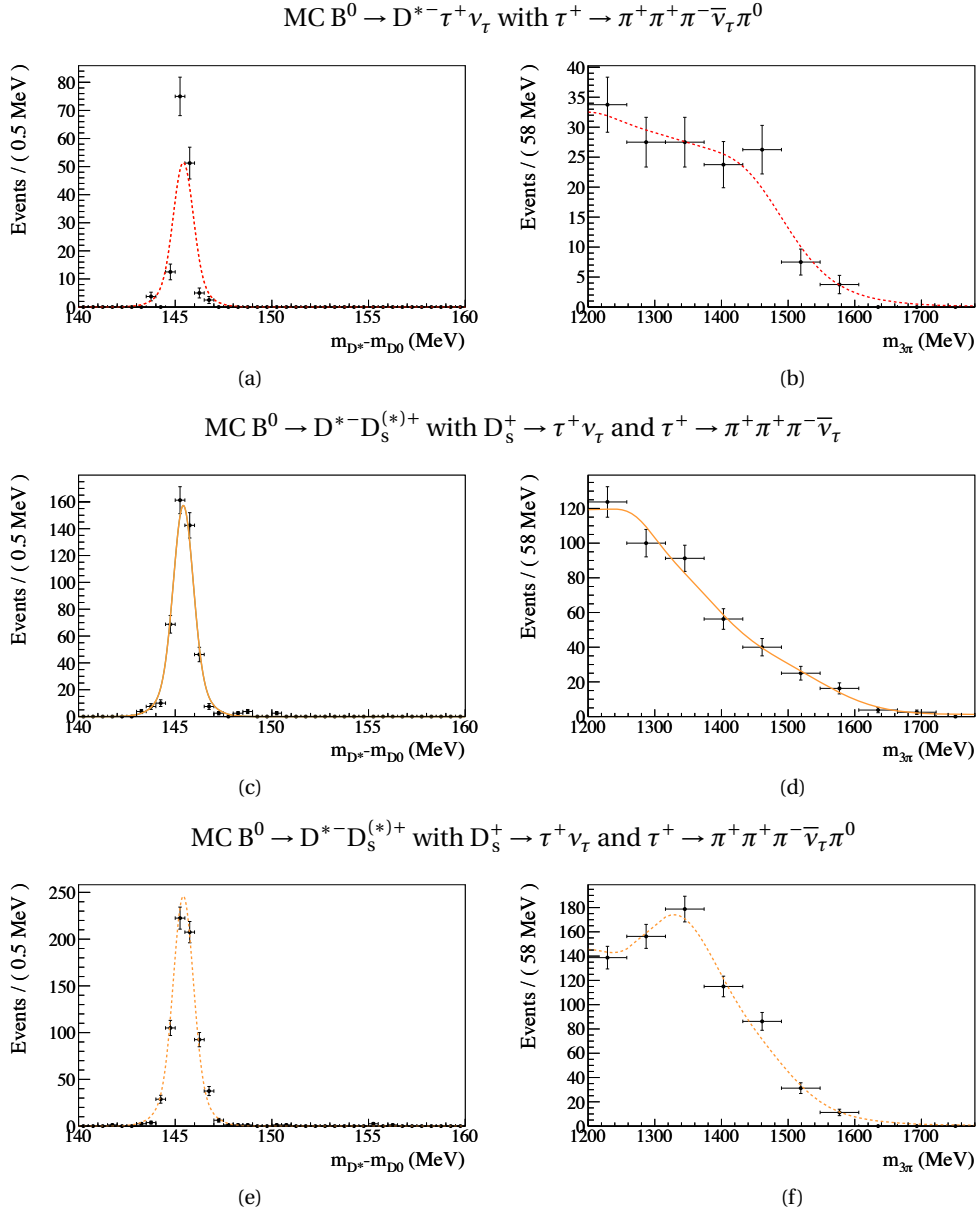


Figure 4.14: The (left)  $m_{D^*} - m_{D^0}$  and (right)  $m_{3\pi}$  distributions from the (top) MC  $B^0 \rightarrow D^{*-} \tau^+ \nu_\tau$  with  $\tau^+ \rightarrow \pi^+ \pi^+ \pi^- \bar{\nu}_\tau \pi^0$ , (middle) MC  $B^0 \rightarrow D^{*-} D_s^{(*)+}$  with  $D_s^+ \rightarrow \tau^+ \nu_\tau$  and  $\tau^+ \rightarrow \pi^+ \pi^+ \pi^- \bar{\nu}_\tau$  and (bottom) MC  $B^0 \rightarrow D^{*-} D_s^{(*)+}$  with  $D_s^+ \rightarrow \tau^+ \nu_\tau$  and  $\tau^+ \rightarrow \pi^+ \pi^+ \pi^- \bar{\nu}_\tau \pi^0$  samples after all selection cuts are applied. A fixed Gaussian shape is used to represent the  $m_{D^*} - m_{D^0}$  signal shape, whereas the  $m_{3\pi}$  distribution is modeled using a RooKeysPdf.

must be modeled by the distributions of the signal decay and those of the physics backgrounds.

By letting all yields float, except for the intrinsic  $\tau^+ \rightarrow \pi^+ \pi^+ \pi^- \bar{\nu}_\tau$  and  $\tau^+ \rightarrow \pi^+ \pi^+ \pi^- \bar{\nu}_\tau \pi^0$  components, whose ratio is fixed, the result depicted in Figure 4.18 is obtained.

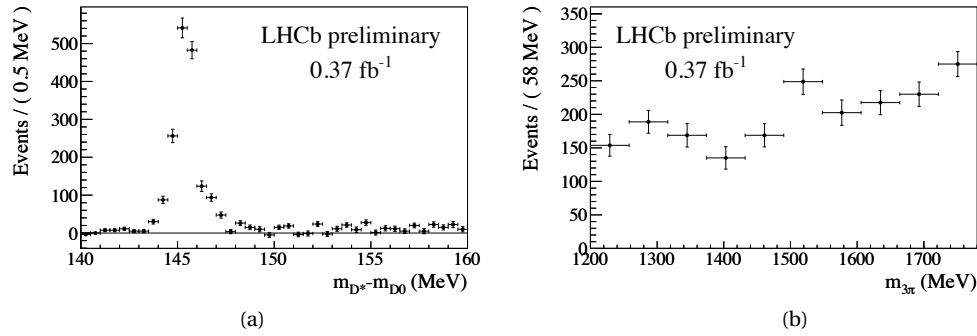


Figure 4.15: The (a)  $m_{D^*} - m_{D^0}$  and (b)  $m_{3\pi}$  distributions obtained from the complete RS and WS data sets, in which the WS combinatoric background candidates have been assigned negative weights.

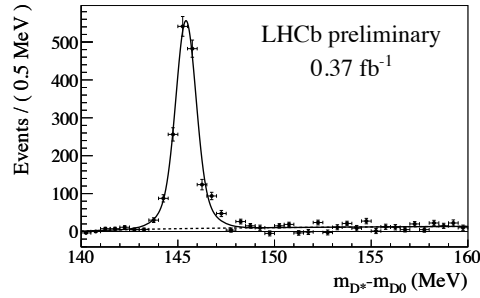


Figure 4.16: The  $m_{D^*} - m_{D^0}$  real data distribution (combinatorics subtracted). The real  $D^*$  distribution is modeled by a double Gaussian, whereas the fake  $D^*$  component is modeled using a RooDstD0BG distribution, which is depicted by the dashed line.

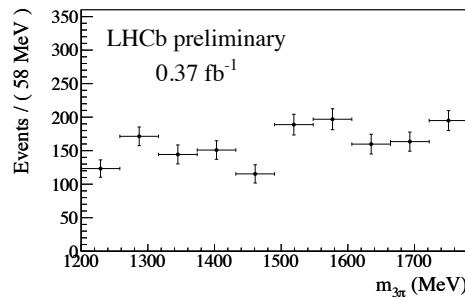


Figure 4.17: The  $m_{3\pi}$  real data distribution in which its candidates have been SPlot reweighted in order to correspond to the real  $D^*$  particle distribution component.

The distributions corresponding to a real  $\tau$  lepton contribution increase for a low  $3\pi$  invariant mass. Those that corresponds to a fake  $\tau$  lepton contribution increase for higher  $3\pi$  invariant

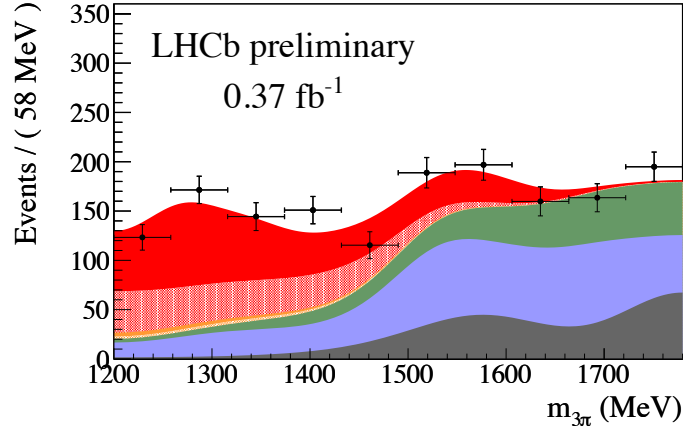


Figure 4.18: The  $m_{3\pi}$  real data distribution modeled by the signal distribution and the considered background distributions. From top to bottom, the model consists of the signal decay (red), the signal decay but with  $\tau^+ \rightarrow \pi^+ \pi^+ \pi^- \bar{\nu}_\tau \pi^0$  (red hashed), the  $B^0 \rightarrow D^{*-} D_s^{(*)+}$  with  $D_s^+ \rightarrow \tau^+ \nu_\tau$  and  $\tau^+ \rightarrow \pi^+ \pi^+ \pi^- \bar{\nu}_\tau$  decay (orange), the  $B^0 \rightarrow D^{*-} D_s^{(*)+}$  with  $D_s^+ \rightarrow \tau^+ \nu_\tau$  and  $\tau^+ \rightarrow \pi^+ \pi^+ \pi^- \bar{\nu}_\tau \pi^0$  decay (orange hashed), the  $B_u \rightarrow DX$  inclusive hadronic component (green), the exclusive  $B^0 \rightarrow D^{*-} \pi^- \pi^+ \pi^+ \pi^0$  contribution (blue) and the remaining  $B_d \rightarrow DX$  inclusive hadronic component (gray). The yield ratio of the  $\tau^+ \rightarrow \pi^+ \pi^+ \pi^- \bar{\nu}_\tau$  and  $\tau^+ \rightarrow \pi^+ \pi^+ \pi^- \bar{\nu}_\tau \pi^0$  components is fixed.

mass. However, the shapes of the individual contributions within the real  $\tau$  and fake  $\tau$  contributions are difficult to distinguish. The error on the individual components is therefore large, whereas the error on the total real  $\tau$  and fake  $\tau$  lepton contributions is smaller. The real  $\tau$  contribution is found to consist of

$$598 \pm 94 \text{ events.}$$

The components for which there is an extra  $\pi^0$  in the  $\tau$  decay, are dependent on the components without  $\pi^0$  particle. There are therefore no errors available for these contributions. All numbers of the fit result are given in Table 4.2.

The dominant systematic error is caused by the errors induced by fixing all distribution shapes and the fixed yields. The error is estimated by creating binned data sets of all distributions. To each bin of the produced histograms a statistical error is automatically assigned. A random fluctuation to the value of each bin is assigned by taking its mean value and adding a random Gaussian correction to it. The standard deviation of this Gaussian correction is chosen to be the bin error. Each time a binned fit is performed, random contributions are applied to all bins simultaneously. The variation of models used is depicted in Figure 4.19 for 200 iterations. In addition, the two fixed yields are varied with a deviation of 10%. The error on the real  $\tau$



Component	number of events
<b>Real taus</b>	<b>598 ± 94</b>
Signal	377 ± 310
$B^0 \rightarrow D^{*-} D_s^{(*)+}$	15 ± 916
Signal (with $\pi^0$ )	194
$B^0 \rightarrow D^{*-} D_s^{(*)+}$ (with $\pi^0$ )	12
<b>Fake taus</b>	<b>1010 ± 97</b>
$B^0 \rightarrow D^* \pi \pi \pi^0$	503 ± 270
$B_d \rightarrow DX$	252 ± 157
$B_u \rightarrow DX$	254 ± 263

Table 4.2: Fit results.

contribution stabilizes to a systematic error of

$$\pm 88 \text{ events.}$$

The likelihood of there being a real  $\tau$  component is depicted in Figure 4.20. The red curve represents the statistical error, whereas the blue curve also takes the systematic error into consideration. The likelihood of a low  $m_{3\pi}$  component in addition to the modeled hadronic inclusive  $b \rightarrow cX$  is  $5.7 \sigma$ .

## 4.6 Discussion

Figure 4.18 and the likelihood curve in Figure 4.20 demonstrate that it is difficult to model the  $m_{3\pi}$  distribution with inclusive hadronic models. A  $3\pi$  invariant mass distribution that is higher at low  $m_{3\pi}$  values is needed to complete the model. The invariant mass distribution of the three pions coming from a  $\tau$  particle satisfies this requirement. However, due to the similar distribution shapes, it is difficult to distinguish between different  $\tau$  sources based on the  $m_{3\pi}$  values alone. The considered real  $\tau$  contributions are estimated to cover at most a third of the extracted number of events, based on the relative known or predicted branching fractions and the reconstruction and selection efficiencies with respect to the hadronic background modes. It is expected that there is a missing background component. The decay time distribution indicates a underestimated short-lived contribution. This distribution could also shed light on the different  $\tau$  sources. A larger  $m_{3\pi}$  window could determine whether the missing component concerns a real  $\tau$  or a different background contribution. More statistics is needed to obtain an accurate model that will result in a definitive outcome. With more statistics and better distribution models, it is possible to apply more selection cuts which will better single out the signal distribution.

For a future study, this analysis would benefit from more exclusive background models. For instance, the source of the neglected  $B_s \rightarrow DX$  candidates can be determined and their dis-

tributions modeled. To sufficiently decrease the statistical error, more is needed than just an increase in data available. A 2D simultaneous fit (for instance of the  $3\pi$  invariant mass and the  $\tau$  lepton life time) can be used to constrain the fit in order to reduce the statistical error. A larger  $3\pi$  invariant mass window would allow the distribution shapes to be better defined. More accurate distribution shapes will reduce the systematic uncertainty if the physics background remains to be modeled with fixed shapes.

Once a confident measurement is made, the measured number of signal events must be normalised to the measured number of events coming from a decay mode with a well known branching fraction. There are three likely normalisation modes. The muonic counterpart of the signal decay is one choice. The advantage of this choice is that this ratio is directly sensitive to new physics contributions. A disadvantage is the differences between reconstruction and trigger efficiencies of the muon track and the three pion tracks originating from the  $\tau$  particle. The second choice is to normalise to the hadronic  $B^0 \rightarrow D^{*-} \pi^- \pi^+ \pi^+$  decay. This channel has the same final state as the signal channel, but without missing energy. The branching fraction is well measured and recently improved by LHCb. Apart from the inclusion of the B mass, the same initial selection can be applied to this decay channel. Thirdly,  $B^0 \rightarrow D^{*-} D_s^{(*)+}$  with  $D_s^+ \rightarrow \tau^+ \nu_\tau$  can be used as a normalisation channel. This component is already modeled as a background contribution and no changes need to be made to the selection. However, trigger differences need to be understood.

In 2009, the result obtained by Belle was based on just  $25 \pm 7$  events [45]. For their latest result, the BaBar collaboration collected  $245 \pm 27$  signal events [46]. The BaBar result is competitive with what LHCb can collect with current data. However, as the size of the LHCb dataset rapidly increases, a statistically superior measurement can be made within its lifetime. To obtain a competitive measurement of the ratio of the muonic and tauonic branching fractions, the total statistical error has to be reduced to less than 10% and the systematical error to less than 9%. These errors include the errors of the normalisation channel and those of the  $B^0 \rightarrow D^{*-} \mu^+ \nu_\mu$  branching fraction.

This analysis is based on exclusive  $\tau$  reconstruction. Although this study is statistically limited, the goodness of the constrained fit has served as a useful selection requirement. The possibility of exclusive  $\tau$  reconstruction has been demonstrated and can be used for either selection purposes or to model decay time or momentum distributions in future analyses.

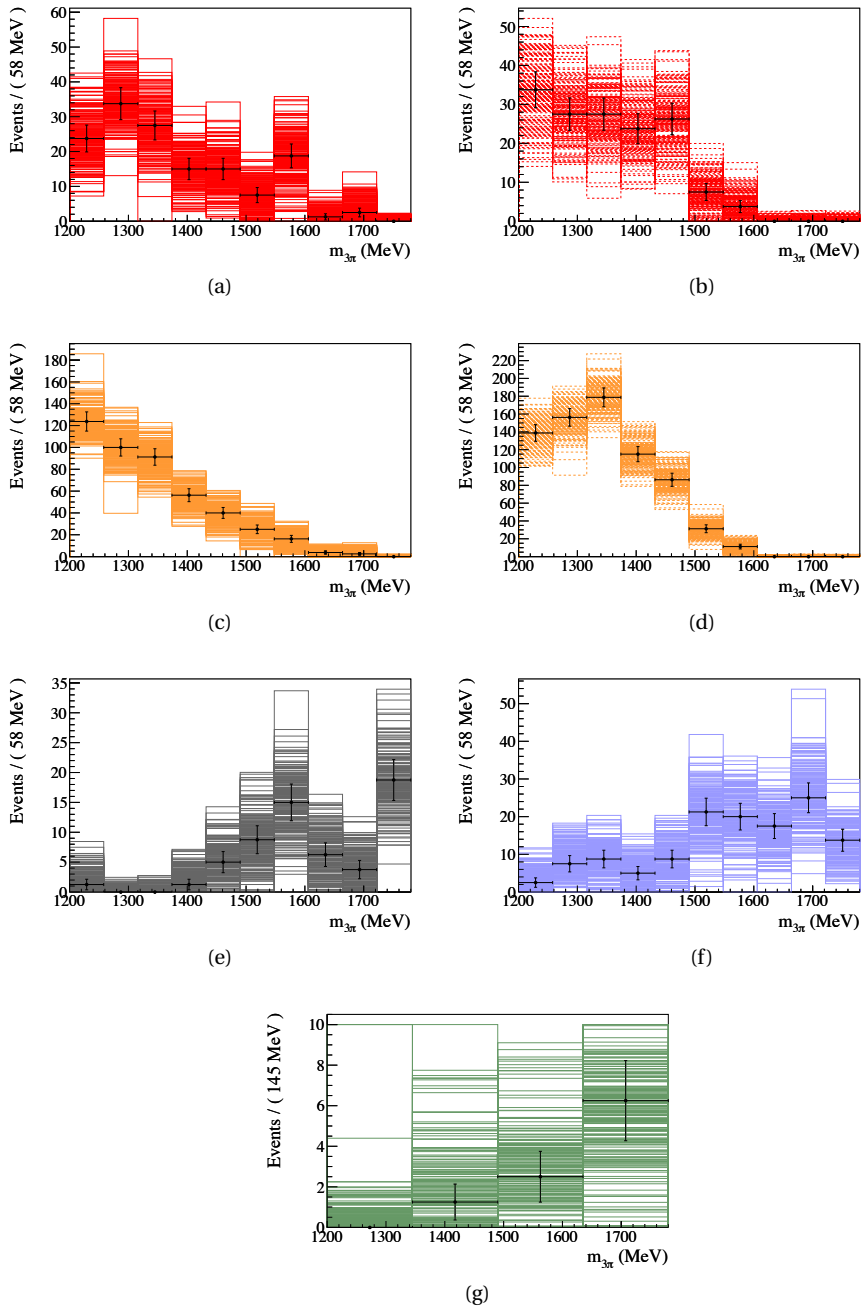


Figure 4.19: The variations on the binned  $m_{3\pi}$  MC distributions of the signal decay (red), the signal decay but with  $\tau^+ \rightarrow \pi^+ \pi^+ \pi^- \bar{\nu}_\tau \pi^0$  (red dashed), the  $B^0 \rightarrow D^{*-} D_s^{(*)+}$  with  $D_s^+ \rightarrow \tau^+ \nu_\tau$  and  $\tau^+ \rightarrow \pi^+ \pi^+ \pi^- \bar{\nu}_\tau \pi^0$  decay (orange), the  $B^0 \rightarrow D^{*-} D_s^{(*)+}$  with  $D_s^+ \rightarrow \tau^+ \nu_\tau$  and  $\tau^+ \rightarrow \pi^+ \pi^+ \pi^- \bar{\nu}_\tau \pi^0$  decay (orange dashed), the  $B_u \rightarrow DX$  inclusive hadronic component (green), the exclusive  $B^0 \rightarrow D^{*-} \pi^- \pi^+ \pi^+ \pi^0$  contribution (blue) and the remaining  $B_d \rightarrow DX$  hadronic component (gray).

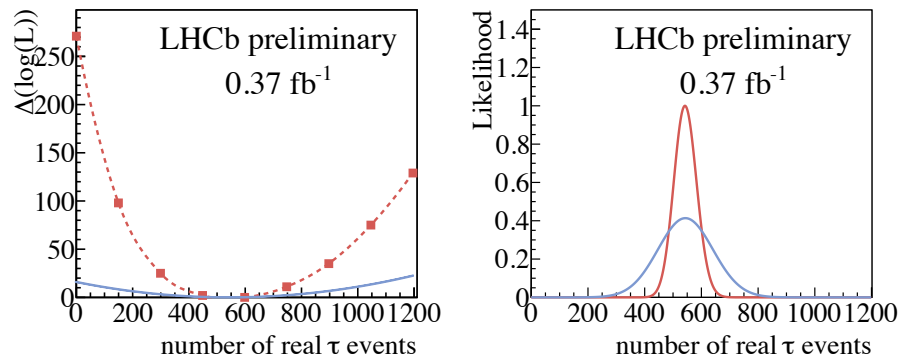


Figure 4.20: (left) the  $\Delta(\log)$  distribution of the likelihood and (right) the likelihood. The red line is based on statistical error, where the points represent likelihood measurements. The blue line includes the systematic error.



## Summary

The work on which this thesis is based started in 2007. At this stage the LHCb detector was in its final state of commissioning. An offline emulator was developed for the testing of the FPGA algorithms implemented in the readout electronics as an essential part of the commissioning of the LHCb Silicon Tracker. After many iterations of improving both the emulator and the firmware, perfection was achieved when the emulation was tested on real data in 2010.

The magnetic field parameterization, as described in this thesis, was finalised in 2009. From this moment a single parameterization has been used to accurately describe both the upward and downward polarities with a simple sign inversion. This description of the magnetic field has been used for the reconstruction of LHCb data since the beginning of 2010. In 2011 additional magnetic field measurements were taken to confirm the map's accuracy. As a result of the study based on the new measurements, which is beyond the scope of this thesis, improvements were made to the existing field map.

My study on exclusive  $\tau$  reconstruction was performed on simulated data, while LHCb data slowly accumulated real data at 7 TeV throughout 2010. The reconstruction of many different decay modes including a  $\tau$  lepton were considered. Most notably, the full reconstruction of the  $B_s^0 \rightarrow \tau^+ \tau^-$  was provided in terms of a mathematical parameterization. In all cases considered, an exclusive reconstruction of the  $\tau$  lepton has been achieved up to a certain ambiguity. Constrained fits were introduced to improve the performance of the analytical reconstructions. The accuracies achieved were found to be inversely dependent on the number of constraints used in the decay reconstruction. The  $B_s^0 \rightarrow \tau^+ \nu_\tau$  decay mode was not included, as there are not enough measured values to constrain it.

With real data, the exclusive reconstruction of  $B^0 \rightarrow D^{*-} \tau^+ \nu_\tau$  is performed. An initial study was done based on data taken in 2010. The full study, as described in this thesis, was based on  $0.37 \text{ fb}^{-1}$  of data from the 2011 data taking. It is demonstrated that it is possible to reconstruct the  $B^0 \rightarrow D^{*-} \tau^+ \nu_\tau$  decay exclusively with the method developed in this thesis. The number of signal events collected from current data is competitive with those collected at other experiments. However, within the lifetime of LHCb a statistically superior measurement can be made due to its fastly increasing dataset. With higher statistics, this method could be used to obtain the ratio of  $B^0 \rightarrow D^{*-} \tau^+ \nu_\tau$  over  $B^0 \rightarrow D^{*-} \mu^+ \nu_\mu$ , which might indicate a possible contribution by a charged Higgs boson in the semileptonic decays of B mesons.



## A The $b \rightarrow c \ell \nu_\ell$ decay rate

The general expression for the differential decay rate of a particle of energy  $E$  is given by Fermi's 'Golden Rule':

$$d\Gamma = \frac{1}{2E} \langle |\mathcal{M}|^2 \rangle d\Phi \quad (\text{A.1})$$

where  $d\Phi$  denotes the phase space which depends on the masses and the momenta of the particles in the initial and final states. The details of the interactions of the particles via the various forces are encoded in the matrix element  $\mathcal{M}$ , which can be expressed as

$$\mathcal{M} = \frac{g_w}{\sqrt{2}} |V_{cb}| \left( \bar{\psi}_c \gamma_\mu \frac{1}{2} (1 - \gamma^5) \psi_b \right) \cdot \frac{1}{m_W^2} \cdot \frac{g_w}{\sqrt{2}} \left( \bar{\psi}_\ell \gamma^\mu \frac{1}{2} (1 - \gamma^5) \psi_\nu \right) \quad (\text{A.2})$$

In order to square the matrix element and sum it over all spin states, the Casimir trick is used:

$$\sum_{\text{spins}} (\bar{\psi}_1 \Gamma \psi_2) (\bar{\psi}_1 \Gamma \psi_2)^* = \text{Tr}\{\Gamma(\not{p}_2 + m_2) \bar{\Gamma}(\not{p}_1 + m_1)\} \quad (\text{A.3})$$

where  $\not{p} = \gamma^\mu p_\mu$  in Feynman slash notation. The result is that  $\langle |\mathcal{M}|^2 \rangle$  can be expressed as the product of two traces (neglecting any neutrino mass)

$$\begin{aligned} \langle |\mathcal{M}|^2 \rangle &= \frac{1}{2} \sum_{\text{spins}} |\mathcal{M}|^2 \quad (\text{A.4}) \\ &= \frac{1}{2} \left( \frac{g_w^2}{8m_W^2} \right)^2 |V_{cb}|^2 \cdot \text{Tr}\{\gamma_\mu (1 - \gamma^5)(\not{p}_c + m_c) \gamma_\nu (1 - \gamma^5)(\not{p}_b + m_b)\} \\ &\quad \cdot \text{Tr}\{\gamma^\mu (1 - \gamma^5)(\not{p}_\ell + m_\ell) \gamma^\nu (1 - \gamma^5)(\not{p}_\nu)\} \quad (\text{A.5}) \end{aligned}$$

The trace theorem

$$\begin{aligned} &\text{Tr}\{\gamma_\mu (1 - \gamma^5)(\not{p}_1) \gamma_\nu (1 - \gamma^5)(\not{p}_2)\} \cdot \text{Tr}\{\gamma^\mu (1 - \gamma^5)(\not{p}_3) \gamma^\nu (1 - \gamma^5)(\not{p}_4)\} \\ &= 256 (p_1 \cdot p_3) (p_2 \cdot p_4) \quad (\text{A.6}) \end{aligned}$$



## Appendix A. The $b \rightarrow c \ell \nu_\ell$ decay rate

---

plus the fact that  $\Gamma^\mu \Gamma^\nu = 0$  and that the trace of any expression of an odd number of gamma matrices is 0, reduces the expression to

$$\langle |\mathcal{M}|^2 \rangle = 64 G_F^2 |V_{cb}|^2 (p_c \cdot p_\ell) (p_\nu \cdot p_b) \quad (\text{A.7})$$

with

$$\frac{G_F}{\sqrt{2}} = \frac{g_w^2}{8m_W^2} \quad (\text{A.8})$$

The matrix element is determined in the b-quark rest frame. In this frame where  $\vec{p}_b = 0$ , the inner product between the bottom quark and the neutrino is given by

$$(p_\nu \cdot p_b) = m_b E_\nu \quad (\text{A.9})$$

As momentum conservation enforces that  $p_b - p_\nu = p_c + p_\ell$ , the inner product between the charm quark and the lepton can be written as

$$\begin{aligned} (p_c \cdot p_\ell) &= \frac{1}{2} \left( (p_c + p_\ell)^2 - p_c^2 - p_\ell^2 \right) \\ &= \frac{1}{2} \left( (p_b - p_\nu)^2 - p_c^2 - p_\ell^2 \right) \\ &= \frac{1}{2} \left( p_b^2 + p_\nu^2 - 2(p_\nu \cdot p_b) - p_c^2 - p_\ell^2 \right) \\ &= \frac{1}{2} \left( m_b^2 - 2m_b E_\nu - m_c^2 - m_\ell^2 \right) \end{aligned} \quad (\text{A.10})$$

The matrix element can thus solely be expressed in terms of  $E_\nu$

$$\langle |\mathcal{M}|^2 \rangle = 64 G_F^2 |V_{cb}|^2 \frac{1}{2} \left( m_b^2 - 2m_b E_\nu - m_c^2 - m_\ell^2 \right) m_b E_\nu \quad (\text{A.11})$$

The differential decay rate becomes

$$d\Gamma = \frac{1}{2E} \langle |\mathcal{M}|^2 \rangle d\Phi = \frac{16 G_F^2}{m_b} |V_{cb}|^2 \left( m_b^2 - 2m_b E_\nu - m_c^2 - m_\ell^2 \right) m_b E_\nu d\Phi \quad (\text{A.12})$$

with  $E = m_b$  in the b rest frame. In order to obtain the total decay rate, the integration over the phase space is performed. The integrand only depends on the neutrino energy, which in its turn depends on the lepton energy. Therefore, as a first step the integral over the c-quark momentum is performed. The integral over the  $\delta$ -function gives 1 for the integral over  $p_c$ .

$$\int d\Phi = \frac{1}{8(2\pi)^5} \int \delta(m_b - E_c - E_\ell - E_\nu) \delta^3(\vec{p}_c - \vec{p}_\ell - \vec{p}_\nu) \frac{d^3 \vec{p}_c}{E_c} \frac{d^3 \vec{p}_\ell}{E_\ell} \frac{d^3 \vec{p}_\nu}{E_\nu} \quad (\text{A.13})$$

$$= \frac{1}{8(2\pi)^5} \int \delta(m_b - E_c - E_\ell - E_\nu) \frac{1}{E_c} \frac{d^3 \vec{p}_\ell}{E_\ell} \frac{d^3 \vec{p}_\nu}{E_\nu} \quad (\text{A.14})$$

The term  $d^3\vec{p}_\ell$  can be written in terms of energies, such that the second delta-function can be eliminated from the integral. In order to do this the relation

$$d|\vec{p}_\ell| = \frac{E_\ell}{|\vec{p}_\ell|} dE_\ell \quad (\text{A.15})$$

is used. It follows that

$$d^3\vec{p}_\ell = |\vec{p}_\ell|^2 \sin\theta d|\vec{p}_\ell| d\theta d\phi \quad (\text{A.16})$$

$$= |\vec{p}_\ell| E_\ell \sin\theta dE_\ell d\theta d\phi \quad (\text{A.17})$$

If the lepton momentum is chosen such that it points along the  $z$ -axis and the angle between the lepton and neutrino is given by  $\theta$ , the  $c$ -quark energy can be expressed as

$$E_c = \sqrt{m_c^2 + \vec{p}_c^2} = \sqrt{m_c^2 + (\vec{p}_\ell + \vec{p}_\nu)^2} \quad (\text{A.18})$$

$$= \sqrt{m_c^2 + |\vec{p}_\ell|^2 + E_\nu^2 + 2|\vec{p}_\ell|E_\nu \cos\theta} \quad (\text{A.19})$$

This implies that

$$d\theta = \frac{-E_c}{|\vec{p}_\ell|E_\nu \sin\theta} dE_c \quad (\text{A.20})$$

Combining equations A.17 and A.20 leads to

$$d^3\vec{p}_\ell = E_\ell \frac{-E_c}{E_\nu} dE_\ell dE_c d\phi \quad (\text{A.21})$$

The integral expression A.14 becomes

$$\int d\Phi = -\frac{1}{8(2\pi)^5} \int \delta(m_b - E_c - E_\ell - E_\nu) \frac{d^3\vec{p}_\nu}{E_\nu^2} dE_\ell dE_c d\phi \quad (\text{A.22})$$

$$= -\frac{1}{8(2\pi)^4} \int \delta(m_b - E_c - E_\ell - E_\nu) \frac{d^3\vec{p}_\nu}{E_\nu^2} dE_\ell dE_c \quad (\text{A.23})$$

$$= \frac{1}{8(2\pi)^4} \int \frac{d^3\vec{p}_\nu}{E_\nu^2} dE_\ell \quad (\text{A.24})$$

$$(\text{A.25})$$

where integration over  $d\phi$  gives a factor  $2\pi$  and integration over  $dE_c$  gives 1 because of the  $\delta$ -function. Equivalently to equation A.16, for the neutrino momentum

$$d^3\vec{p}_\nu = E_\nu^2 \sin\theta' dE_\nu d\theta' d\phi' \quad (\text{A.26})$$

## Appendix A. The $b \rightarrow c \ell \nu_\ell$ decay rate

---

holds, such that

$$\int d^3 \vec{p}_\nu = 4\pi \int E_\nu^2 dE_\nu \quad (\text{A.27})$$

and the integral over the phase space reduces to

$$\int d\Phi = \frac{1}{4(2\pi)^3} \int dE_\nu dE_\ell \quad (\text{A.28})$$

The expression of the total decay rate becomes

$$\Gamma = \frac{4G_F^2}{(2\pi)^3} |V_{cb}|^2 \int (m_b^2 - 2m_b E_\nu - m_c^2 - m_\ell^2) E_\nu dE_\nu dE_\ell \quad (\text{A.29})$$

Before integrating over  $E_\nu$  and  $E_\ell$  their limits need to be determined. First the integration over  $E_\nu$  will be performed. Therefore the integration limits of  $E_\nu$  need to be expressed in terms of  $E_\ell$ . For  $E_\ell$  an absolute maximum and minimum will be calculated afterwards. First  $E_\nu$  will be expressed in terms of  $E_\ell$ . Equivalently to Equation A.10, it follows that

$$(p_c \cdot p_\nu) = \frac{1}{2}(m_b^2 - 2m_b E_\ell - m_c^2 + m_\ell^2) \quad (\text{A.30})$$

The b-quark mass can be written as the invariant mass of the c-quark, the lepton and neutrino

$$0 = m_{c\ell\nu}^2 - m_b^2 = (p_c + p_\ell + p_\nu)^2 - m_b^2 \quad (\text{A.31})$$

$$= m_c^2 + m_\ell^2 + 2(p_c \cdot p_\ell) + 2(p_c \cdot p_\nu) + 2(p_\ell \cdot p_\nu) - m_b^2 \quad (\text{A.32})$$

$$= m_b^2 - m_c^2 + m_\ell^2 - 2m_b E_\ell - 2m_b E_\nu + 2E_\ell E_\nu - 2\sqrt{E_\ell^2 - m_\ell^2} E_\nu \cos\theta \quad (\text{A.33})$$

Hence

$$E_\nu = \frac{m_b^2 - m_c^2 + m_\ell^2 - 2m_b E_\ell}{2m_b - 2E_\ell + 2\sqrt{E_\ell^2 - m_\ell^2} \cos\theta} \quad (\text{A.34})$$

The maximum value of  $E_\nu$  occurs when  $\cos\theta = -1$ , its minimum when  $\cos\theta = +1$ . Thus

$$E_\nu^{\min} = \frac{m_b^2 - m_c^2 + m_\ell^2 - 2m_b E_\ell}{2m_b - 2E_\ell + 2\sqrt{E_\ell^2 - m_\ell^2}} \quad \text{and} \quad E_\nu^{\max} = \frac{m_b^2 - m_c^2 + m_\ell^2 - 2m_b E_\ell}{2m_b - 2E_\ell - 2\sqrt{E_\ell^2 - m_\ell^2}} \quad (\text{A.35})$$

For the limits of  $E_\ell$  the absolute values are calculated. In order to do this, first the invariant mass of the neutrino and c-quark is considered.

$$m_{c\nu}^2 = (p_c + p_\nu)^2 = m_c^2 + 2(p_c \cdot p_\nu) \quad (\text{A.36})$$

---

Equivalently to the derivation of equation A.10 it follows that

$$m_{\text{cv}}^2 = m_{\text{b}}^2 + m_{\ell}^2 - 2m_{\text{b}}E_{\ell} \quad (\text{A.37})$$

and hence

$$E_{\ell} = \frac{m_{\text{b}}^2 + m_{\ell}^2 - m_{\text{cv}}^2}{2m_{\text{b}}} \quad (\text{A.38})$$

The minimal value of the invariant mass  $m_{\text{c}\ell}$  is  $m_{\text{c}} + m_{\ell}$ , where the particle momenta are colinear. The minimal value of the energy of a particle is its mass, when it's at rest. The lower and upper limits on the possible value of the lepton energy thus become

$$E_{\ell}^{\text{min}} = m_{\ell} \quad \text{and} \quad E_{\ell}^{\text{max}} = \frac{m_{\text{b}}^2 + m_{\ell}^2 - m_{\text{c}}^2}{2m_{\text{b}}} \quad (\text{A.39})$$

Before the integration it suffices to make a coordinate change. The coordinate change

$$x = \frac{m_{\text{b}}E_{\ell}}{2} \quad (\text{A.40})$$

is chosen. In addition

$$y = \frac{m_{\text{c}}}{m_{\text{b}}} \quad \text{and} \quad z = \frac{m_{\ell}}{m_{\text{b}}} \quad (\text{A.41})$$

are used. The integration limits become

$$E_{\text{v}}^{\text{min}} = m_{\text{b}} \frac{-1 + x + y^2 - z^2}{-2 + x + \sqrt{x^2 - 4z^2}} \quad \text{and} \quad E_{\text{v}}^{\text{max}} = -m_{\text{b}} \frac{-1 + x + y^2 - z^2}{2 - x + \sqrt{x^2 - 4z^2}} \quad (\text{A.42})$$

After the coordinate change this becomes

$$x^{\text{min}} = m_{\text{b}}z \quad \text{and} \quad x^{\text{max}} = \frac{1}{2}m_{\text{b}}(1 - y^2 + z^2) \quad (\text{A.43})$$

The decay rate reduces to

$$\Gamma = \frac{4G_{\text{F}}^2 m_{\text{b}}}{(2\pi)^3} |V_{\text{cb}}|^2 \int_{x^{\text{min}}}^{x^{\text{max}}} \int_{E_{\text{v}}^{\text{min}}}^{E_{\text{v}}^{\text{max}}} (m_{\text{b}}(-1 + y^2 + z^2) + 2E_{\text{v}}) E_{\text{v}} dE_{\text{v}} dx \quad (\text{A.44})$$

$$= \frac{G_{\text{F}}^2 m_{\text{b}}^4}{6(2\pi)^3} |V_{\text{cb}}|^2 \int_{x^{\text{min}}}^{x^{\text{max}}} w(x, y, z) dx \quad (\text{A.45})$$

## Appendix A. The $b \rightarrow c \ell \nu_\ell$ decay rate

---

with

$$w(x, y, z) = \frac{\sqrt{x^2 - 4z^2}(-1 + x + y^2 - z^2)^2}{(-1 + x - z^2)^3} \cdot \left[ x(3 - 5x + 2x^2 - (-3 + x)y^2) + (-4 + 10x - 5x^2 + (-8 + 3x)y^2)z^2 + (-4 + 3x)z^4 \right] \quad (\text{A.46})$$

The total decay rate, after integration over  $x$ , results in

$$\Gamma = \frac{G_F^2 m_b^5}{192\pi^3} |V_{cb}|^2 f_{ps} \quad (\text{A.47})$$

with the phase space factor  $f_{ps}$

$$f_{ps} = s + y^6 s - 7z^2 s + z^6 s + y^2(-7 + 12z^2 - 7z^4) s - z^4(7s + 24 \log 2) + y^4(-7s - 7z^2 s + 12z^4 \log 4) + 12 \left[ 2y^4(-1 + z^4) \log y + 2(-1 + y^4)z^4 \log z - (y^4 + (-2 + y^4)z^4) \log(1 - y^2 + z^2 + s) - y^4(-1 + z^4) \log(-y^2(1 + z^2) - (-1 + z^2)(1 - z^2 + s)) \right] \quad (\text{A.48})$$

where

$$s = \sqrt{(-1 + y^2)^2 - 2(1 + y^2)z^2 + z^4} \quad (\text{A.49})$$

# Bibliography

- [1] Peter W. Higgs. Broken Symmetries and the Masses of Gauge Bosons. *Phys. Rev. Lett.*, 13:508–509, 1964.
- [2] Steven Weinberg. A Model of Leptons. *Phys. Rev. Lett.*, 19:1264–1266, 1967.
- [3] Makoto Kobayashi and Toshihide Maskawa. CP Violation in the Renormalizable Theory of Weak Interaction. *Prog. Theor. Phys.*, 49:652–657, 1973.
- [4] Lincoln Wolfenstein. Parametrization of the Kobayashi-Maskawa Matrix. *Phys. Rev. Lett.*, 51:1945–1947, 1983.
- [5] K. Nakamura et al. (Particle Data Group). Review of Particle Physics. *J. Phys. G*, 37:075021, 2010.
- [6] Nathan Isgur and Mark B. Wise. Weak decays of heavy mesons in the static quark approximation. *Phys. Lett. B*, 232:113–117, 1989.
- [7] Matthias Neubert and Volker Rieckert. New approach to the universal form factor in decays of heavy quarks. *Nucl. Phys. B*, 382:97–119, 1992.
- [8] Michael E. Luke. Effects of subleading operators in the heavy quark effective theory. *Phys. Lett. B*, 252:447–455, 1990.
- [9] P. F. Harrison and H. R. Quinn. The BABAR Physics Book. SLAC-R-504, 1998.
- [10] J.G. Körner and G.A. Schuler. Exclusive semileptonic heavy meson decays including lepton mass effects. *Z. Phys. C*, 46:93–109, 1990.
- [11] D.S. Hwang and D.-W. Kim. Model independent calculation of  $\mathcal{B}(\bar{B}^0 \rightarrow D^{(*)+} \tau^- \bar{\nu}_\tau) / \mathcal{B}(\bar{B}^0 \rightarrow D^{(*)+} e^- \bar{\nu}_e)$ . *Eur. Phys. J. C*, 14:271–274, 2000.
- [12] C.-H. Chen and C.-Q. Geng. Charged Higgs on  $B^- \rightarrow \tau \bar{\nu}_\tau$  and  $\bar{B} \rightarrow P(V) \ell \bar{\nu}_\ell$ . *JHEP*, 10:053, 2006.
- [13] The BaBar Collaboration. Measurement of the semileptonic decays  $\bar{B} \rightarrow D \tau^- \bar{\nu}_\tau$  and  $\bar{B} \rightarrow D^* \tau^- \bar{\nu}_\tau$ . *Phys. Rev. D*, 79:092002, 2009.

## Bibliography

---

- [14] The Belle Collaboration. Observation of  $B^0 \rightarrow D^{*-} \tau^+ \nu_\tau$  decay at belle. *Phys. Rev. Lett.*, 99:191807, 2007.
- [15] Manuel Franco Sevilla. Measurements of  $\bar{B} \rightarrow D^{(*)-} \tau^+ \nu_\tau$  and  $|V_{ub}|$  at BaBar. Proceedings of Science: [http://pos.sissa.it/archive/conferences/134/155/EPS-HEP2011\\_155.pdf](http://pos.sissa.it/archive/conferences/134/155/EPS-HEP2011_155.pdf), 2011.
- [16] M. Tanaka. Charged Higgs Effects on Exclusive Semi-tauonic B Decays. *Zeitschrift für Physik C Particles and Fields*, 67:321–326, 1994.
- [17] The LHCb Collaboration. The LHCb Detector at the LHC. *JINST*, 3:S08005, 2008.
- [18] The LHCb Collaboration. Measurement of  $\sigma(pp \rightarrow b\bar{b}X)$  at  $\sqrt{s}=7$  Tev in the forward region. *Physics Letters B*, 694:209–216, 2010.
- [19] M. Losasso et al. Tests and Field Map of LHCb Dipole Magnet. *IEEE Transactions on Applied Superconductivity*, 16:1700–1703, 2006.
- [20] <http://www.vectorfields.com>.
- [21] <http://root.cern.ch/root/html/TMultiDimFit.html>.
- [22] The LHCb Collaboration. Measurement of b-hadron masses. *Phys. Lett. B*, 708:241–248, 2012.
- [23] Guido Haefeli and Alex Gong. Velo and ST non-zero suppressed bank data format. EDMS 692431, 2008.
- [24] The LHCb Collaboration. LHCb Computing Technical Design Report. CERN-LHCC-2005-019, 2005.
- [25] T. Sjostrand, S. Mrenna, and P. Z. Skands. PYTHIA 6.4 Physics and Manual. *JHEP*, 0605, 2006.
- [26] D. J. Lange. The EvtGen particle decay simulation package. *Nucl. Inst. Meth.*, A(462):152, 2001.
- [27] The GEANT4 Collaboration. GEANT4, a simulation toolkit. *Nucl. Inst. Meth.*, A(506):250, 2003.
- [28] M. Clemencic, N. Gilardi, and J. Palacios. LHCb Conditions Database. CERN-LHCb-2006-017, 2006.
- [29] Chongxing Yue, Yanming Zhang, and Lanjun Liu. Non-universal gauge bosons  $Z'$  and lepton flavor-violation tau decays. *Phys. Lett. B*, 547:252–256, 2002.
- [30] Apostolos Pilaftsis. Gauge and Scheme Dependence of Mixing Matrix Renormalization. *Phys. Rev. D*, 65:115013, 2002.
- [31] The BaBar Collaboration. Limits on tau Lepton-Flavor Violating Decays in three charged leptons. *Phys. Rev. D*, 81:111101, 2010.

- 
- [32] The Belle Collaboration. Search for Lepton Flavor Violating tau Decays into Three Leptons. *Phys. Lett. B*, 660:154–160, 2008.
- [33] Anne Keune. The lepton flavour violating decay  $\tau^\pm \rightarrow \mu^\pm \mu^\pm \mu^\mp$  at LHCb. to be published in: *Yadernaya fizika*, 2010.
- [34] J. Albrecht et al. LHCb-ANA-2011-100, 2012.
- [35] W. D. Hulsbergen. The global covariance matrix of tracks fitted with a Kalman filter and an application in detector alignment. *Nucl. Inst. Meth., A*(600):471–477, 2009.
- [36] The CDF Collaboration. Search for New Physics Using High-Mass Tau Pairs from 1.96 Tev  $p\bar{p}$  Collisions. *Phys. Rev. Lett.*, 95:131801, 2005.
- [37] Anne Keune. A first consideration of the decay channel  $\tau^\pm \rightarrow \pi^\pm \pi^\pm \pi^\mp \nu_\tau$  as prompt  $\tau$  normalisation channel. LHCb-INT-2009-030, 2009.
- [38] C. Sturm. Mémoire sur la résolution des équations numériques. *Bull. des sciences de Férussac*, 11, 1929.
- [39] J. H. Wilkinson. *Rounding Errors in Algebraic Processes*. Englewood Cliffs, New Jersey: Prentice Hall., 1963.
- [40] <http://root.cern.ch/root/html/TMinuit.html>.
- [41] Y. Grossman, Z. Ligeti, and E. Nardi.  $B \rightarrow \tau^\pm \tau^\mp (X)$  decays: First constraints and phenomenological implications. *Phys. Rev. D*, 55:2768, 1997.
- [42] The BaBar Collaboration. Searches for the Decays  $B^0 \rightarrow \ell^\pm \tau^\mp$  and  $B^+ \rightarrow \ell^+ \nu$  ( $\ell = e, \mu$ ) using Hadronic Tag Reconstruction. *Physical Review D*, 77:091104R, 2008.
- [43] Wouter Verkerke and David Kirkby. The RooFit toolkit for data modeling. arXiv:physics/0306116v1, 2003.
- [44] Muriel Pivk and Francois R. Le Diberder. sPlot: a statistical tool to unfold data distributions. *Nucl. Inst. Meth., A*(555):356, 2005.
- [45] The Belle Collaboration. Measurement of  $B \rightarrow D^* \tau \nu$  using full reconstruction tags. arXiv:0910.4301v1, 2009.
- [46] The BaBar Collaboration. Evidence for an excess of  $\bar{B} \rightarrow D^* \tau^- \bar{\nu}_\tau$  decays. arXiv:1205.5442v1, 2012.







# Curriculum Vitae

Name: Anne Keune

Date of birth: 14-11-1981

Nationality: Dutch

## Education:

- 2007-2012: Ph.D. in Particle Physics at the Ecole Polytechnique Fédérale de Lausanne
  - Thesis: Reconstruction of the tau lepton and the study of  $B^0 \rightarrow D^{*-} \tau^+ \nu_\tau$  at LHCb
  - Documentation of the feasibility of the decay  $B \rightarrow \tau \tau$  at the LHCb experiment
  - Parameterization of the LHCb magnetic field
  - Implementation of an offline FPGA emulation of the LHCb Silicon Tracker
- 2005-2007: Master in Particle and Astroparticle Physics at Nikhef
  - Graduated Cum Laude
  - Thesis: Vertexing and pattern recognition study on LHCb VELO testbeam data
  - CERN summer student: Statistical evaluation of the ATLAS MDT certification data and RPC efficiency measurement resulting in a cabling scheme verification method for ATLAS
- 2002-2006: Double Bachelor in Physics and Mathematics at Leiden University
  - Thesis: Determination of quantum operators spectra using inverse spectral theory
  - Head teacher math at yearly high-school exam courses hosted by Leiden University
- 1999-2001: Propedeuse (1 year degree) in Computer Science at the Vrije Universiteit in Amsterdam